On the emergence and evolution of jets and vortices in turbulent planetary atmospheres.

Thibault Jougla

Communauté UNIVERSITÉ Grenoble Alpes

University of St Andrews

THÈSE

Pour obtenir le grade de

DOCTEUR DE LA COMMUNAUTE UNIVERSITE GRENOBLE ALPES

préparée dans le cadre d'une cotutelle *entre la Communauté Université Grenoble Alpes* et *l'Université de Saint Andrews*

Spécialité : **Océan, atmosphère, hydrologie**

Arrêté ministériel : le 6 janvier 2005 – 25 mai 2016

Présentée par

Thibault JOUGLA

Thèse dirigée par **David DRITSCHEL**
codirigée par **Jan-Bert FLOR**

préparée au sein de la **School of Mathematics and Statistics** et du **Laboratoire des Écoulements Géophysiques et Industriels**

dans **les Écoles Doctorales Terre, Univers, Environnement.**

Sur l'émergence et l'évolution des jets et des vortex dans les atmoshpères planétaires turbulentes.

Thèse soutenue publiquement le **« 4 décembre 2018 »**,
devant le jury composé de :

Monsieur, Richard, SCOTT ..... Président
Maître de Conférence, Université de Saint Andrews, Royaume-Uni
Monsieur, Peter, READ ..... Examinateur
Professeur, Université d'Oxford, Royaume-Uni
Monsieur, Xavier, CARTON ..... Rapporteur
Professeur, Université de Brest, France
Monsieur, Yves, Morel ..... Rapporteur
Directeur de recherche, CNRS, délégation Midi-Pyrénées, France

On the emergence and evolution of jets and vortices in turbulent planetary atmospheres.

Thibault Jougla

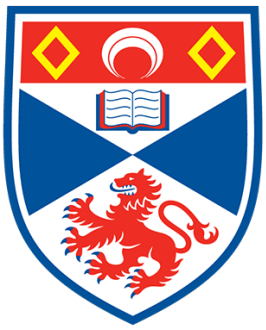

University of
St Andrews

This thesis is submitted in partial fulfilment for the degree of
Doctor of Philosophy (PhD)
at the University of St Andrews and
at the Univeristé de Grenoble Alpes.

14 December 2018

Abstract

This thesis investigates the formation and evolution of jets and vortices in turbulent planetary atmospheres using a dual approach of high-resolution numerical simulations and novel laboratory experiments. A two-layer quasi-geostrophic beta-channel shallow water model is used for the numerical study. As in Panetta (1988), a vertical shear is implemented to represent a spatially-mean latitudinal temperature gradient, which is partially maintained by thermal relaxation. Baroclinic instabilities work to erode the temperature gradient, while thermal relaxation acts to restore it. As the basic state vertical shear is unstable, the thermal relaxation cannot lead to a full recovery, thus modifying subsequent instabilities and leading to rich nonlinear dynamical behaviour.

First, we consider flow over a flat bottom, and model convective motions like those thought to occur on Jupiter by pairs of cyclones/anti-cyclones or 'hetons' as in Thomson (2016). We thereby obtain predominantly baroclinic jets, oscillating between quiescent phases, when jets are zonal and the energy is nearly stationary, and turbulent phases, when the flow loses its zonality, vortices pinch off from the meandering jets, and zonal energy components drop while eddy energy components increase. These turbulent phases typically last for a thermal relaxation relaxation period. The impacts of vertical shear (baroclinicity), thermal relaxation and heton forcing are comprehensively investigated by considering the energy transfers occurring between kinetic and potential energy, their barotropic and baroclinic parts as well as their zonal and eddy parts. This leads to a rethinking of the classic paradigm of energy transfer presented by Salmon (1982), as this paradigm is too simplistic to explain the results found.

Then, we consider the effect of large-scale bottom topography, as a first approach to understanding the role of topography in jet and vortex formation. We use the same model as in the first study but include a linearly sloping topography which has the advantage of being characterised by a single parameter, the slope. We omit the heton forcing and instead perturb the flow with a small amplitude Rossby wave initially. The main effect of heton forcing is actually to act as a kind of damping: energy fluctuations are consistently less extreme than when no forcing is used. A linear stability analysis is carried out to motivate a series of nonlinear simulations investigating the effect of topography, in particular, differences from the flat bottom case previously examined. We find that destabilising topography makes the jets more dynamic.

In the experimental part, a two-layer salt-stratified fluid is used in a rotating tank

with a differentially rotating lid to generate the shear across the interface. We consider a baroclinically unstable front in the regime of amplitude vacillation, which is found to be characterised by the sequential emergence and disappearance of a large-scale vortex. Analysing two similar experiments at the limit of geostrophy, with different Rossby numbers Ro=0.4 and Ro=0.6, shows surprisingly different behaviours, with a baroclinic dipole for small, and a barotropic vortex for the large Rossby number. The small-scale wave activity is explored using different methods, and the results suggest small, spontaneously-arising inertia-gravity waves preceding the emergence of the vortex which stirs the interface, thus having an impact on the mixing between the two layers. The recovery period of the amplitude vacillation, as well as the intensity of the vortex, increases with the Rossby number.

For further research on fronts at two-layer immiscible interfaces, a very accurate novel optical method has been developed to detect the height and slope, based on the refractive laws of optics. The associated theoretical equations are solved numerically and validated in various idealised situations.

Résumé

Cette thèse étudie la formation et l'évolution des jets et des vortex dans les atmosphères planétaires turbulentes, à l'aide d'une double approche de simulations numériques et d'expériences de laboratoire. Pour l'approche numérique, un modèle en fluides shallow-water quasi-géostrophique à deux couches dans le plan β avec des conditions canal a été utilisé. Comme dans Panetta and Held [1988], on implémente un cisaillement vertical pour représenter le gradient latitudinal (de l'équateur aux pôles) de température moyenné spatialement, qui est partiellement maintenu par un forçage thermique. Les instabilitéś baroclines affaiblissent le gradient de température, alors que le forçage thermique le restaure, ce qui crée une dynamique non-linéaire très riche.

Dans la première étude numérique, nous avons considéré l'écoulement sur un fond plat, et avons modélisé les mouvements convectifs par des paires de cyclones/anticyclones ou 'hetons' comme dans Thomson and McIntyre [2016]. Nous obtenons ainsi des jets principalement baroclines (pour une stratification atmosphérique), oscillants entre des phases calmes et des phases turbulentes, où l'écoulement perd sa zonalité. Des vortex se forment à partir des jets méandreux et l'énergie zonale diminue alors que l'énergie tourbillonnaire augmente. Ces phases turbulentes durent typiquement pendant une période de relaxation du forçage thermique. On étudie les effets du cisaillement vertical (baroclinicité), du forçage thermique et des hetons, en regardant les transferts d'énergie entre les énergies cinétiques et potentielles, leurs composantes barotropes et baroclines ainsi que leurs composantes zonales et tourbillonnaires. Ceci nous amène à repenser le paradigme classique des transferts d'énergie présenté dans Salmon [1982]. De plus, nous étudions comment une analyse de stabilité linéaire de l'écoulement zonal instantané est reliée aux phases calmes et turbulentes. Enfin, nous examinons les propriétés et les caractéristiques du profil en escalier de la vorticité potentielle.

Dans la seconde étude numérique, nous considérons l'effet d'une topographie de grande échelle, comme une première approche pour comprendre le rôle de la topographie dans la formation des jets et des vortex. Nous utilisons le même modèle que dans la première étude mais nous ajoutons un fond topographique linéaire méridionalement, qui a l'avantage de dépendre d'un seul paramètre, la pente. Une pente négative approfondit la couche inférieure par rapport à un fond plat, ce qui augmente le potentiel des instabilités baroclines, alors qu'une pente positive a un effet stabilisateur. Nous supprimons le forçage par les hetons et perturbons l'écoulement grâce à une zone de Rossby de

faible amplitude dans la couche inférieure à l'instant initial. L'effet principal du forçage par les hetons est d'agir comme une sorte d'amortissement : les fluctuations de l'énergie sont constamment plus extrêmes que sans forçage. Une analyse de stabilité linéaire est effectuée afin de déterminer les zones de stabilité et d'instabilité. Une topographie qui stabilise l'écoulement rend les jets plus dynamiques. Nous avons aussi trouvé que différentes définitions de l'échelle de Rossby reproduisent de manière qualitative le fait que l'espace entre les jets s'accroît avec la baroclinicité de l'écoulement.

Pour l'étude expérimentale, nous utilisons une cuve tournante remplie par deux couches de fluides avec une stratification au sel et un couvercle rigide en rotation différentielle. Nous étudions un front barocliniquement instable dans le régime des vacillations d'amplitude, qui est caractérisé par l'émergence et la disparition de vortex de grande échelle. L'analyse de deux expériences à la limite de la géostrophie, avec des nombres de Rossby de $Ro = 0.4$ et $Ro = 0.6$, montre des comportement très différents. Pour un faible nombre de Rossby, nous observons des dipôles baroclines alors que pour un large nombre de Rossby nous obtenons des vortex barotropes. Nous examinons l'activité des ondes de petite échelle par différentes méthodes qui révèlent la présence d'ondes d'inertie gravité comme précurseures de l'émergence des vortex. Nous étudions aussi de manière qualitative l'impact de ces vortex sur le mélange entre les couches. De plus, la période de reconstruction des vacillations d'amplitude augmente avec le nombre de Rossby.

Afin de poursuivre nos recherches sur les fronts à l'interface entre deux couches de fluides immiscibles, nous avons développé une nouvelle méthode de détection de la hauteur et de la pente basée sur les lois optiques de la réfraction. Les équations théoriques associées sont résolues numériquement et validées à l'aide de plusieurs situations idéalisées.

Declarations

Candidate's declaration

I, Thibault Jougla, do hereby certify that this thesis, submitted for the degree of PhD, which is approximately 33,000 words in length, has been written by me, and that it is the record of work carried out by me, or principally by myself in collaboration with others as acknowledged, and that it has not been submitted in any previous application for any degree.

I was admitted as a research student at the University of St Andrews in August 2015.

I received funding from an organisation or institution and have acknowledged the funder(s) in the full text of my thesis.

Date **Signature of candidate**

Supervisor's declaration

I hereby certify that the candidate has fulfilled the conditions of the Resolution and Regulations appropriate for the degree of PhD in the University of St Andrews and that the candidate is qualified to submit this thesis in application for that degree.

Date **Signature of supervisor**

Permission for publication

In submitting this thesis to the University of St Andrews we understand that we are giving permission for it to be made available for use in accordance with the regulations of the University Library for the time being in force, subject to any copyright vested in the work not being affected thereby. We also understand, unless exempt by an award of an embargo as requested below, that the title and the abstract will be published, and that a copy of the work may be made and supplied to any bona fide library or research worker,

that this thesis will be electronically accessible for personal or research use and that the library has the right to migrate this thesis into new electronic forms as required to ensure continued access to the thesis.

I, Thibault Jougla, confirm that my thesis does not contain any third-party material that requires copyright clearance.

The following is an agreed request by candidate and supervisor regarding the publication of this thesis:

Printed copy No embargo on print copy.

Electronic copy No embargo on electronic copy.

Date **Signature of candidate**

Date **Signature of supervisor**

Underpinning Research Data or Digital Outputs

Candidate's declaration

I, Thibault Jougla, hereby certify that no requirements to deposit original research data or digital outputs apply to this thesis and that, where appropriate, secondary data used have been referenced in the full text of my thesis.

Date **Signature of candidate**

Acknowledgements

First and foremost, I would like to thank my supervisors David G. Dritschel and Jan-Bert Flór for their help and guidance during these three years. I am full of gratitude for the priceless support they have offered to me throughout this PhD. They provided me with advice, wonderful discussions, bright ideas, challenging tasks, strong human interactions and exciting projects. Thank you very much.

I also want to thank the members of the Vortex group from St Andrews and of the MEIGE team in Grenoble for discussions and fantastic dinners. These three years would not have been the same without the comfort and friendship of my office mates and fellow PhD students, Crisi and Cruz. This work would not have been possible without the help of technicians, secreataries and computer scientists of the two institutions.

Finally, I want to thank my family and friends, Géraldine, Gules, Malo, Hélène, Sam and Thessa. Always present, bringing light and laughs, make joy and life to every moment, they have transformed these moments. They have stood by my side throughout, bringing light and joy to everyday life. They are both a great source of inspiration as well as one of comfort. For our scientific evenings, our discussions, and your precious help, I want to thank you.

Funding and data

I would like to acknowledge the financial support of the School of Mathematics and Statistic of the University of St Andrews and the Observatoire des Sciences de l'Univers de Grenoble, during this PhD.

Contents

Chapter 1

Introduction

Ever since ancient times, people have studied Nature, the stars and the weather, including cloud formation and precipitation. They have tried to understand the rhythm of the tides, ocean currents experienced while sailing, or atmospheric winds affecting agriculture. The first records of weather forecasting go back to the Babylonians and ancient Greeks, who used astrology and, studied the stars, the moon, and clouds to make predictions about the weather. Around 350 B.C., Aristotle wrote *Meteorologica*, a study of the weather based on the four elements. We have records of weather predictions made in China and India from the same period.

To arrive at our understanding of geophysical flows, we have to 'stand on the shoulders of Giants', as Bernard de Chartres first said during the twelfth century. We have to stand on Newton's shoulders and admire his scientific contributions, his laws of motion and his theory of gravitation. We have to stand on Cassini's shoulders for his contribution to astronomy and in particular for the first observations of the Great Red Spot (shared with Hook). We have to stand on Richardson's shoulders, on Rossby's shoulders and all the others who have shaped, step by step, our understanding of science and especially geophysical flows. In the eighteenth century, Edmond Halley and George Hadley built a model to explain the trade winds based on large-scale dynamics (see Hadley et al. [1735]). Based on this work, Gaspard-Gustave de Coriolis subsequently established the now well-known Coriolis force (see Coriolis [1835]). In the nineteen century, new technologies like the electric telegraph allowed for the analysis of information from around the globe. This set the stage for modern meteorology. The study of geophysical fluid dynamics is closely related to weather forecasts and climate sciences. The first numerical weather forecast

model was developed by Lewis Fry Richardson at the beginning of the twentieth century (see Richardson [2007]), based on work done by Bjerknes (Friedman [1993]). During the twentieth century, with the evolution of computer sciences, weather forecast predictions have made enormous progress. Now, in the early twenty-first century, we need a global but precise understanding of geophysical flows to model the climate. To understand the climate, many models run complex simulations based on numerous parameters, in which it is difficult to evaluate the impact of each parameter.

The goal of geophysical fluid dynamics in general and of simple idealised models in particular, then, is to assess the extent to which each parameter affects the climate. To do so, it is essential to understand the Earth's and ocean's fluid dynamics. As both are very similar, they can be generally modelled using the same set of equations, although certain processes like condensation differ between the two. The Earth, however, only provides a handful of examples of geophysical flows to inform our knowledge of these atmospheric and oceanic phenomena. More examples can be found on other planets and moons, like Titan, and, with the development of space observation, data from other planets, like Jupiter and Saturn – as well as from exoplanets – is becoming increasingly available. A better understanding of these planets' atmospheres (and oceans) will offer insight into our own planet's fluid dynamics.

1.1 Geophysical context

Jets and vortices are striking features present in most planets with atmospheres, such as gas giants like Jupiter or Saturn, but also telluric planets like the Earth that have an atmosphere and oceans. Size, rotation period, atmosphere depth, and composition vary from planet to planet, resulting in different kinds of jets. Jupiter exhibits strong, almost zonal jets at lower latitudes and weaker jets at higher latitudes (see Porco et al. [2003] and Ingersoll et al. [2004]). They coexist with vortices of varying intensity, such as the Great Red Spot (studied numerically by Marcus [1988], experimentally by Sommeria et al. [1988]), the white ovals (see Li et al. [2004] and Vasavada and Showman [2005]), and the polar vortices observed recently by Juno, (see Adriani et al. [2018] for more details). Saturn exhibits a very strong and wide equatorial jet, while the Earth's atmosphere has four main jets, weaker but more meandering than those on other planets. Finally, the Earth's oceans exhibit jets such as the Gulf Stream and Kuroshio, whose meanders pinch off as a series of eddies, acting as strong biological or transport barriers (see Bower et al.

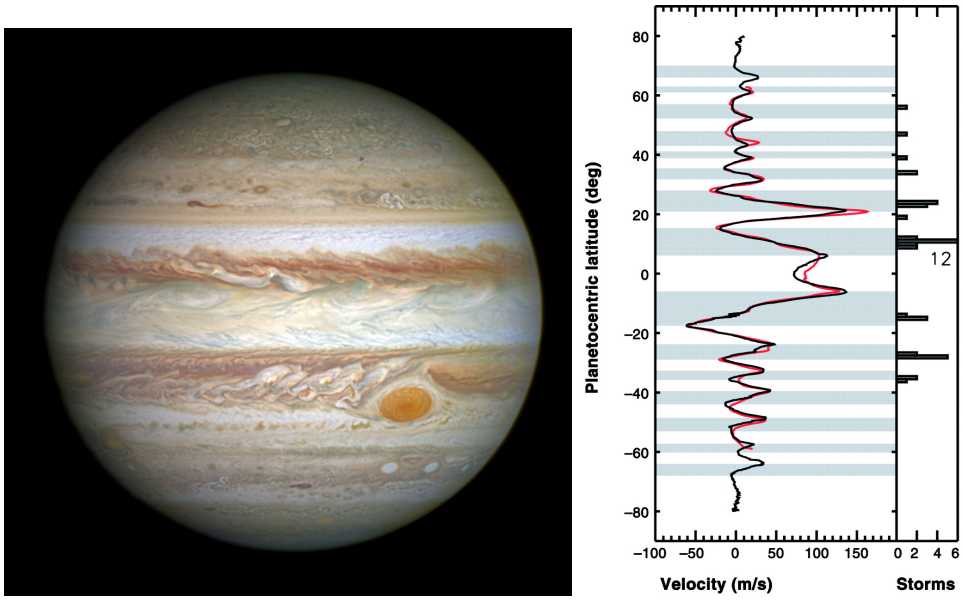

Figure 1.1: Left: Jupiter observed by NASA's space telescope Hubble in 2017. Alternating zones (white-ish) and belts (red-ish) co-existing with vortices are visible at low latitudes. Credit: NASA, ESA, and A. Simon (NASA Goddard). Right: averaged wind speed from Cassini observations in black and Voyager 2 in red. Grey and white regions correspond to belts and zones. The right panel indicates the occurrence of convective features, image from Porco et al. [2003].

[1985] and Bower [1991]).

Jupiter and Saturn exhibit beautiful, impressive patterns in their visible atmospheres. They are covered by latitudinal stripes, also called zonal bands, of various colours, as can be seen, for example, in the visible atmosphere of Jupiter captured by NASA's telescope Hubble in figure 1.1. White regions are relatively high-pressure regions of rising air called 'zones'. Their colour is due to a high concentration of ammonia clouds. Red regions are called 'belts'. They are relatively low-pressure regions where air subsides. Clouds in the belts are less dense and so less white. The reason for the red colour is not known but might be due to chemical components such as sulphur, phosphorus or carbon (see Ingersoll et al. [2004] and Sugiyama et al. [2006]).

These bands are separated by relatively narrow currents flowing in an east-west or 'zonal' direction called 'jets'. Jets separating belts and zones flow westward, i.e. retrograde where belts are located closer to the equator. Where zones are closer to the equator, on the other hand, jets between zones and belts move in an eastward (prograde) direction. Figure 1.1 displays the equatorial zone with two prograde jets on it edges adjacent to the North and South equatorial bands. Also shown is the zonal velocity profile of the Jovian

atmosphere deduced from cloud motions (image from Porco et al. [2003]). Alternating prograde and retrograde jets are clearly visible and align with the boundaries of zones and belts. Moreover, the speed of the jets decreases with latitude: equatorial jets have relatively high speeds, while mid-latitude jets are weaker, as seen in the right panel in figure 1.1.

Figure 1.2: Jupiter's Great Red Spot, an anticyclone co-existing with zonal jets. Credit: NASA.

Another prominent feature on Jupiter, beside jets, is the widespread occurrence of spots, visible on figure 1.2. These spots are vortices, which are either cyclones spinning counter-clockwise in the northern hemisphere or anticyclones, which spin clockwise in the northern hemisphere (rotational directions being reversed in the southern hemisphere). As we have seen, zones are separated by prograde jets on their equatorial edge and retrograde jets on their polar edge, so the wind speed decreases with latitude. Zones thus represent an anticyclonic wind shear. Moreover, anticyclones are always found within zones, i.e. in a cooperative shear which is known to be stabilising (see Dritschel [1990]). Conversely, cyclones are only found in belts, where the wind shear is cyclonic (see Vasavada and Showman [2005] for more details).

The most famous Jovian spot is undoubtedly the Great Red Spot, an anticyclone which has been present on the surface of Jupiter at least since humans were able to observe it. This was first reported by Hook in 1664, followed by Cassini in 1665, see figure 1.3. Thirty years before, in 1630, Niccolo Zucchi was able to detect the presence of bands thanks to the improvement of optics (see Rogers [1995]). Since then, scientists believe that there has been a persistent presence of jets and the Great Red Spot. However, the Great Red Spot was twice its current size a century ago, and is now shrinking in the

longitudinal direction (see Simon-Miller et al. [2002] and Irwin [2009]).

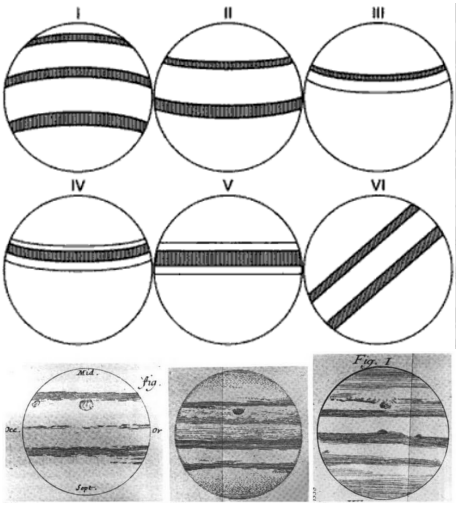

Figure 1.3: First records of Jupiter with bands and spot, drawings from the seventieth century by Riccioli and Cassini.

The peculiar case of oval BA's formation is a beautiful example of the emergence and dynamics of spots on Jupiter. The early origins of oval BA go back to 1939, when three spots emerged from the split of the South Temperate Zone, STZ, creating three white ovals called BC, DE and FA (see Rogers [1995]). In 1998, BC and DE merged to form a bigger spot called BE. Subsequently, in September 2000, BE and FA merged to create oval BA (see Sanchez-Lavega et al. [2001] for more details). Figure 1.4 shows the different steps of oval BA's formation. It also illustrates how a jet can collapse and two bands can merge.

Our knowledge of the Jovian atmosphere is closely tied to the progress in scientific instrumentation. Before Hook and Cassini, Jupiter was simply seen as a bright star (see Sachs [1974]). The evolution of optics during the seventeenth century allowed for observations of the atmosphere, namely Zucchi's observation of bands, and Hook's and Cassini's subsequent discovery of spots (see Rogers [1995]). Thanks to the continued improvement of spatial observation technology, many high-resolution images are now available. A series of spacecrafts have captured images of the planet: first Pioneer 10 and 11, followed by the Voyagers (with a 5km resolution) (see Ingersoll et al. [1981]), next the Galileo probe (see Atkinson et al. [1998], Banfield et al. [1998] and Vasavada et al. [1998]), the Cassini-Huygens mission (see Vasavada and Showman [2005] and Read et al. [2006]), the Hubble space telescope (see Simon et al. [2015]) and finally Juno, which was sent on the 4th of July 2015. The latest observations are being studied intensively and

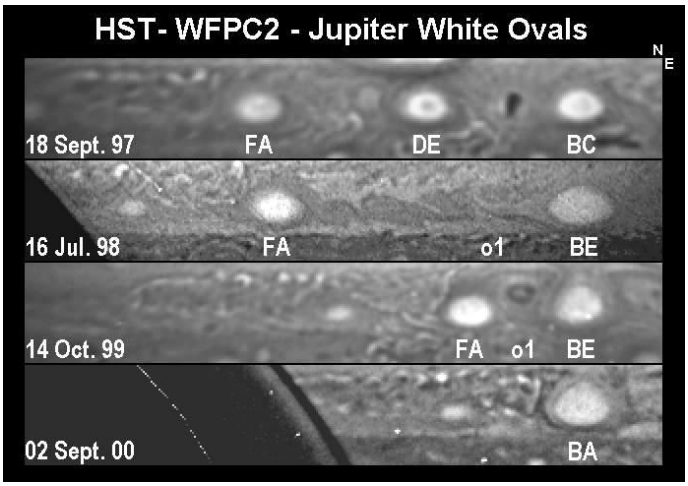

Figure 1.4: Formation of the white oval BA from the merging of three vortices FA, DE and BC. Image taken by the Hubble space telescope. Credit: NASA.

have revealed unexpected new results (see Guillot et al. [2018], Kaspi et al. [2018] and Adriani et al. [2018]). One of them is the presence of polar vortices. The north and south poles both exhibit a polar vortex surrounded by a series of circumpolar cyclones, eight around the north pole and five around the south pole, see figure 1.5 from Adriani et al. [2018].

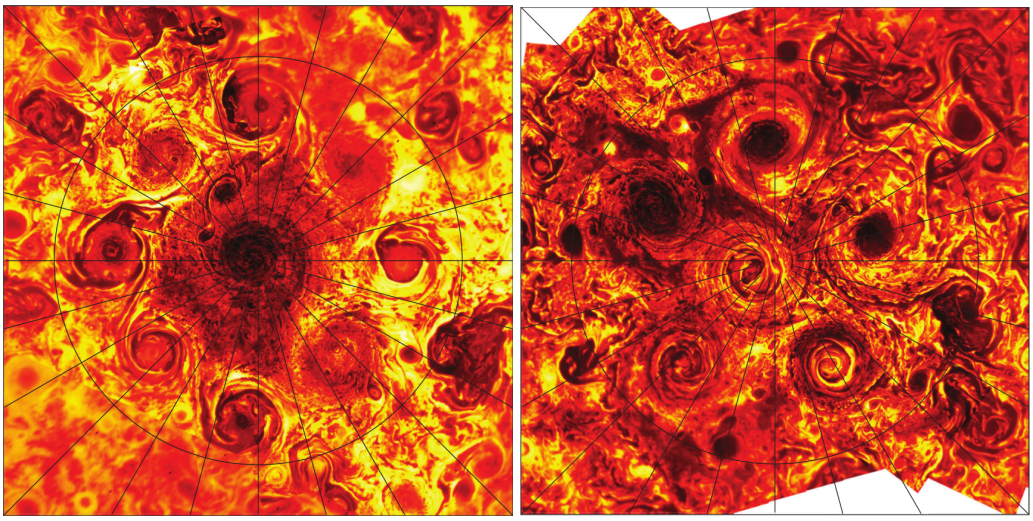

Figure 1.5: Left: Jovian north pole cyclones. Right: south pole cyclones. Credit: NASA.

To summarise, the Jovian atmosphere exhibits a series of zonal jets co-existing with long-lived vortices. Similar structures are also present on Saturn, Uranus, Neptune and, of course, the Earth. The Earth's atmosphere presents four main jets, two per hemisphere. They separate polar air masses from temperate air masses (jet streams) and temperate

air masses from tropical air masses (subtropical jets). Earth's jets are not straight purely-zonal flows but strongly meander around a mean position. They can also split into two jets before merging back. When the jet stream is north of the UK mainland, one can expect mild temperatures, as in summer 2018. On the other hand, when the jet stream is south of the UK mainland, the UK finds itself under the polar air mass, corresponding to cooler temperatures. The jet stream is therefore a useful weather forecast indicator.

Atmospheres are not the only places where jets can be found. The oceans also reveal a number of jets. Most of the Earth's main oceanic currents, such as the Gulf Stream, the Kuroshio or the Agulhas current are jets. The Gulf Stream brings warm water from the Gulf of Mexico to western Europe through the Atlantic Ocean. The Gulf Stream is a jet, with many meanders, frequently pinching off into vortices. The Kuroshio, the Pacific equivalent of the Gulf Stream and born in the warm pool of the Philippine and South China Sea, brings warm water through the Luzon strait to northern latitudes and across the Pacific Ocean. These currents are representative of the main oceanic jets. However, jets in the ocean are much more widespread. In a long time average of ocean velocity, typically ten years, a banded latitudinal organisation of the flow appears. These patterns are called 'latent' jets or 'ghost' jets (see Maximenko et al. [2005], Kamenkovich et al. [2009] and Berloff et al. [2011]).

1.2 Different approaches

When studying weather, climate and geophysical fluid dynamics in general, there are many possible approaches depending on the detail required or the questions being addressed. Models may be sophisticated, incorporating many processes, as in long-term climate prediction, or they can be idealised 'toy' models focusing on a particular aspect of the flow. In all cases, approximations are made to seek the appropriate model. Even weather forecasting models do not include all processes, since many are negligible over the forecast period. A wide range of approaches are possible. Numerical weather prediction models try to give an accurate, fine resolution forecast of the evolution of the flow from assimilated data obtained in different ways, including both satellites and ground-based observations. Such models may use different sets of equations and different numerical methods to represent phenomena that we roughly understand and know how to model, such as cloud formation, air-sea interactions, cyclogenesis, etc. However, these models are highly demanding computationally. They are complex and depend on many

parameters and parametrisations. To accurately understand the impact of one parameter on the forecast is difficult with such a model.

To study fundamental aspects of geophysical fluid dynamics, researchers commonly use idealised models. It was Bjerkness who first developed the 'primitive' equations (see Friedman [1993]). These are based on conservation of momentum and mass, with three approximations: the hydrostatic approximation, which states that the pressure gradient force is balanced by gravity, the shallow-fluid approximation, which states that horizontal scales are large compared to vertical scales, and the 'traditional' approximation, which states that the horizontal velocity is large compared to the vertical velocity. To simplify the problem, a vertically-integrated set of equations is often used, known as the shallow water equations, introduced by de Saint Venant (see de Saint-Venant [1888] for the first derivation and Vallis [2006] for more details). Another idealisation can be made: the 'quasi-geostrophic' shallow water approximation. Geostrophy refers to situations in which the horizontal Coriolis force is balanced with the pressure gradient force. The quasi-geostrophic approximation assumes a small Rossby number, which is to say that the advective time scale is long compared to the planetary rotation period. These idealised models offer different possibilities to study a problem, though many other models or approximations can be considered involving forcing, relaxation, subgrid-scale turbulence, etc. In geophysical fluid dynamics, there is a multi-dimensional parameter space that can never be completely studied. Results depend not only on parameters but often also on the initial conditions. This has led to a great diversity in models and approaches, each offering different points of view on similar problems, and collectively a better comprehension of geophysical flows.

In studies of the Jovian atmosphere, different approaches have been taken. It is still unknown if Jovian jets are due to shallow layer phenomena or to deep convection motions. The shallow layer approach supposes that Jovian jets arise in a similar manner to Earth's jets. In the Earth's oceans and atmosphere, vertical dimensions are typically much smaller compared to horizontal dimensions. Charney [1971], Dritschel et al. [1999], Reinaud et al. [2003] and Haynes [2005] have shown that the characteristic vertical scale H can be related to the Rossby deformation radius L_d by a factor f/N with N the Brunt-Väisälä frequency, i.e. $H = L_d f/N$, for rapidly rotating planets with a stably stratified atmosphere. Using the same computation as Young and Read [2017], we compute the ratio N/f for Jupiter's midlatitudes ($20°$-$40°$). Only one vertical profile of the jovian atmosphere has been captured by the Galileo probe (see Atkinson et al. [1998]). Therefore,

it is difficult to make a precise estimate of the ratio N/f. Instead, we follow Young and Read [2017] and compute a rough estimate from

$$\frac{N}{f} = \frac{g}{\sqrt{T_e c_p} 2\Omega \sin\phi} = \frac{g}{\sqrt{(S(1-A)/4\sigma)^{1/4} c_p} 2\Omega \sin\phi}$$

with $g = 23.1\text{m s}^{-2}$ (see Showman et al. [2010]), T_e the temperature of an isothermal hydrostatic atmosphere at equilibrium, we have $T_e = (S(1-A)/4\sigma)^{1/4}$, with $S = 50.66\text{W m}^{-2}$ the solar constant of Jupiter, $A = 0.343$ the albedo, $\sigma = 5.670373 \times 10^{-8}\text{Wm}^{-2}\text{K}^{-4}$ the Stefan-Boltzmann constant, $c_p = 12360\text{JK}^{-1}\text{kg}^{-1}$ the specific heat capacity, $\Omega = 1.75865 \times 10^{-4}\text{rad s}^{-1}$ the rotation rate, and ϕ the latitude (all these values come from Young and Read [2017]).

We obtain

$$\frac{N}{f} = \frac{56}{\sin\phi} = [324, 164] \quad \text{for} \quad \phi \in [20°, 40°].$$

So, the ratio of stratification over rotation on Jupiter is of the order of 10^2. One of the approaches to study Jovian jets is to consider that horizontal scales are larger than vertical scales (ratio N/f) and that the shallow water approximation can be applied. Under this assumption, using the shallow model approach, jets are mainly due to an upscale cascade of geostrophic turbulence (see Williams [1978], Sukoriansky et al. [2007] and Scott and Dritschel [2012]). Another approach states that jets are the external signature of deep convective patterns. The flow is organised at large scales in deep concentric rotating cylinders with visible bands representing their external print, and jets representing their boundaries (see Busse [1970] and Kaspi et al. [2009]). The following paragraphs discuss the two different approaches in more details.

The shallow layer approach assumes that jets are due to an upscale cascade of energy (cascade to small wavenumbers). This energy accumulates at the Rossby deformation wavenumber as in the Earth's atmosphere. Williams [1978], using a barotropic vorticity transfer model forced by stochastic forcing and a quasi-geostrophic baroclinic two-layer model originally developed by Phillips [1951], reproduced the main large-scale phenomena observed on Earth and Jupiter. He found that large-scale dynamics are mainly controlled by barotropic phenomena but that eddy turbulence is necessary for the inverse energy cascade which brings energy to large scales and specifically to jets. He also shows that baroclinic instabilities are a potential candidate for smaller-scale phenomena and for

energy and vorticity inputs that can create large-scale vortices, for example the Great Red Spot or latitudinal temperature variations. Cho and Polvani [1996] went a step further in the development of shallow models, using a spherical shallow-water model varying the rotation and the deformation radius. Imposing Jupiter's parameters, they obtained Jupiter-like motions with most of the main features, like latitudinal variations of bands and jets. While this model uses freely decaying turbulence, Showman [2007] forces only with anticyclones and Scott and Polvani [2007] uses a forced-dissipative shallow-water spherical model. They showed that the balance between the dissipation and the forcing is crucial for the stability of jets.

From equator to poles, there is an enormous variation of planetary vorticity. Baldwin et al. [2007] and Dritschel and McIntyre [2008] have shown that this planetary vorticity is essential to explain jet formation. The classic turbulence theory predicts a uniform mixing, but this is prevented by planetary vorticity. The down-gradient (diffusive-like) mixing tends to homogenise the potential vorticity (PV) in zones and locally decreases the PV gradient. This increases the shear, leading to a positive feedback (more mixing). However, the overall planetary vorticity contrast cannot be mixed away, and therefore jets must arise where PV gradients are intensified. In short, turbulent mixing in flows supporting Rossby waves is heterogeneous, and tends to create staircase-profiles of PV.

Thomson and McIntyre [2016] used a doubly-periodic $1\frac{1}{2}$-layer quasi-geostrophic β-plane model to study jets and vortices co-existing on Jupiter. Following Dowling and Ingersoll [1989], they applied a bottom topography to model the impact of deep, intense jets of the dry-convective layer on the weather-layer. These jets act as guide-rails for the weather-layer. They obtained statistically steady, straight jets in the weather-layer, without any large-scale dissipation. Additionally, stochastic forcing was added to model the convective motions in the weather layer. This forcing was implemented as pairs of cyclones/anticyclones, called 'hetons', and was more intense in belts than zones to be more realistic. They were able to reproduce long-lived vortices co-existing with jets for a specific forcing regime. Moreover, a good qualitative reproduction of the activity of zone and belt vortices was obtained. Specifically, they studied the migration of vortices from belts to zones and investigated the possibility of the weather-layer being at or close to the margin of shear stability.

Over time, different experimental approaches have also been used to study fundamental aspects of planetary circulations. The genesis of experiments in geophysical fluid dynamics goes back to James Thomson's Bakerian lecture in 1882, entitled *the great cur-*

rents of the atmospheric circulation. In it, he proposed using a ring filled with water, heated at the bottom and cooled at or close to the surface to observe the main large-scale phenomena of the Earth's atmosphere. He suggested varying different key parameters, i.e. rotation, height of water, and imposed temperatures. This was a pioneering approach to geophysical fluids experimental studies, and the essential features have remained unchanged to this day.

Hide was the first to make some important changes to the structure of these experiments: Hide [1953] and Hide [1958] started to conduct experiments using three concentric rings on a rotating table. The internal ring contained cold water maintained at a stable temperature, the external ring contained hot water also maintained at a stable temperature, while the middle ring — the so-called convection chamber — is where the dynamics takes place. By varying different parameters such as rotation speed and stratification, Hide observed baroclinic instability occurring over a range of azimuthal wavenumbers in this rotating tank.

Fifteen years later, Hart [1972] used a two-layer experiment with a rigid lid spinning faster than the mean flow to create a vertical shear to obtain an experimental representation of the Phillips model, see Phillips [1951], where he could observe baroclinic instabilities. Baroclinic instabilities have been experimentally investigated using various methods, different forcings, the use of a rigid lid, or thermal heating and cooling, in a variety of different parameter regimes. Depending on the parameter regime, various phenomena can be observed. For small Burger numbers ($Bu = g'H/f^2L^2$), the flow oscillates between different patterns. This is called vacillation or amplitude vacillation, and was first introduced by Hide [1958] and next developed by Hart [1972], Lovegrove et al. [2000], Williams et al. [2005]. Additionally, Flór et al. [2011] and Scolan et al. [2014] have studied amplitude vacillations using a two-layer salt-stratified rotating tank with varying parameters. By exploring different regimes here, too, it was possible to study the dynamics of fronts and vortices, and to observe different waves and instabilities, like inertial-gravity, Kelvin-Helmholtz, Holmboe and baroclinic instabilities.

Baroclinic instability is a fundamental mechanism in geophysical flows that plays a major role in the turbulent mixing occurring in oceans and in the planetary atmospheres (see Galperin et al. [2004], Maximenko et al. [2005] and Richards et al. [2006] for more details). These instability leads to small-scale eddies that seem to be essential for the formation of zonal jets through energy conversion. Through an inverse energy cascade, energy is transformed from a large-scale input down to small scales thanks to baroclinic in-

stability, before being converted to barotropic energy and back to large scales, see Salmon [1982] and chapter 2 for more details.

Jets have been studied using different methods on different experimental apparatus. Read et al. [2007] conducted an experiment on the Coriolis platform, a rotating tank of thirteen-meter diameter which mimics vertical convection by spreading dense salty water on the top surface and applying a β-topography. They observed large-scale zonal structures separated by the Rhines scale. Matulka and Afanasyev [2015] studied oceanic-like jets formation in a baroclinic two-layer flow on a polar β-plane, obtaining jets driven by eddy-forcing.

Gas giants are mainly composed of light elements, primarily hydrogen and helium. So instead of having a solid surface as found on telluric planets, their surfaces hold fluids only. There might be a small core not larger than a tenth of the radius (see Guillot [1999]), which was either originally the seed of the planet (see Lissauer [1993]) or was formed at the early age of the planet when no convective motions were taking place (see Boss [1998]). In this context, Busse [1970] and Busse [1976] have investigated the possibility of using Taylor-Proudman cylinders, i.e. concentric cylinders that showcase jets as their visible external footprint. Several studies have been conducted following this approach. Aurnou and Olson [2001], Christensen [2002] and Aurnou and Heimpel [2004], for example, used 3D numerical models to reproduce and continue the work started experimentally by Busse [1970], and obtained jets from the interaction between rapidly rotating concentric cylinders.

Glatzmaier et al. [2009] and Kaspi et al. [2009] built a 3D non-hydrostatic general circulation model to investigate different density profiles. They modelled the differential rotation by using the expansion of rising fluid and the contraction of sinking fluid to obtain jets. Using a similar general circulation model, Liu and Schneider [2009] reproduced the general aspect of Saturnian and Jovian large-scale dynamics, with jets extending down to depths where drag becomes strong. Spiga et al. [2015] also used a general circulation model to look at the impact of aerosol layers, ring shadowing and internal heat flux to study Saturnian dynamics. In the meantime, several groups developed laboratory experiments to test this approach; Cardin and Olson [1994] used a rotating sphere with an imposed latitudinal temperature gradient and a non-intrusive acoustic detection method to capture the flow behaviour. Egbers et al. [2003], on the other hand, used two concentric spheres in zero-gravity with different temperatures to create convective cells. They employed Schlieren methods and optical index variations due to temperature changes and

Particle Image Velocimetry (PIV) to detect the flow features.

Even if neither the shallow nor the deep approaches model Jovian jets realistically, both shed light on the possible mechanisms at play. While the shallow approach allows us to better understand the Earth's atmospheric and oceanic dynamics, the deep approach allows us to better understand solar and terrestrial convective motions. Moreover, these two methods have widespread applications in geophysical flows.

1.3 Our approach to the problem

As said previously, geophysical fluid dynamics problems are multi-dimensional parameter space problems where choices have to be made regarding experimental, numerical, statistical, theoretical, and model options, the level of idealisation, the forcing considered, the initial conditions, etc. In this thesis, we consider both experimental and numerical approaches allowing us to gain a broader understanding of the mechanisms responsible for the emergence of jets and vortices as well as their evolution in turbulent planetary atmospheres. These choices inevitably represent trade-offs. While a numerical approach allows us to study a wide range of parameters, varying numerically the values of the different parameters, there are commonly limitations in computational resources and numerical accuracy. On the other hand, in laboratory experiments using real fluids, phenomena can be observed as they happen, but the reason for the observed events may be unclear. We find a real effect of viscosity in experiments, i.e. a Reynolds number much smaller than in the Earth's and Jupiter's atmospheres. By using a dual approach of both numerical and experimental investigation, some of the limitations of either method can be overcome to obtain a more comprehensive understanding of flow behaviour.

Table 1.1 lists key parameters in the different geophysical contexts and in our numerical and experimental studies. Here a is the equatorial planetary radius for the atmospheres in km, the longitudinal characteristic lengthscale divided by 2π for the oceans in km, the dimensionless longitudinal lengthscale divided by 2π for the numerical simulations, and the radius of the tank in experiments in km. Also, U is an estimate of the zonal wind speed, Ro is an estimate for the Rossby number at midlatitudes based on U and a characteristic lengthscale of $L \simeq 2000$km for the Earth's atmosphere, 10^4km for Jupiter and Saturn, Ω is the rotation rate, g is the equatorial gravity at the surface for the planetary atmospheres and g' the reduce gravity for the experiments, and finally L_d is an estimate

	a km	U m s^{-1}	Ro	Ω rad s^{-1}	g or g' m s^{-2}	L_d/a
E. oceans	1300	0.1	0.01	7.27×10^{-5}	0.01	0.02
E. atmos.	6370	20	0.1	7.27×10^{-5}	9.82	0.3
Jupiter	71400	40	0.02	1.7×10^{-4}	23.1	0.03
Saturn	60270	150	0.06	1.65×10^{-4}	8.96	0.03
Numerics	1	0.2				0.05
Experiments	65×10^{-5}	0.01	0.5 ± 0.1	0.3	0.14	0.35

Table 1.1: Geophysical parameters and parameters used in this thesis. Blue values come from Showman et al. [2010], green values come from Vallis [2006], red value comes from Cessi and Primeau [2001], purple value comes from Olson [1991].

of the Rossby deformation length, with $L_d/a = \sqrt{Bu}$.

For the numerical part, we chose to use a two-layer quasi-geostrophic shallow water model (QGSW). While this is an idealised model, we are able to comprehensively study the primary mechanisms giving rise to jets and vortices in geophysical flows. As for the parameter space, we concentrate on variations around a chosen vertical shear, thermal relaxation and topography. The advantage of the QGSW model is its capacity to model all (small) Rossby numbers in one simulation. With such a simple model, the goal is not a quantitative reproduction of a specific behaviour but to mimic, qualitatively, observed behaviours. The reality is far too complex and poorly understood (we have little information about Jupiter's vertical structure (see Vasavada et al. [1998])). Boundary conditions represent another dimension in the vast parameter space. Geostrophic balance is problematic in spherical geometry, and full shallow-water simulations would not have allowed us to carry out a comprehensive analysis of parameter space. This, however, is possible in the mid-latitude β-plane channel geometry adopted. We sought to reach statistical equilibrium where the initial conditions do not impact the flow, in order to eliminate the dependence on initial conditions in parameter space.

Chapters 2 and 3 explore the mechanisms of jet formation, numerically, using the two-layer quasi-geostrophic framework alluded to above. First, we consider vertically-sheared (baroclinic) flow over a flat bottom in chapter 2. The dependence on various parameters is widely explored, including the amplitude of the vertical shear, the thermal relaxation rate and characteristics of the forcing (hereby known as small-scale baroclinic eddies called 'hetons'). We revisit the classical paradigm of energy transfers and dissi-

pation mechanisms and demonstrate that this paradigm is too simplistic to describe the results obtained. Moreover, we find strong intermittency, with long periods of stable jets being interrupted (randomly) by highly non-zonal 'turbulent' events. Each of these events are found to have similar characteristics, including energy transfers. Second, in chapter 3 we generalise the study in chapter 2 by including a meridionally sloping bottom topography, as a first approach to understanding the impact of broadly-varying topography on jet formation. Bottom topography directly impacts the potential for baroclinic instability, generally destabilising the flow when the topography deepens northwards, and stabilising otherwise. Moreover, topography modifies the structure and spacing of the jets, their persistence and their tendency to drift meridionally.

For our experimental study, we used a rotating tank, filled with a mix of water and alcohol in the upper layer and salty water in the lower layer. In order to create a configuration where baroclinic instabilities can occur, we put a rigid lid on the top which spins faster than the mean flow. This difference of rotation induces Ekman pumping and elevates the interface at the centre, thus creating an inverse parabolic profile at the interface between the two layers. On the sides of the interface, baroclinic instabilities may occur due to the vertical shear. By varying the Rossby number we observe different scenarios and study the formation of waves and vortices.

In chapter 4, experimental observations on the formation and evolution of waves and vortices near a front in the baroclinic unstable stage of amplitude vacillation are discussed. For two experiments, the Burger number is held fixed while the Rossby number is varied. Strikingly different dynamics are observed; one exhibiting baroclinic dipoles while the other exhibits barotropic vortices. Small- and large-scale disturbances present in the flow are considered. The impact of these disturbances on vortex formation is studied. Subsequently, the impact of the Rossby number of the flow (vortices' nature, their radius, their formation) is investigated.

Finally in chapter 5, we present a new optical method for analysing interface displacements using refractive laws of optics. This method has been built to detect the height and slope of the interface between two layers of immiscible fluid. In turn, long and detailed records of the entire interface profile can be obtained. A numerical validation of the code is presented using two virtual tanks and a series of interface profiles.

A summary of the thesis and overall conclusions are provided in chapter 6. The key findings, in particular how they further our understanding of the formation of jets and

vortices in planetary atmospheres, are discussed. Lastly, we highlight several important questions for future research.

Chapter 2

On the energetics of a two-layer baroclinic flow.

The following chapter consists of a study, Jougla and Dritschel [2017], published in the *Journal of Fluid Mechanics* and the work is reproduced here with minor modifications.

2.1 Introduction

General features of planetary atmospheres such as alternating bands and currents, exemplified by the jet streams on Earth and more prominently on Jupiter and the giant gas planets, are known to be strongly affected by planetary rotation, specifically the latitudinal variation in planetary potential vorticity (PV). Nowhere else is this better seen than on Jupiter, a rapidly rotating planet with a particularly active atmosphere [Rogers, 1995]. Observations of Jupiter in fact go back to ancient times. Babylonian astronomers first recorded the appearance of the planet [Sachs, 1974], and for them it was a bright star in the celestial sky. In 1630 with the improvement of optics, Jupiter's bands were first captured by Niccolo Zucchi. Then, Hooke and Cassini in 1664 and 1665 detected spots, now known as vortices [Rogers, 1995]. Hence, the presence of bands and vortices was already known at this time. Much more recently, spacecraft observations have revealed complex turbulent dynamics occurring in Jupiter's atmosphere, composed of quasi-zonal jets and myriads of vortices like the Great Red Spot (see Dowling and Ingersoll [1988] and Marcus [1993]).

The outer Jovian atmosphere is structured in zonal bands, called belts and zones. They are separated by jets which are strong currents flowing eastwards around the planet. Contrary to Earth's jets, Jovian jets are remarkably straight, with few large scale meanders. Hubble offers us a visualisation of the Jovian atmosphere's external layer where jets and vortices are clearly present (see Simon et al. [2015] [1]) and for previous observations see Limaye [1986] and Porco et al. [2003]). Observations of Jupiter have in turn inspired researchers to develop idealised models of the Jovian atmosphere (see e.g. Dowling [1995] and Ingersoll et al. [2004]).

Such models generally differ as regards the vertical structure of the Jovian atmosphere. Actual data are sparse: we have only a single vertical profile collected by the Galileo probe (see Atkinson et al. [1998]), which cannot be argued to be representative. To gain at least a qualitative understanding of the dynamics of Jupiter and of the gas giants generally, two main modelling approaches have been taken: a shallow model and a deep model. The shallow model (typically employing the rotating shallow water equations in a single layer) suggests that jets emerge essentially through an upscale cascade of geostrophic turbulence (Williams [1978], Cho and Polvani [1996], Kaspi and Flierl [2007], Showman [2007],Scott [2007]). By contrast, the deep model suggests that the flow is organised in deep concentric rotating cylinders, with jets their external representation, (see Busse [1970], Busse [1976]). [Kaspi et al., 2009] studied a 3D non-hydrostatic general circulation model, with a large density variation under the anelastic approximation. Unlike in models employing the Boussinesq approximation valid for weak density variations, they observe the development of baroclinic shear (a strong increase of horizontal wind speed with height). Likewise, [Liu and Schneider, 2009] and [Spiga et al., 2015] used general circulation models to study the atmospheres of the gas giants. [Liu and Schneider, 2009] were able to reproduce main features of the large-scale circulation on both Jupiter and Saturn, and found that zonal jets extend down to a depth where drag is assumed to become important. [Spiga et al., 2015] focused on Saturn and included specifically the roles of aerosol layers, ring shadowing and internal heat fluxes. They found that zonal jets develop in the troposphere and equatorial oscillations occur in the stratosphere. In summary, it has been argued that many models, having widely different formulations, capture qualitative features of planetary circulations on the gas giants.

On Earth, both the atmosphere and the oceans exhibit similar dynamical structures. The jets occurring in the oceans, however, are typically strongly meandering and unsteady

[1] Movie available at http://svs.gsfc.nasa.gov/cgi-bin/details.cgi?aid=12021

(see Maximenko et al. [2005], Kamenkovich et al. [2009] and Berloff et al. [2011]). The most well-known oceanic jets are the strong oceanic currents like the Gulf Stream and the Kuroshio. The jets occurring in the atmosphere also exhibit large-scale meanders but are generally much more well-defined than their oceanic counterparts.

[Arbic and Flierl, 2004] and [Thompson and Young, 2007] studied the impact of bottom friction on oceanic simulations. Arbic and Flierl [2004] examined the energetics behind the formation of mid-ocean eddies, while Thompson and Young [2007] focused on the role of the baroclinic (vertically varying) mode on the eddy heat flux. [Venaille et al., 2014], using a two-layer quasi-geostrophic model on the f-plane, found that for a small bottom friction the flow forms approximately barotropic (height independent) large-scale structures, which persist over a time-scale inversely proportional to the bottom friction damping rate. However, for high bottom friction, the upper layer flow dominates at leading order in the inverse damping rate. In this case, the upper flow behaves like a single-layer shallow-water flow (a $1\frac{1}{2}$-layer model) and exhibits coherent jets separating regions of nearly homogeneous PV.

To develop a conceptual understanding of Jovian jets and vortices, Thomson and McIntyre [2016] recently proposed a $1\frac{1}{2}$-layer quasi-geostrophic model based on the Dowling and Ingersoll model (see Dowling and Ingersoll [1989]), with pre-defined jets (created by an imposed lower boundary shape interface) and forced by the injection of cyclone/anti-cyclone pairs. With this idealised Jovian weather-like model, they managed to reproduce observed features such as nearly steady and straight (zonal) jets together with long-lived vortices.

The goal of the present study is to better understand the *vertical* structure of jets and vortices in a turbulent planetary atmosphere. A two-layer quasi-geostrophic shallow-water β-channel model is used to examine the formation and evolution of jets and vortices, and in particular their sensitivity to vertical shear, forcing and relaxation. Following Panetta and Held [1988], a vertical shear is imposed by relaxing to a thermal equilibrium temperature gradient — however we do not include Ekman damping or any bottom friction (see [Venaille et al., 2014] for the impact of bottom friction on a two-layer quasi-geostrophic model). Bottom friction is not relevant in shallow models of the gas giants [Thomson and McIntyre, 2016]. The vertical shear induces baroclinic instability, whose nonlinear equilibration attempts to reduce the shear. This competition between thermal forcing and baroclinic instability gives rise to the formation of baroclinic jets and, in extreme cases, to stepped PV profiles or 'staircases'. Such staircase formation

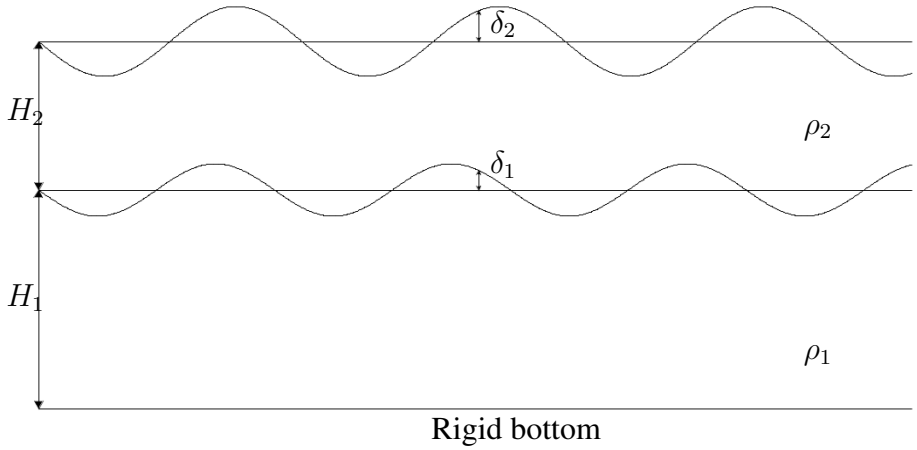

Figure 2.1: Vertical cross section of the model. Here, H_1 and H_2 are the mean layer thicknesses, ρ_1 and ρ_2 the layer densities, and δ_1 and δ_2 the displacements of the middle and upper interfaces.

has already been demonstrated in the single-layer barotropic context (see Dritschel and McIntyre [2008] and Scott and Dritschel [2012]). Additionally, in the present model small-scale stochastic forcing is imposed, crudely mimicking convective processes. This is done by adding hetons or small cyclonic/anti-cyclonic pairs in the two layers. Unlike in the model of [Thomson and McIntyre, 2016], jets do not emerge from an imposed lower boundary shape but emerge naturally from the competition between baroclinic instability and thermal relaxation.

Section §2.2 presents the model, the equations, and the boundary conditions. Section §2.3 presents the results, starting with an analysis of a characteristic simulation, followed by a detailed examination of energy transfers in section §2.4. We then focus on a turbulent event in §2.5 and discuss the wider parameter dependence in §2.6. Finally, section §2.7 presents our conclusions and a few ideas for future research.

2.2 Model formulation

To study the formation and evolution of jets and vortices in turbulent planetary atmospheres, we make use of a two-layer quasi-geostrophic (QG) β-channel model (see Phillips [1951]), with a rigid bottom and a free upper surface (see figure 2.1). It is governed by

the set of equations:

$$\frac{Dq_1}{Dt} = F_1 \quad ; \qquad \frac{Dq_2}{Dt} = F_2 \tag{2.1}$$

$$q_1 = \beta y + \nabla^2\psi_1 - \frac{f_0\delta_1}{H_1} \quad ; \qquad q_2 = \beta y + \nabla^2\psi_2 - \frac{f_0(\delta_2 - \delta_1)}{H_2} \tag{2.2}$$

$$\delta_1 = \frac{f_0(\psi_1 - \alpha\psi_2)}{g(1-\alpha)} \quad ; \qquad \delta_2 = \frac{f_0\psi_2}{g} \tag{2.3}$$

where $D/Dt = \partial/\partial t + \boldsymbol{u}\cdot\boldsymbol{\nabla}$ is the material derivative, q_i is the quasi-geostrophic potential vorticity (QGPV) in layer i, F_i includes all forcing and relaxation on the QGPV in layer i, β is the linear gradient of the Coriolis frequency $f = f_0 + \beta y$, ψ_i is the streamfunction in layer i, δ_i is the displacement of the upper interface of layer i, H_i is the mean depth of layer i, ρ_i the uniform density in layer i, $\alpha = \rho_2/\rho_1$ is the density ratio, and g is the acceleration due to gravity. We eliminate all reference to f_0, g and the total mean depth $H = H_1 + H_2$ by specifying the mean baroclinic Rossby deformation wavenumber, $\bar{k}_d$, defined through

$$\bar{k}_d^2 = \frac{1}{L_d^2} = \frac{f_0^2 H}{g(1-\alpha)H_1H_2} \tag{2.4}$$

and making use of the fractional mean layer depths $h_i = H_i/H$ whose sum is unity ($h_1 + h_2 = 1$). Then the only explicit parameters are h_1, $\bar{k}_d$, α and β.

As explained e.g. in [Vallis, 2006], the QGPV expressions in equations 2.2 derive from a series expansion of the shallow-water Rossby-Ertel PV, $q_i = (\zeta_i + f)/(h_i(1+\tilde{h}_i))$, where ζ_i is the relative vorticity in layer i, and $\tilde{h}_i$ is the fractional layer depth perturbation defined by $\tilde{h}_i = (\delta_i - \delta_{i-1})/H_i$, with $\delta_0 = 0$. The leading-order non-constant terms, for $\zeta_i/f \ll 1$ and $\tilde{h}_i \ll 1$, define the QGPV:

$$q_i = \beta y + \zeta_i - f_0\tilde{h}_i. \tag{2.5}$$

The interface displacements δ_i are related to the layer pressure perturbations p_i through hydrostatic balance (cf. Mohebalhojeh and Dritschel [2004]):

$$p_i = g\sum_{j=i}^{n}(\rho_j - \rho_{j+1})\delta_j \tag{2.6}$$

where here $n = 2$ and $\rho_{n+1} = 0$. From geostrophic balance, we have

$$p_i = \psi_i f_0 \rho_i \tag{2.7}$$

together with $u_i = -\partial\psi_i/\partial y$ and $v_i = \partial\psi_i/\partial x$. Using 2.6 and 2.7, we can re-express 2.5 for each layer as

$$q_1 = \beta y + \nabla^2\psi_1 + h_2\bar{k}_d^2(\alpha\psi_2 - \psi_1) \quad ; \quad q_2 = \beta y + \nabla^2\psi_2 + h_1\bar{k}_d^2(\psi_1 - \psi_2). \tag{2.8}$$

These may be regarded as 'inversion relations' providing the flow field $\boldsymbol{u}_i$ in each layer (via ψ_i) from the instantaneous distribution of QGPV (q_1 and q_2).

2.2.1 Stratification

Atmospheric stratification is modelled by an exponential decrease of the density profile $\rho = \rho_0 e^{-z/H_\rho}$, where ρ_0 is the density at the bottom of the domain and H_ρ is the scale height (such a profile corresponds to an isothermal basic state), see Vallis [2006], p.40. The impact of strong variations in density stratification has previously been studied by Fu and Flierl [1980] and Smith and Vallis [2002] in a two-layer quasi-geostrophic ocean model. Such variations inhibit energy transfers to the barotropic mode, thereby favouring a relatively strong upper layer flow. The same enhanced baroclinic response is found in the present results below.

The scale height is defined through $c_\rho H_\rho = H_1 + H_2 = H$, with c_ρ being the depth of the model in scale heights. We take equal layer depths $H_1 = H_2 = c_\rho H_\rho/2$, and define ρ_i to be the mean density in each layer:

$$\rho_1 = H_1^{-1}\int_0^{H_1} \rho\, dz = \rho_0 \frac{H_\rho}{H_1}(1 - e^{-\frac{H_1}{H_\rho}}) \tag{2.9}$$

$$\rho_2 = H_2^{-1}\int_{H_1}^{H} \rho\, dz = \rho_0 \frac{H_\rho}{H_2}(e^{-\frac{H_1}{H_\rho}} - e^{-\frac{H}{H_\rho}}) \tag{2.10}$$

Then the density ratio $\alpha = \rho_1/\rho_2$ is prescribed through $\alpha = e^{-c_\rho/2}$. The densities ρ_1 and ρ_2 are not explicitly needed in the model, only their ratio α is.

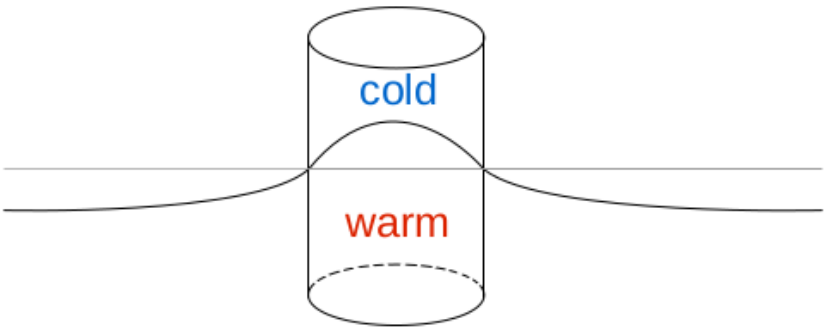

Figure 2.2: Sketch of the impact of hetons on the interface. The core of the heton is cold in the upper layer and warm in the lower layer. The interface is elevated in the core of the heton and subsides outside.

2.2.2 Stochastic Forcing

Material changes of the QGPV in each layer occur through stochastic forcing and thermal relaxation, represented by the terms F_1 and F_2 in (2.1). The stochastic forcing models in a very simple way unresolved convective motions through the spatially-random addition of 'hetons', which helps to destabilise the flow. A heton is a pair of opposite-signed PV anomalies (cyclonic in the lower layer and anti-cyclonic in the upper layer, resulting from convergence and divergence respectively) which carry heat (see [Carton, 2001]). In order to avoid any net vorticity input in either layer, a compensating uniform vorticity is added (mimicking subsidence). Figure 2.2 shows the impact of a heton on the interface. A heton is composed of an anticyclone in the lower layer and a cyclone in the upper layer. Due to thermal wind balance, this corresponds to a warm core in the lower layer and a cold core in the upper layer. The interface is thus elevated in the core of the heton. By imposing the requirement that the total integrated vorticity vanishes in each layer, the interface surrounding the hetons must be deflected downwards.

Each heton has a fixed radius $R = 0.05$ and PV amplitude q_{heton} on the highest baroclinic mode (there is no projection on the lowest mode). The frequency at which hetons are added is controlled by a prescribed (potential) enstrophy input rate η. The dependence of the flow evolution on η has been studied by using values ranging from 0.01 to 100. The dependence on the heton's radius R has also been examined but is found to have a minor effect. Notably, simulations initialised with small non-zonal perturbations and no heton forcing produce qualitatively similar results.

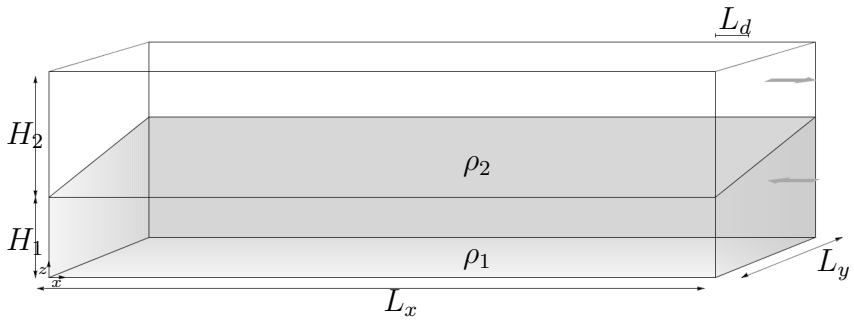

Figure 2.3: Illustration of the initial undisturbed state of a two-layer quasi-geostrophic vertically-sheared flow, with uniform westward flow in the lower layer and uniform eastward flow in the upper layer.

2.2.3 Thermal Relaxation and Vertical Shear

The thermal forcing of a planetary atmosphere generally varies from the equator to the poles. Equatorial regions typically receive more solar radiation than the poles (at lower levels). The resulting latitudinal temperature gradient implies a vertical gradient of the horizontal velocity, by thermal wind balance under the QG approximation. As in [Panetta and Held, 1988], this vertical shear is represented in a 2-layer QG model as a uniform westward flow in the lower layer and a uniform eastward flow in the upper layer, as illustrated in figure 2.3. Indeed, a negative northward temperature gradient at lower levels (in the northern hemisphere) implies a positive vertical gradient of velocity, here westward in the lower layer and eastward in the upper layer. The mean zonal velocity is kept fixed at its thermal equilibrium value at the $y-$boundaries. In the interior, the mean zonal velocity may vary as a result of baroclinic and barotropic instability.

From equation 2.8, the QGPV is linearly related to the streamfunction, which in turn is linearly related to the velocity. Adding a uniform velocity to the flow corresponds to adding a linear streamfunction profile $\psi \propto y$ and hence a linear PV profile in 2.8. Thus, vertical shear corresponds to adding a linear profile to the pre-existing background PV, βy, so that the total PV is, say, $\epsilon_i \beta y$ in each layer ($i = 1, 2$). Below, we take ϵ_1 to be a control parameter and deduce ϵ_2 from the requirements that (i) the vertical shear projects only on the vertical mode with the highest deformation wavenumber (hereafter, the 'baroclinic' mode), and that (ii) it has zero mass average ($\rho_1 h_1 \bar{u}_1 + \rho_2 h_2 \bar{u}_2 = 0$). Full details may be found in appendix §A.

To allow baroclinic instability, the potential vorticity gradients in the two layers must have opposite signs, implying $\epsilon_1 \epsilon_2 < 0$. Baroclinic instability however acts to reduce the vertical shear, leading to a quasi-stable flow. To prevent this and to allow cycles

alternating between turbulent and quiescent states, thermal relaxation is imposed to help maintain the large-scale vertical shear. The thermal relaxation here crudely corresponds to radiative forcing by the sun or internally. It acts to restore the layer interfaces δ_i to their initial thermal equilibrium profiles $\delta_{\mathsf{eq},i}$ at the rate r. This leads to non-conservative changes in the QGPV through the relation between the QGPV and interface displacement, namely (2.5) with $\tilde{h}_i = (\delta_i - \delta_{i-1})/H_i$ and $\delta_0 = 0$. To eliminate reference to f_0, g etc., it is convenient to scale the interface displacements so they have units of vorticity:

$$\tilde{\delta}_i \equiv \frac{f_0 \delta_i}{H}. \tag{2.11}$$

Owing to the relations (2.3), together with the definition of $\bar{k}_d^2$ in (2.4), we can express the scaled interface displacements as

$$\tilde{\delta}_1 = h_1 h_2 \bar{k}_d^2 (\psi_1 - \alpha\psi_2) \quad ; \quad \tilde{\delta}_2 = h_1 h_2 \bar{k}_d^2 (1-\alpha)\psi_2. \tag{2.12}$$

Then, thermal relaxation contributes the following terms to F_1 and F_2 in (2.1):

$$F_1 \leftarrow r\left(\tilde{\delta}_1 - \tilde{\delta}_{\mathsf{eq1}}\right)/h_1 \quad ; \quad F_2 \leftarrow r\left((\tilde{\delta}_2 - \tilde{\delta}_1) - (\tilde{\delta}_{\mathsf{eq2}} - \tilde{\delta}_{\mathsf{eq1}})\right)/h_2. \tag{2.13}$$

2.2.4 Boundary Conditions

We employ a channel model, with periodic conditions in x (longitude) and free-slip rigid boundaries in y (latitude). On the y-boundaries, the zonally-averaged zonal velocity is held fixed to the value imposed by the vertical shear, as in [Panetta and Held, 1988]. The model has a rigid bottom surface and a free top surface, as illustrated schematically in figure 2.1.

2.2.5 Non-dimensionalisation

We choose to employ dimensionless quantities only. To this end, we take the width of the domain to be $L_x = 2\pi$ and its breadth to be $L_y = \pi$, and, most importantly, ensure that these dimensions are much larger than the characteristic Rossby deformation length $L_d = 1/\bar{k}_d = 0.05$.[2] The total height of the model H is taken to be $c_\rho = 2$ density scale heights H_ρ, corresponding to a density ratio of $\rho_2/\rho_1 = \alpha = e^{-c_\rho/2} \simeq 0.37$, though

[2] A more representative measure of L_d is $2\pi/\bar{k}_d = \pi/10$, yet this is still much smaller than L_y.

Parameter	Symbol	Value or range considered
Longitudinal domain length	L_x	2π
Latitudinal domain length	L_y	π
Rossby deformation length	L_d	0.05
1st deformation wavenumber	k_{d1}	8.87
2nd deformation wavenumber	k_{d2}	17.93
Upper to lower layer density ratio	α	0.37 to 1
Depth in density scale heights	c_ρ	0 to 2
Fractional layer depths	h_1, h_2	0.5
Planetary vorticity gradient	β	8π
Lower layer PV gradient $/\beta$	ϵ_1	-0.5 to -0.1
Upper layer PV gradient $/\beta$	ϵ_2	2.81 to 3.79
Thermal relaxation rate	r	0 to 0.5
Enstrophy input rate	η	0.01 to 100
Heton PV amplitude	q_{heton}	1.257 to 1508
Heton radius	R	0.05

Table 2.1: Physical parameters used in the model simulations.

$c_\rho = 0.2$ and 0 have also been studied (see below). For $c_\rho = 2$ and $\bar{k}_d = 20$, and for equal layer depths $h_1 = h_2 = 0.5$, the deformation wavenumbers of each vertical mode are $k_{d1} \simeq 8.87$ and $k_{d2} \simeq 17.93$ (see appendix §A for details).

2.2.6 Parameter choices

We set the planetary vorticity gradient β to be 8π, corresponding to a Rossby wave period of unity for a barotropic disturbance with a wavenumber of $k_0 = 4$. A typical time scale emerges from the relation $T_\beta = 2\pi k_0/\beta$. We use in this study the dimensionless time $\tilde{t} = t/T_\beta$. For ease of presentation, we drop the tilde in the following. Recall that the initial PV gradients in each layer are $\epsilon_i\beta$, and the choice of ϵ_1 controls the strength of the vertical shear. Here, we consider two main values of ϵ_1, namely -0.1 and -0.5, corresponding to $\epsilon_2 \simeq 2.81$ and 3.79 respectively. For $\epsilon_1 = -0.5$, the initial mean velocities in the two layers are $\bar{u}_1 \simeq -0.094$ and $\bar{u}_2 \simeq 0.256$ (see appendix §A for details). The enstrophy input rate η controlling the injection of hetons ranges between 0.01 and 100. We consider values of the heton PV q_{heton} ranging from $1 \times \beta/\bar{k}_d$ to

$1200 \times \beta/\bar{k}_d$, whereas we fix the heton radius R at 0.05 unless otherwise stated. We vary the thermal relaxation rate r between 0 and 0.5. Section §2.6 examines the effect of variations in the parameters. A full list of the dimensionless physical parameters and the values used are provided in Table 2.1.

Over 100 simulations have been run using a variety of grid dimensions $N_x \times N_y$, for $N_x = \{128, 256, 512\}$ and $N_y = N_x/2 + 1$, over 10^4 units of time (and up to 10^5 units for very small r). Note: an extra grid point is needed in the y direction to include the boundaries and ensure each grid box is square.

2.2.7 Numerical Model

All simulations have been carried out using the 'Combined Lagrangian Advection Method' (CLAM) developed by Dritschel and Fontane [2010]. This numerical method, using a pseudo-spectral method at large scales, and Lagrangian contour advection at small scales, is both highly accurate and efficient (see Dritschel and Tobias [2012] for a recent demanding comparison). All numerical parameters follow the recommended choices outlined in Fontane and Dritschel [2009] except that twice as many PV contour levels (here 80) are used to represent the initial PV variation in each layer. The PV contour interval remains fixed in time.

2.3 Results

We begin by presenting in detail a characteristic flow simulation. The flow illustrated alternates, irregularly, between a more disturbed 'turbulent' phase and a more zonal 'quiescent' phase. The initial baroclinically-unstable zonal state rapidly breaks down and never fully recovers. The instability equilibrates into a structured flow, a quiescent phase, where regions of nearly homogeneous PV are separated by eastward jets in the upper layer and westward jets in the lower layer. Next, and as a result of the accumulative effect of thermal relaxation, this structured state destabilises and breaks down, again through baroclinic instability but on a much different basic state than was present initially. The flow becomes more turbulent and much less organised. It then recovers to a structured quiescent phase only to break down again into a turbulent phase, and so on. We pay particular attention to the flow behaviour around these turbulent phases, and we study the

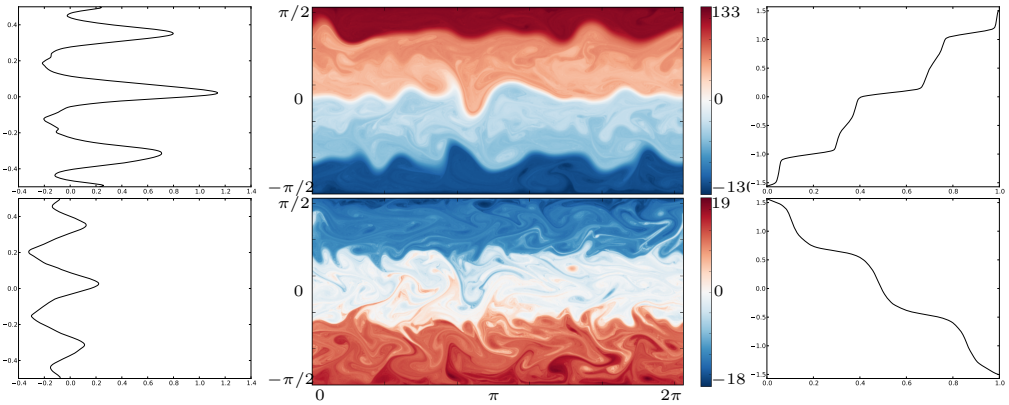

Figure 2.4: The top figures show the upper layer flow, and the bottom figures show the lower layer flow, all at $t = 3000$. Left: normalised latitude $2y/\pi$ vs zonally-averaged zonal velocity $\bar{u}_i(y,t)$. Centre: PV field $q_i(x,y,t)$ over the entire domain. Right: equivalent latitude $y_e(\tilde{q},t)$ vs normalised PV $\tilde{q} = (q - q_{\mathsf{min}})/(q_{max} - q_{\mathsf{min}})$.

changes in energy (kinetic/potential, zonal/eddy, barotropic/baroclinic) and zonal-flow stability which occur.

2.3.1 A characteristic simulation

The chosen simulation has been run on a 512×256 'inversion' grid (the effective grid resolution is 16 times finer in each direction), with a thermal relaxation rate $r = 0.01$, a stratification parameter $c_\rho = 2$, a lower-layer fractional PV gradient $\epsilon_1 = -0.5$, a heton PV $q_{\mathsf{heton}} = 1 \times \beta/\overline{k}_d$, and an enstrophy input rate $\eta = 0.1$.

At the initial time, the flow exhibits a linear slope in PV, opposite in each layer. This flow is baroclinically unstable (as explicitly shown in appendix §A), and within a few units of time leads to a strongly non-zonal, eddying, turbulent flow. This subsequently collapses and organises into bands of nearly uniform PV separated by jets. This quiescent phase, illustrated in figure 2.4 at $t = 3000$ typically lasts hundreds of time units, or several relaxation time scales r^{-1}.

The central panels in figure 2.4 show the PV field at this time in the upper and the lower layers, respectively. In the upper layer, four distinct bands of nearly homogeneous PV are present, separated by three jets flowing eastward. In the lower layer, by contrast, there are three bands of nearly homogeneous PV separated by two westward jets. As discussed in Dritschel and McIntyre [2008] and Scott and Dritschel [2012] in the context of a single-layer model, the 'equivalent latitude' PV profile $y_e(q)$ is particularly useful

for identifying jets, here seen by the nearly flat portions of the curves shown in the right panels of these figures. The formation of a staircase profile in $y_e(q)$ indicates the presence of homogeneous regions ($dy_e/dq \to \infty$) and jets ($dy_e/dq \to 0$). The function $y_e(q)$ is obtained by re-arranging the PV monotonically in each layer. In the upper layer, $y_e(q) = y_{\mathsf{min}} + A_2(q)/L_x$ where $A_2(q)$ is the area occupied by PV values having $q > q_{\mathsf{min}}$. In the lower layer, where the mean PV gradient is generally reversed, instead $y_e(q) = y_{\mathsf{min}} + A_1(q)/L_x$ where $A_1(q)$ is the area occupied by PV values having $q < q_{\mathsf{max}}$.

The right panels in figure 2.4 show $y_e(\tilde{q})$ versus normalised PV, defined by $\tilde{q} \equiv (q - q_{\mathsf{min}})/(q_{\mathsf{max}} - q_{\mathsf{min}})$, for each layer. Both layers exhibit a near staircase profile, but it is most distinct in the upper layer. The three main small gradient portions of the curve seen here correspond to the strong eastward jets seen in the zonally-averaged zonal velocity $\bar{u}_2$ (upper left figure), while the four high gradient portions correspond to the nearly homogeneous PV regions. The zonal flow in these regions is weakly westwards. In the lower layer, the two (central) small gradient regions in $y_e(\tilde{q})$ correspond to westward jets (see lower left panel). Between the westward jets in this layer one also sees eastward jets of comparable magnitude. These are induced by the strong PV gradients in the upper layer. PV inversion couples the layers together so that the flow in either layer depends on the PV in both layers. Here however the lower layer PV is relatively weak, so it has much less impact on the upper layer flow than has the upper layer PV on the lower layer flow.

Overall, the observed jets are not vertically coherent. Jet intensities strongly vary from one layer to another. This implies that the baroclinicity of the flow is important. The two layers have different numbers of jets. Jets flow eastward in the upper layer and predominantly westward in the lower layer. Moreover, the upper layer jets are much faster than the lower layer jets. Additionally, signatures of the jets in one layer are visible in the PV field of the other layer. In the upper layer (central panel), the transitions between the two sky/pale blue bands, and between the pink-reddish bands (the two middle bands) coincide with the locations of the lower layer westward jets. These signatures appear in the equivalent latitude $y_e(\tilde{q})$ (upper right panel) as small swerves in the middle of the two high gradient portions. In the lower layer, the signatures of the upper layer jets are less obvious, but are visible in the zonally averaged flow, an effect of PV inversion mentioned above. Jet signatures in PV are less evident in the lower layer in part because the flow is more disturbed at small scales there. These transitions could also be due to mixing around jets as demonstrated in Scott and Tissier [2012].

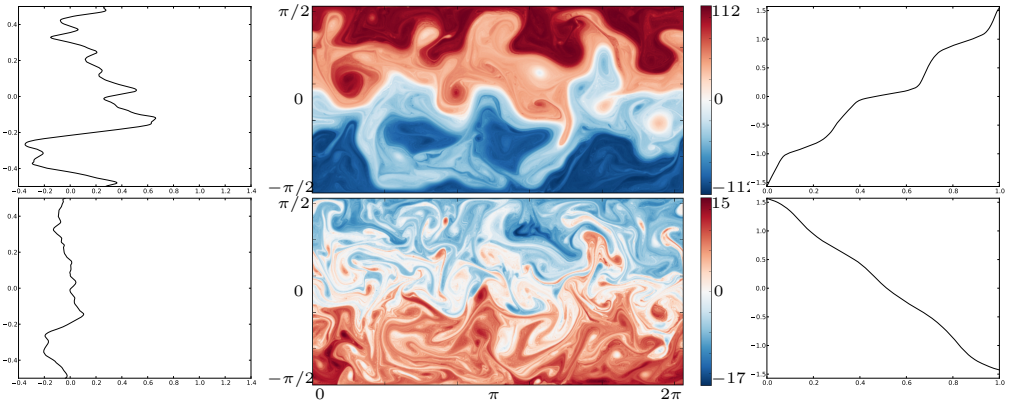

Figure 2.5: The top figures show the upper layer flow, and the bottom figures show the lower layer flow, all at $t = 4000$. Left: normalised latitude vs zonally-averaged zonal velocity (Note that plot scale for u are the same as in figure 2.4). Centre: PV field over the entire domain. Right: equivalent latitude $y_e(\tilde{q}, t)$ vs normalised PV.

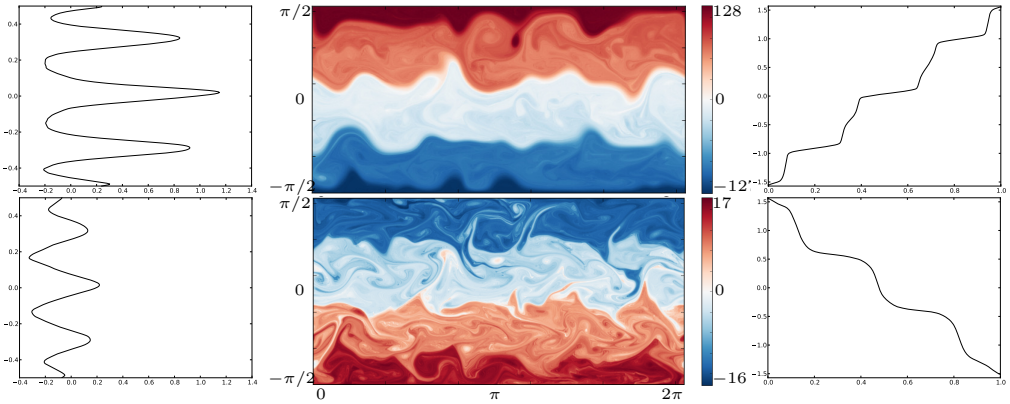

Figure 2.6: The top figures show the upper layer flow, and the bottom figures show the lower layer flow, all at $t = 9400$. Left: normalised latitude vs zonally-averaged zonal velocity (Note that plot scale for u are the same as in figure 2.4). Centre: PV field over the entire domain. Right: equivalent latitude $y_e(\tilde{q}, t)$ vs normalised PV.

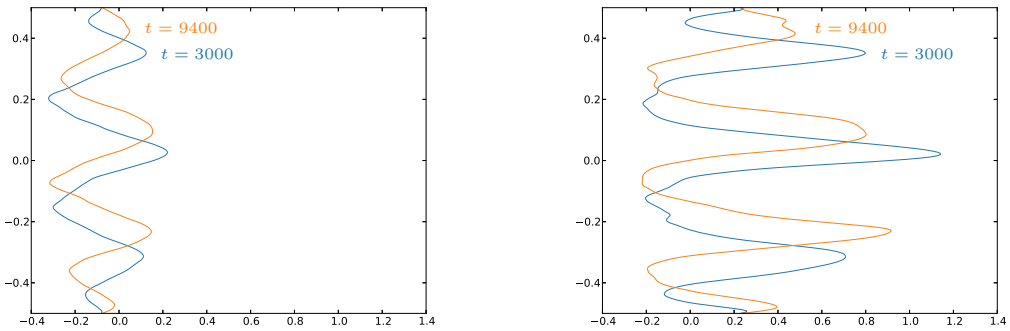

Figure 2.7: Lower layer (left figure) and upper layer (right figure) zonally-averaged zonal velocity $\bar{u}_i(y, t)$ at two different times $t = 3000$ blue and $t = 9400$ orange.

Figure 2.5 illustrates the same flow at a later time $t = 4000$, during a turbulent phase. The flow is substantially less zonal, with large-amplitude excursions exhibited in the PV field in both layers. Remarkably, nearly homogeneous regions persist in the upper layer though they are much more disturbed than in the quiescent phase. Moreover, the jets are considerably weaker and virtually absent from the lower layer flow. The 'jets' seen in the upper layer are not steady and show no obvious relation to the equivalent-latitude PV profile $y_e(\tilde{q}, t)$. A series of short-lived vortices can be seen, especially in the central regions of the flow. These formed from the buckling and breaking of the jets at earlier times and re-merge with the jets subsequently. Two movies of the PV evolution are available in the online supplementary material.

Various statistics summarising the time evolution of the flow are provided in figure 2.8. From top to bottom we show the equivalent PV $q_e(y)$ (the inverse of the function $y_e(q)$) in the upper and lower layers as Hövmoller diagrams, the zonal and eddy kinetic energy in the first 'barotropic' and second 'baroclinic' vertical modes, the zonal and eddy potential energies, the maximum growth rate of the instantaneously zonally-averaged flow versus zonal wavenumber, and the meridionally-integrated spectrum of the available potential energy (APE) versus zonal wavenumber. In each plot, time is in the abscissa.

The equivalent PV Hövmoller diagrams allow one to identify major changes in the flow structure, such as a latitudinal shift of the jets and homogeneous regions. We can see here the entire evolution of the flow, starting with the first rapid re-organisation of the flow from its unstable initial state, to the alternation between quiescent phases and (relatively short) turbulent phases.

The initial linear PV variations $\epsilon_i \beta y$ are short lived after the flow destabilises and evolve into nearly homogeneous regions separated by jets, or staircase profiles, by $t = 500$. This is the beginning of the first quiescent phase. Four nearly homogeneous regions are clearly identifiable in the upper layer and between them three jets are present. The lower layer at this stage has three nearly homogeneous regions with two westward jets separating them. Over the next 1600 units of time, the innermost homogeneous regions narrow slowly but progressively, due to the accumulative effects of thermal relaxation (this does not occur in the absence of relaxation). Near $t = 2100$, the quasi-zonal flow is disrupted and a short turbulent phase occurs, lasting no more than approximately 100 days, which is the thermal relaxation time-scale, r^{-1}. The flow then recovers, this time significantly more rapidly than it did following the initial instability, and enters a second quiescent phase, illustrated in figure 2.4 at $t = 3000$.

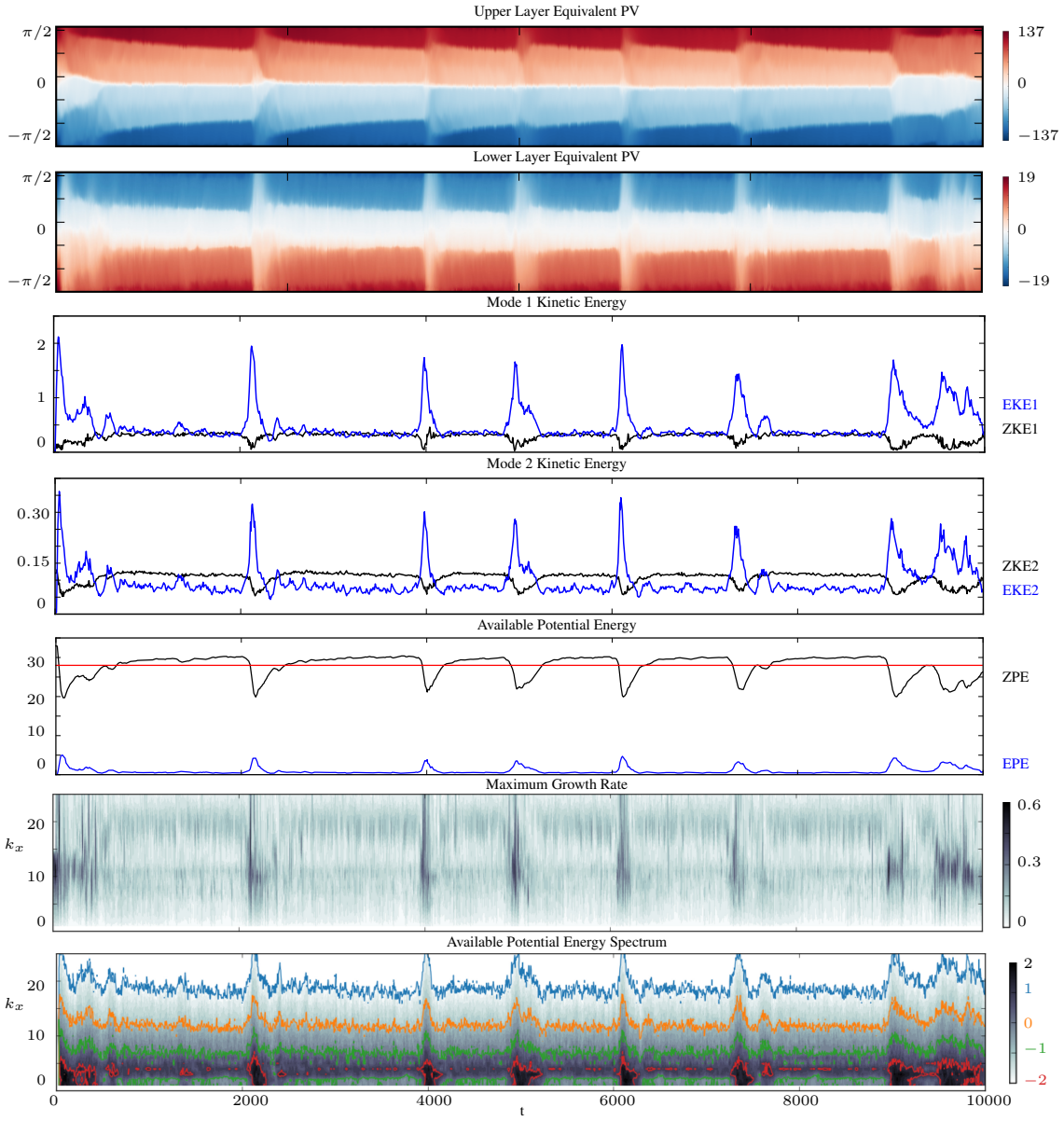

Figure 2.8: (a,b) Hövmoller diagrams of the equivalent PV $q_e(t, y)$, with latitude in the ordinate. (c,d,e) Energy components (with the eddy part in blue, the zonal part in black and the red line the time averaged APE). (f) $\log_{10}$ of the maximum growth rate of the zonally-averaged flow versus zonal wavenumber k_x. (g) $\log_{10}$ of the meridionally-integrated spectrum of available potential energy versus zonal wavenumber k_x. The coloured contours correspond to specific values of the spectrum as indicated on the colourbar. In all of these plots time is in the abscissa.

Over the next 1900 units of time, the same progressive thinning of the innermost homogeneous regions occurs, disrupted by a turbulent phase around $t = 4000$, illustrated in figure 2.5. This sequence of long quiescent and short turbulent phases continues with irregular frequency almost to the end of the simulation. At around $t = 9000$, the flow passes through a turbulent event and organises into an anomalous quiescent phase, similar to that seen after the initial instability near $t = 0$, see figure 2.6. Instead of having a symmetric flow with a centered jet, the flow exhibits a shift of the jets and homogeneous regions as shown in figure 2.7.

This anomalous quiescent phase is significantly more active and non-zonal than previous such phases. It is also found in other simulations and is discussed further in §B below.

The energy diagnostics closely correlate with the variations seen in the equivalent PV Hövmoller diagrams. Each turbulent phase is characterised by a strong peak in the non-zonal, eddy component of the energy and a dip in the zonal component. For the barotropic (mode 1) kinetic energy, the eddy energy (EKE1) is always comparable or greater than the zonal part (ZKE1). The baroclinic (mode 2) kinetic energy is smaller, with the eddy part (EKE2) surpassing the zonal part (ZKE2) only during turbulent phases. On the other hand, the potential energy is much larger: even the eddy potential energy (EPE) is greater than any component of the kinetic energy. The zonal potential energy (ZPE) is more than 10 times any component of kinetic energy. This dominance of ZPE is seen in all simulations conducted. Note: here we mean the 'available' potential energy (APE) relative to a resting basic state (APE measures the mean-square displacement of the layer interfaces).

The maximum growth rate of the instantaneous zonally-averaged flow (second panel from the bottom in figure 2.8) shows that the turbulent phases coincide with periods of relatively strong baroclinic instability, involving zonal wavenumbers k_x mainly between 5 and 20. Note that the instability is not in fact purely baroclinic, except in the initial stages when the mean flow is a simple baroclinic shear. In general, there is a projection on the barotropic mode as well when the zonal mean flow is more complex (see e.g. [James, 1987], who examined the influence of barotropic shear on baroclinic instability). It appears that the instability precedes the growth in the eddy energy components, but in fact it occurs after these components have already grown significantly (this is shown below in detail). Hence, it is too simplistic to think that the thermal relaxation has led to an unstable zonal flow state, which then becomes turbulent. The non-zonal flow must

also play a role, but this cannot be assessed simply through a linear stability analysis.

Finally, in the bottom panel in figure 2.8 we show the meridionally-integrated APE spectrum as a function of zonal wavenumber k_x (between 1 and 25) and time. At the very earliest stages, $t \leq 10$, baroclinic instability excites wavenumbers centred on $k_x = 11$ (as found in the linear stability analysis). Very soon after, a broad spectrum of disturbances emerges, with dominant power residing at much lower wavenumbers, around $k_x = 4$ and to a lesser extent $k_x = 6$. This is typical of quiescent phases, and indicates a significant and persistent amount of eddy activity even during these phases. The turbulent phases on the other hand are characterised by the excitation of a broad range of wavenumbers, both lower and higher. This spreading is characteristic of turbulent flow evolution. Each turbulent phase appears to first spread APE to higher wavenumbers then build up energy at low wavenumbers, predominantly $k_x = 2$ and 3. This is short-lived however as the flow returns to a quiescent phase.

2.4 Energy Transfers

We next look more closely at the energy transfers taking place between different energy components (kinetic/potential, barotropic/baroclinic, zonal/eddy) to gain a better understanding of the flow changes occurring when entering and leaving turbulent phases. To be more quantitative, we define a turbulent phase as a period when the ZPE is smaller than the mean ZPE. Other definitions have been tried, but this simple definition adequately identifies turbulent phases, as seen in figure 2.8.

To study energy transfers, we examine two different kinds of instantaneous correlations between the six energy components ZKE1, ZKE2, ZPE, EKE1, EKE2 and EPE. Note that it is not possible to express the rate of change of any one component solely in terms of the other components, so one must seek other means to examine the energy transfers taking place. We have chosen correlations, separated into turbulent and quiescent phases, together with directions of energy change, as explained below.

The first correlation is the standard one, defined for two time series $\{x_1, x_2, ..., x_n\}$

and $\{y_1,\, y_2,\, ...,\, y_n\}$ by

$$r_{xy} = \frac{\sum_{i=1}^{n}(x_i - \bar{x})(y_i - \bar{y})}{\sqrt{\sum_{i=1}^{n}(x_i - \bar{x})^2 \sum_{i=1}^{n}(y_i - \bar{y})^2}} \tag{2.14}$$

where $\bar{x} = n^{-1}\sum_{i=1}^{n} x_i$ and $\bar{y} = n^{-1}\sum_{i=1}^{n} y_i$. The second one, which we call the 'global correlation', is defined by the numerator of (2.14) only. This gives a better measure of the energy magnitudes involved and, in particular, helps to identify the key components involved in the energy transfers taking place. In the results presented, data have been sampled every 5 units of time, providing energy time series of $n = 2001$ values.

Figure 2.9 shows three scatterplots of different energy components and the standard correlation matrix. First, the correlation matrix exhibits three distinct areas. The two red areas show that zonal energies are positively correlated with each other, and that eddy energies are also positively correlated with each other. The blue area shows that zonal energies are negatively correlated with eddy energies. This finding agrees with that found in figure 2.8 for the evolution of the energy components, namely that when there is a decrease of any zonal energy the other zonal energies also decrease and the eddy energies increase, and vice versa.

In the scatterplots, further information can be obtained. First of all, we see the strong, tight correlation between ZKE2 and ZPE (top left figure), consistent with the value of 0.94 seen in the correlation matrix. Moreover, the eddy energies are all tightly and positively correlated (only EKE2 vs EPE is presented here in the bottom left figure). The scatterplots exhibit a racquet shape, very narrow at the base, corresponding to the quiescent phases, and more spread at the top, corresponding to the turbulent phases. Moreover, there is a definite pattern of evolution: the flow leaves a quiescent phase with relatively low EPE, gains EPE during the peak of the turbulent phase, then returns to the quiescent phase with relatively high EPE.

Similar looping patterns are present in the zonal versus the different eddy scatterplots, as well as in both the ZKE1 versus ZKE2 and ZKE1 versus ZPE scatterplots. However, only three of these scatterplots are shown to demonstrate this point. These patterns are more widely spread than seen between the eddy energies themselves. If we look at ZPE versus EPE (top right figure), we see that ZPE diminishes as EPE grows when leaving a quiescent phase, following nearly a straight line. It then returns along a curved line

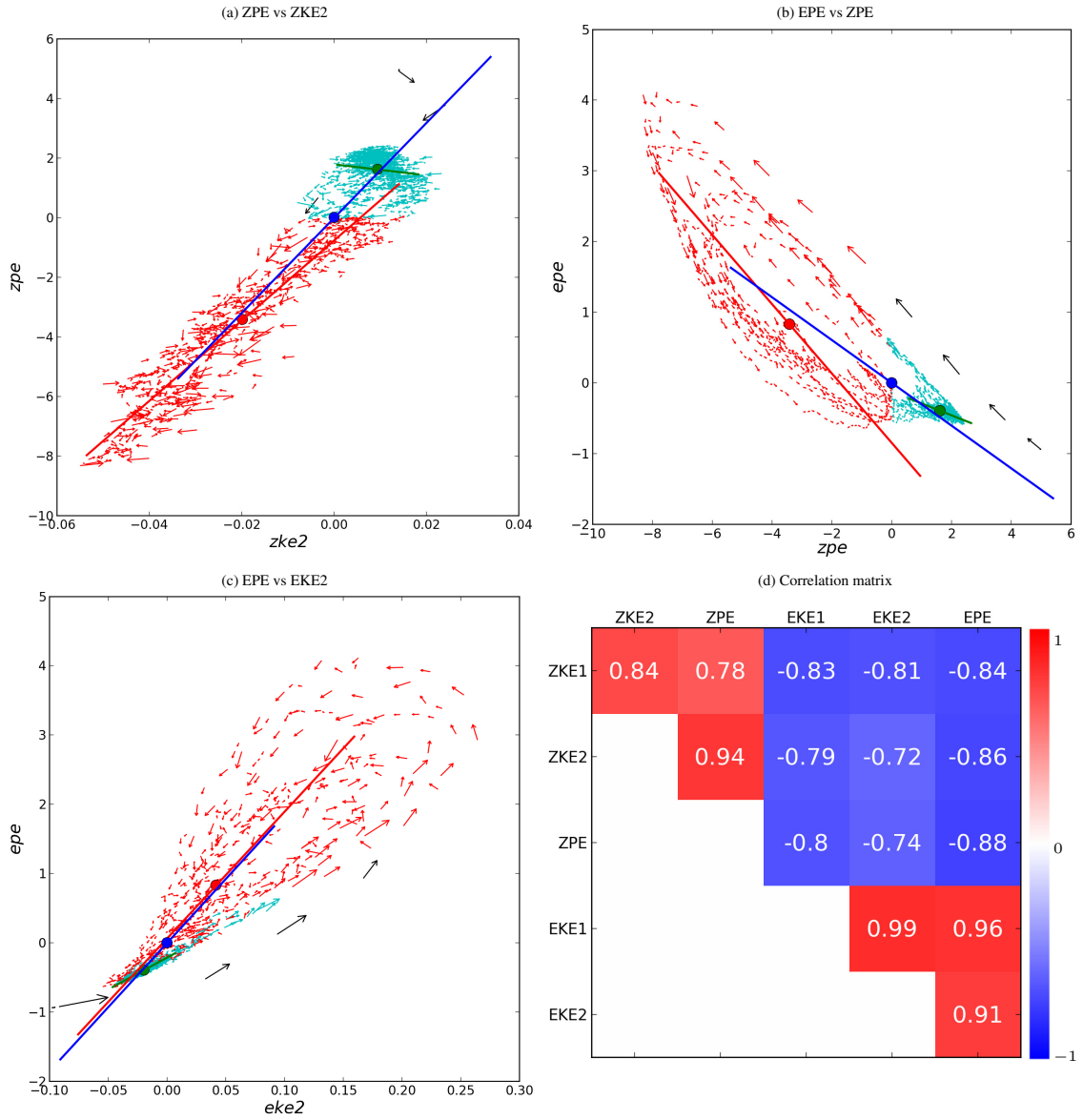

Figure 2.9: (a, b, c) Scatterplots of different energy components in the characteristic simulation, for (a) ZPE vs ZKE2, (b) EPE vs ZPE, and (c) EPE vs EKE2. Note: the mean values are subtracted and the scales are adjusted to the range of energy values observed. The arrows represent a third of the distance between adjacent points. Black arrows: initial phase. Cyan arrows: quiescent phases. Red arrows: turbulent phases. The lines show the best fit of the data (cyan for quiescent phases, red for turbulent phases, and blue overall), after optimal rotation of the data and a least-squares fit. The lengths of the lines are proportional to the spread in the data. (d) The standard correlation matrix is shown, computed using (2.14) for the different energy components.

to recover from a turbulent phase. During this recovery, EPE falls relatively quickly while ZPE does not show much growth until near the end of the turbulent phase. This slow recovery of ZPE is likely due to the weak thermal relaxation. The nearly straight lines, leaving quiescent phases and entering turbulent phases, are all closely parallel. The more eccentric one, with black arrows, corresponds to the initial stages where baroclinic instability acts on an idealised basic state. All the other straight lines are parallel to this one because the same phenomenon happens: ZPE is converted into EPE due to baroclinic instability. However the zonal energy at the beginning of subsequent turbulent phases is lower than it was in the initial phase, explaining the gap between the different lines.

A difficulty in the interpretation of these results arises because the scatterplots are two-dimensional projections of a six-dimensional phase space. The loop patterns seen imply that other components not shown in a given 2D cross section are involved in the energy transfers taking place, and moreover that the transfers are not occurring simultaneously (this is highlighted in §2.5). An alternative interpretation, discussed next, focuses on the energy components exhibiting the greatest variations.

The standard correlation scatterplots in figure 2.9 show the correlation between different energy components, but not the energy transfer. To see the energy transfer, it is necessary to use the same plot limits in all scatterplots and to correlate the energy components using only the numerator of (2.14). These global correlations are exhibited in figure 2.10 in the same format as figure 2.9 for comparison. The main energy transfers involve just a few components, ZPE, EPE and to a weaker extent EKE1 and ZKE1. The other components have essentially no impact on the global energy transfer. In particular, some components which show a strong standard correlation instead show a very weak global correlation, such as ZKE2 versus ZPE. This means that ZKE2 and ZPE evolve similarly but there is scarcely any energy transfer between them.

The dominant energy transfer occurs between ZPE and EPE and is strongly anti-correlated, as expected. ZPE is also anti-correlated with EKE1, implying that both EPE and EKE1 are the dominant components uptaking any change in ZPE. This is consistent also with the positive correlation between EPE and EKE1. Finally, and perhaps surprisingly, only one correlation between zonal energies, ZPE versus ZKE1, is notable. For a relatively large gain in ZPE, there is a modest increase in ZKE1. Evidently, the thermal restoration of the sloping layer interfaces favours an increase in barotropic energy. Restoration of a linear slope would not have this effect, as a linear slope only generates a baroclinic flow, by construction. Instead, it must be that the eddying motions

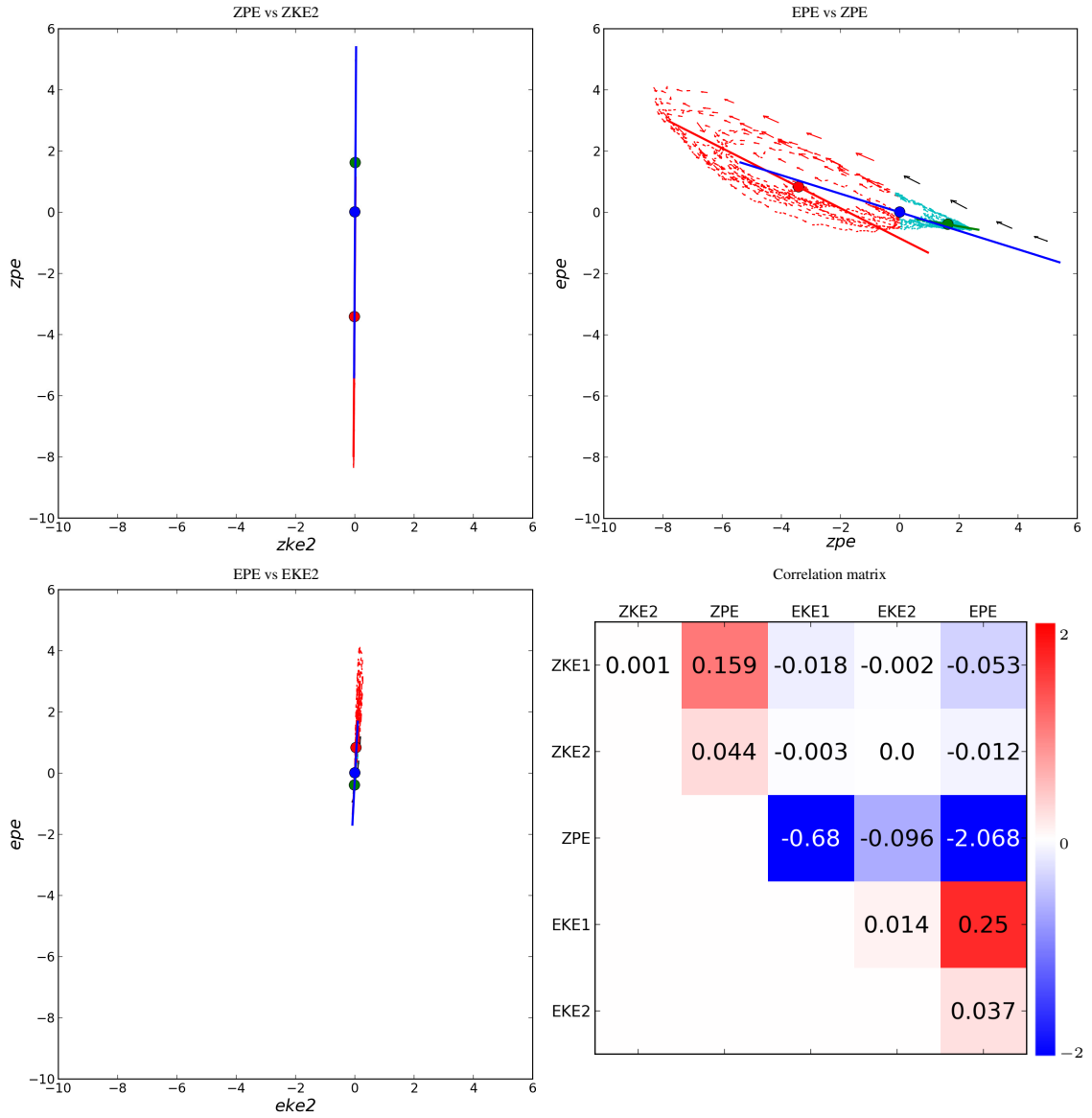

Figure 2.10: (a, b, c) Scatterplots of different energy components, (a) for ZPE vs ZKE2, (b) for EPE vs ZPE, (c) for EPE vs EKE2, in the characteristic simulation as in Table 1 but using fixed, identical scales in each plot to emphasise which energy components exhibit the greatest variations. (d) The global correlation matrix is shown, computed using only the numerator of (2.14) for the different energy components.

present even during quiescent phases continue to provide inhomogeneous PV mixing, maintaining sharp jets [Dritschel and McIntyre, 2008, Scott and Dritschel, 2012]. These jets project on both barotropic and baroclinic modes, unlike the initial vertical shear flow.

2.5 Focus on a turbulent phase

The detailed behaviour of the flow around a turbulent phase is examined in this section. The panels in figure 2.11 show the time evolution of various diagnostics over $1800 \leq t \leq 2800$. The first three panels show energy components linearly rescaled to lie between 0 and 1 over the entire simulation duration ($0 \leq t \leq 10000$). In the third panel, the complement of the rescaled zonal energies is shown so that they can be better compared with the rescaled eddy energies (this panel combines the first two). The fourth panel shows the maximum growth rate for each zonal wavenumber k_x (in the abscissa), and the bottom panel shows the meridionally-integrated APE spectrum, also versus k_x.

In the top panel, the rescaled zonal energies ZKE2 and ZPE follow the same trend, especially on the approach to the turbulent phase. This is why the standard correlation between ZKE2 and ZPE is very high. However, ZKE1 decreases before the two other energies *and* recovers sooner. Similarly, in the second panel for the rescaled eddy energies, there is a small offset between the different components. EKE1 and EKE2 grow first (with EKE2 slightly ahead) and next EPE follows, with almost the same trend. This offset between the different energy components explains the looping or racquet patterns observed in the standard correlation scatterplots in Table 1.

The third panel compares the rescaled zonal and eddy energies. This highlights the differences in evolution of the various components. The eddy energies are seen to rise and fall rapidly, over a timescale comparable but shorter than the relaxation period $r^{-1} = 100$. The mode 1 zonal kinetic energy ZKE1 appears to lead all components into the turbulent phase, but due to the re-scaling, the energy changes involved are actually smaller than those taking place in ZPE and EPE (cf. figure 2.8). The onset of the turbulent phase is best associated with the steep rise in all the curves just before $t = 2100$, with the dominant energy transfer between ZPE and EPE. Other rising events happen later, e.g. between $t = 2300$ and 2400, without leading to any major disruption of the flow.

It therefore appears that the disturbance must reach a threshold amplitude before trig-

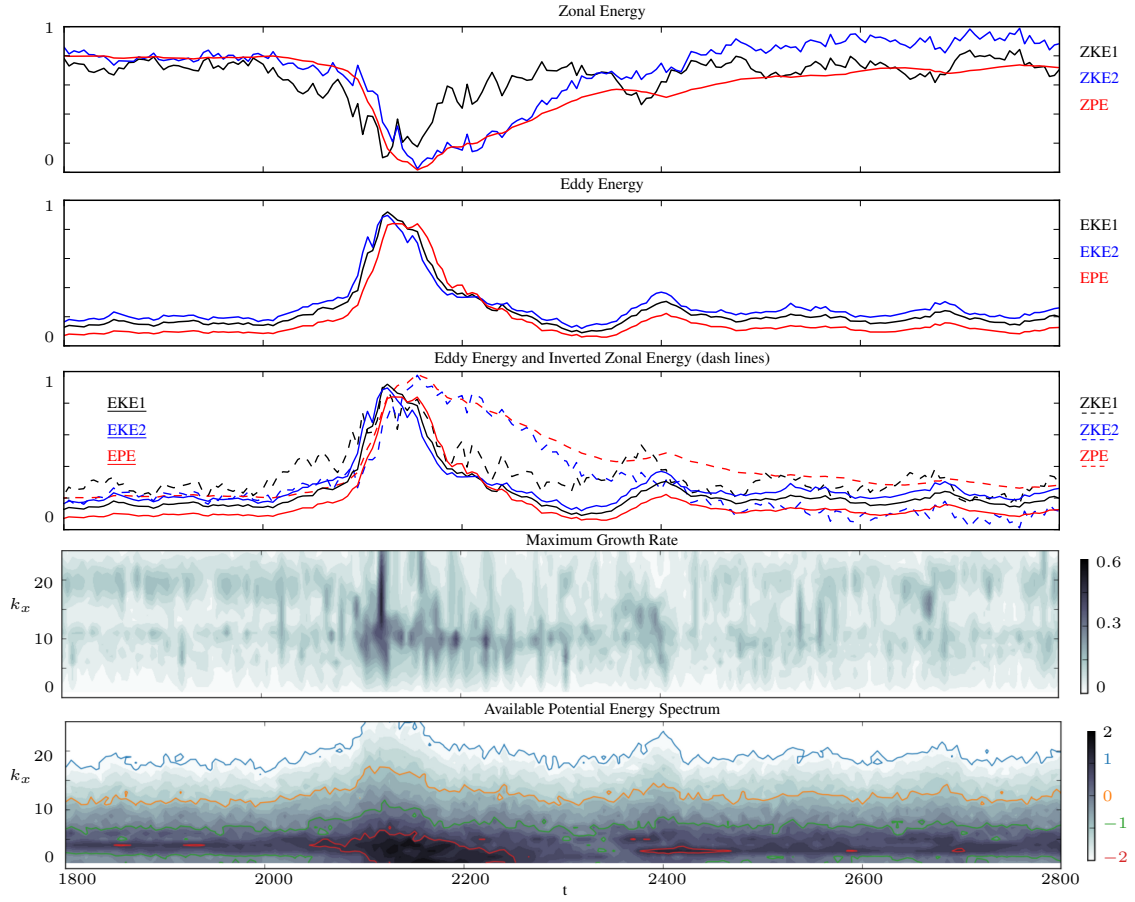

Figure 2.11: (a,b,c) Rescaled energy components (with mode 1 kinetic energy in black, mode 2 kinetic energy in blue and available potential energy in red) versus time for $1800 \leq t \leq 2800$. In (a) only zonal components are shown, in (b) only eddy components are shown, while in (c) all components are shown with the zonal ones inverted for comparison. (d) $\log_{10}$ of the maximum growth rate of the zonally-averaged flow versus zonal wavenumber k_x. (e) $\log_{10}$ of the meridionally-integrated spectrum of the available potential energy versus k_x. The coloured countours correspond to specific values of the spectrum as indicated on the colourbar. In each panel, time is in the abscissa.

gering a turbulent phase (this has been confirmed by examining many such events). In the PV field (not shown, but see the movie available to the online supplementary material), wave amplitudes along the jets are seen to slowly grow, eventually (sometimes after several false starts) leading to wave breaking and vortex formation. This strongly disturbed state lasts only a relatively short time before the vortices are either torn apart by the jet shear or recaptured by the jets, and the wave amplitudes gradually subside. The slow return to a quiescent state is most apparent in the behaviour of ZPE and ZKE2: the thermal relaxation slowly acts to rebuild the sloping layer interfaces, at the same time enhancing the baroclinic shear (in ZKE2). In this return to a quiescent phase, the principal energy changes (i.e. in ZPE) are mainly brought about by thermal relaxation. However, the rapid decay in all eddy energies, occurring over a period of just 20 to 30 units of time, cannot be explained simply by thermal relaxation. Instead, part of this decay must be due to inhomogeneous turbulent mixing, constrained by the mean PV gradient in each layer. The mixing acts to homogenise PV and sharpen jets, processes which are only enhanced by non-zonal variations [Dritschel and McIntyre, 2008, Scott and Dritschel, 2012]. The mixing continues until most of the eddy energy (principally at higher wavenumbers where thermal relaxation is weak) is exhausted and converted into jets (qualitatively this is the argument behind the Rhines scale $L_{\mathsf{Rh}} = \sqrt{U/\beta}$, where U characterises the eddy velocities and β is the background PV gradient, see Rhines [1975]). The low wavenumber part of the eddy energy gives rise to meanders, which unlike the high wavenumber part are affected by the thermal relaxation. Subsequently, thermal relaxation weakens the meanders and establishes quasi-zonal jets around $t = 2200$. Thereafter, thermal relaxation gradually modifies them, slowly bringing them closer together at the centre of the channel, as seen in the top two panels of figure 2.8. Eventually, this sets up the conditions for a further turbulent phase.

The maximum growth rate of the flow (shown in the fourth panel of 2.11) increases in the expected range of baroclinic instability wavenumbers, i.e. wavenumbers around $k_x = 11$, at the onset of the turbulent phase. Thereafter, at the peak of the turbulent phase around $t = 2150$, a wide range of wavenumbers are excited. Notably, just before this peak there is a decrease in the growth rate for high wavenumbers (18 to 20), that will only recover during the next quiescent phase. While it is not very clear in this figure, this feature is common to all the turbulent phases.

The APE spectrum (bottom panel) before the turbulent phase shows significant and persistent excitation of wavenumbers 4 to 6. During the first part of the turbulent phase,

there is an increase in power for small wavenumbers, from 2 to 4, and more generally for all wavenumbers. This is the effect of wave breaking, vortex generation and subsequent turbulent mixing. The increased excitation of all wavenumbers is matched by the growth of EPE shown in the second panel. Likewise, as the excitation subsides, so does the EPE, reaching a minimum around the end of the turbulent phase at $t = 2350$.

From this analysis, we can better understand the energy variations occurring during the onset and decay of a turbulent phase. The loop patterns exhibited in the correlation scatterplots (cf. figure 2.9) are associated with the asynchronous growth and decay of the various energy components. What we find generically, across many events and simulations examined, is that at the onset of a turbulent phase ZKE1 decreases marginally sooner than both ZKE2 and ZPE, which remain highly correlated until near the end of the turbulent phase. ZKE1 recovers much sooner than either ZKE2 or ZPE, and this appears to be an eddy effect. Looking back at figure 2.8, we can see that the dips in ZKE1 occurring during a turbulent phase only last while there is significant eddy energy. By contrast, ZKE2 and ZPE take longer to recover, well after the eddy energies have all but dissipated. Another generic feature worth noting is that, at the onset of a turbulent phase, EKE2 appears to increase slightly before EKE1, which is then followed by EPE. The recovery is also in the same order, with EPE recovering last. The recovery is also rapid, mainly a nonlinear effect of inhomogeneous mixing. Thermal relaxation acts most strongly at largest scales, and gradually weakens the low-wavenumber meanders on the jets. This helps to re-establish strong quasi-zonal jets, which then slowly shift due to thermal relaxation until conditions are established for the next turbulent phase.

2.6 Dependence on parameters

2.6.1 Parameter Sweep

To study the dependence of the flow evolution on the different parameters involved, a wide range of simulations have been conducted. The main parameters consist of the thermal relaxation coefficient r, the lower layer fractional PV gradient ϵ_1 (directly controlling the vertical shear), the stratification coefficient c_ρ, the enstrophy input rate η, and the heton PV q_{heton}. Other parameters have been varied, like the heton radius R and topographic forcing, but these have been found to have only a minor influence. Table 2.2 lists the

N_x	c_ρ	ϵ_1	η	$q_1 \times \overline{k}_d/\beta$	r	other
512	2	-0.5	0.1	1	0, 10^{-4}, 10^{-3} 10^{-2}, 0.1, 0.5	
512	2	-0.1	0.1	1	0, 10^{-3}, 10^{-2} 0.1, 0.5	
512	0.2	-0.1	0.1	1	0, 10^{-3}, 10^{-2} 0.1, 0.5	
512	0.2	-0.1	0.01, 1	1	0.01	
512	2	-0.1	0.01, 1	1	0.01	
256	0, 2	-0.5	10, 100	10, 30, 100, 300	0.01	
256	2	-0.1	100	100, 300, 1200		Heton radius
256	2	-0.1	100	300	0.001	$R = 0.025$ rather
256	0	-0.1	100	100	0.01	than 0.05
256	0	-0.5	100	100	0.01	$h_1 = 0.9$
256	0	-0.5	100	100	0.01	$h_1 = 0.95$
256	5	-0.5	100	100	0.01	
256	2	2.0	1	1	0.001	opposite
256	0	1.5	1	1	0.001	vertical shear
256	2	$-0.5, -0.4, -0.3$ $-0.2, -0.1$	0.1	1	0.01	
128, 512	2	-0.5	0.1	1	0.01	
256	0	1	100	100	0.01	with and without topography

Table 2.2: Numerical and physical parameters for the set of experiments conducted in this study.

parameters used for the main simulations conducted in this study. In the following subsections, we focus on the parameters having the greatest influence: the thermal relaxation r and the vertical shear parameter ϵ_1. We then briefly summarise the influence of the remaining parameters.

2.6.2 Thermal relaxation

An important parameter controlling the flow evolution is thermal relaxation. A wide range of thermal relaxation rates $r = \{0, 0.0001, 0.001, 0.01, 0.1, 0.5\}$ have been examined,

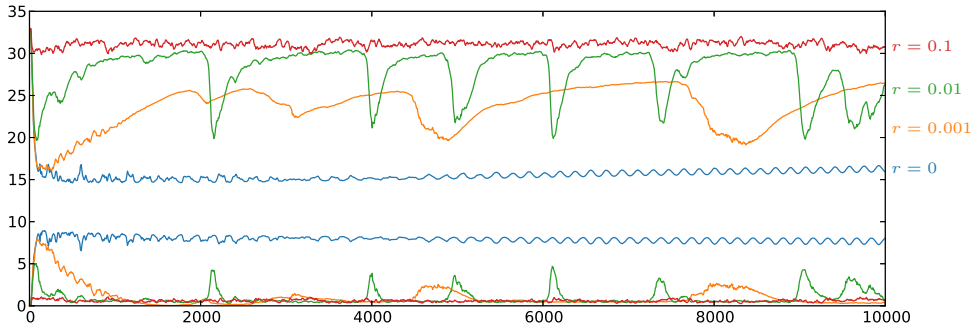

Figure 2.12: The evolution of zonal (upper plots) and eddy (lower plots) potential energy (ZPE and EPE) for different thermal relaxation rates r: no relaxation, blue; 0.001, orange; 0.01 (reference), green; and 0.1, red.

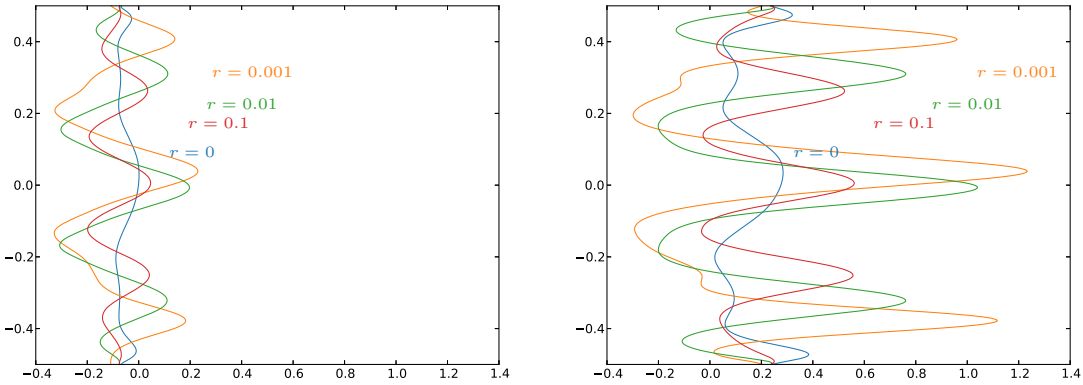

Figure 2.13: Lower layer (left panel) and upper layer (right panel) time-averaged between $t = 6500$ and $t = 7300$ (quiescent phase) zonally-averaged zonal velocity $\bar{u}_i(y,t)$, for different thermal relaxation rates r: no relaxation, blue; 0.001, orange; 0.01 (reference), green; and 0.1, red.

mainly for different values of stratification coefficient c_ρ and vertical shear parameter ϵ_1. Thermal relaxation acts to restore the initial vertical shear. Simultaneously, baroclinic instability, induced by excessive vertical shear, leads to turbulent mixing which tends to reduce the vertical shear. There is thus a competition between thermal relaxation and baroclinic instability which nearly always results in the formation of jets through inhomogeneous PV mixing.

Thermal relaxation is found to have a major impact on the evolution of the flow. This is exhibited in figure 2.12 comparing the evolution of zonal potential energy (ZPE) for $r = 0, 0.001, 0.01$ and 0.1, keeping all other parameters at their default values. The green curve corresponds to the characteristic simulation examined already. At high relaxation rates, $r \geq 0.1$, the flow appears to be very stable: the initial ZPE is reduced by only 12% for $r = 0.1$ and fluctuates close to a constant value thereafter. In fact, small-scale disturbances are ever present due to the perpetual creation of baroclinic instability, but

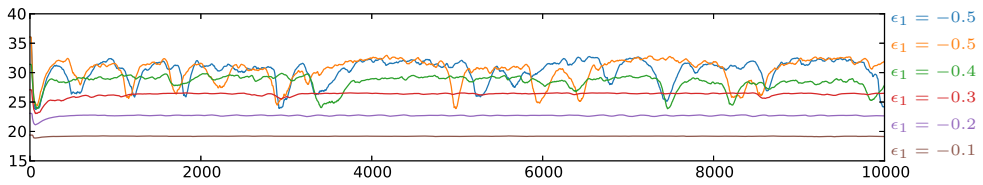

Figure 2.14: Zonal potential available energy's evolution for five different vertical shears ϵ_1: -0.1 brown; -0.2 purple; -0.3 red; -0.4 green; and -0.5 orange and blue.

no large-scale disruption like that seen in figure 2.5 for the characteristic simulation ever occurs. At high relaxation, the flow exhibits many weak jets whose number remains constant from the earliest times. By contrast, with no relaxation ($r = 0$), the imposed vertical shear is rapidly cancelled, suppressing any further baroclinic instability. The flow in this case is mainly dominated by large-scale oscillations with a few weak jets, see figure 2.13. For small but non-zero relaxation ($r = 0.001$ and 0.01), there is a competition between the relaxation trying to restore the vertical shear and baroclinic instability trying to break it down, leading to strong, widely-spaced jets. The relaxation has a direct impact on the intensity of the jets (their zonal velocity) and jet spacing, as seen in figure 2.13. As in the characteristic case presented in §2.3.1, the flow is more unstable and variable, and exhibits large-scale fluctuations. The relaxation rate strongly affects the recovery time from each turbulent phase, leading to a wider spacing of turbulent events.

2.6.3 Vertical shear

The initial vertical shear is directly controlled by the lower layer relative PV gradient, ϵ_1 (see appendix §A). When $\epsilon_1 < 0$, PV gradients are reversed in the two layers, and the vertical shear is sufficient to induce baroclinic instability. The more negative ϵ_1 is, the greater is the vertical shear and thus the potential for instability.

Vertical shear has a direct influence on the number of homogeneous regions and jets that develop, see figure 2.14. Increased vertical shear implies stronger baroclinic instability and thus higher eddy velocities, u'_{rms}. This on its own would imply an increased jet spacing, qualitatively, through the Rhines scale $L_{\mathsf{Rh}} = \sqrt{u'_{rms}/\,|\bar{q}_y|}$, except that the mean PV gradient $|\bar{q}_y|$ also increases. Nevertheless, we find that higher vertical shear leads to both a wider jet spacing and more intense jets, see figure 2.15. Regarding the oscillations between quiescent and turbulent phases, higher vertical shear decreases their frequency. When the vertical shear is too weak to permit baroclinic instability ($\epsilon_1 \geq 0$), the flow

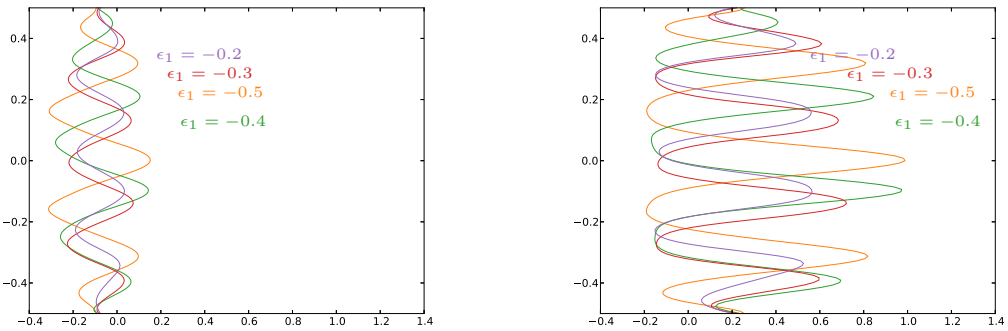

Figure 2.15: Lower layer (left figure) and upper layer (right figure) zonally-averaged zonal velocity $\bar{u}_i(y,t)$ averaged between $t = 3800$ and $t = 4500$ (quiescent phase), for different vertical shears ϵ_1: -0.2 purple; -0.3 red; -0.4 green; and -0.5 orange.

evolution is radically different than what we have seen so far. Jets, if at all present, are very weak and erratic.

2.6.4 Other parameters

Many other simulations have been conducted, looking at the effect of stratification, the PV of the injected hetons, the enstrophy input rate, etc. Regarding stratification, the simulations presented in this paper are relevant to an atmospheric-like situation. We have also run simulations for oceanic-like cases ($c_\rho \to 0$). The main difference is a greater propensity for meandering at small scales, such as seen in oceanic currents like the Kuroshio or the Gulf Stream. Large scale structures are still present, though they are weaker and significantly disturbed by small scale perturbations. Jets are also less prominent. As in the oceans, the flow is less structured into zonal bands but contains many more coherent vortices. These findings are broadly consistent with those found by Maximenko et al. [2005], Kamenkovich et al. [2009], Berloff et al. [2011] who examined a forced idealised two-layer ocean with Ekman damping.

Regarding the heton PV and the enstrophy input rate, we have examined the effect of adding a few high intensity hetons versus adding numerous low intensity hetons. We thought that adding high intensity hetons would favour the formation of long-lived vortices, but this is not true. Inevitably any intense vortices which do form drift north or south and get torn apart by or incorporated into the intense jets. Overall, these parameters have only a small impact on the flow evolution. Simulations with different parameters exhibit

the same number of homogeneous regions and jets, with comparable jet velocities and spacing. Further details concerning the impact of hetons are provided in section §3.4.2. Essentially, hetons tend to damp the flow and homogenise the energy (in particular ZPE) over time during quiescent phases. Without hetons, variable topography is necessary to obtain similar ratios between the energy fluctuations during quiescent phases, and the drop of energy during turbulent events.

2.7 Conclusions

We have investigated the emergence, nonlinear dynamics and energetics of jets and vortices in a two-layer β-plane quasi-geostrophic channel model. An extensive range of numerical simulations have been carried out using the Combined Lagrangian Advection Model [Dritschel and Fontane, 2010], at unprecedented resolution and for very long times (10^4 to 10^5 model days). We have primarily focused on the atmospheric case where there is a strong density difference between the two layers and where thermal relaxation acts to maintain vertical shear against baroclinic instability. As found in the original study of this type by Panetta and Held [1988], the competition between relaxation and baroclinic instability results in quasi-zonal jets. In the present study, additionally, we have included the effect of stochastic forcing, specifically adding small-scale baroclinic vortices called 'hetons' randomly at a prescribed enstrophy input rate. These hetons are meant to crudely model the effects of convection thought to occur in the atmospheres of the gas giant planets (see Thomson and McIntyre [2016] and references therein). The details of the stochastic forcing however do not seem to matter: qualitatively similar evolution is observed without such forcing when the initial flow is weakly perturbed.

The combination of thermal relaxation, heton forcing and atmospheric stratification leads to a 'baroclinic life cycle' (see [Feldstein and Held, 1989, Thorncroft et al., 1993, Esler, 2008]), in which jets emerge through baroclinic instability of the vertically-sheared flow and subsequently break down and reform, often in an irregular manner. The jets form through inhomogeneous potential vorticity mixing [Dritschel and McIntyre, 2008, Scott and Dritschel, 2012], in which potential vorticity is nearly homogenised in bands, but between which the potential vorticity abruptly jumps, forming a 'staircase' profile. Each jump is associated with a jet, eastward in the upper layer and westward in the lower layer, a direct effect of potential vorticity inversion [Dritschel and McIntyre, 2008].

Both thermal relaxation and heton forcing continuously modify the jets that form through baroclinic instability. Thermal relaxation works to increase the vertical shear (favouring baroclinic instability), while heton forcing creates disturbances which eventually trigger the breakdown of the jets. In most cases, this breakdown is characterised by wave amplification and breaking on the quasi-zonal jets, leading to vortex detachment and turbulence. In this 'turbulent phase', the upper layer jets often persist but become strongly non-zonal and time dependent, while the lower layer jets are nearly obliterated before they reform. The turbulent phase lasts typically one thermal relaxation period, approximately, but only part of the recovery is due to thermal relaxation. From a detailed analysis of the energetics, it is found that the eddies (or non-zonal disturbances) created at the onset of a turbulent phase convert their energy into jets, arguably by inhomogeneous potential vorticity mixing (an inviscid mechanism). Thermal relaxation, by contrast, acts mainly at large scales to dampen long-wave disturbances and straighten the jets. Thereafter, thermal relaxation slowly shifts the jets and builds the mean vertical shear, setting up the conditions for subsequent instability and breakdown.

Each turbulent phase is followed by a 'quiescent' phase characterised by nearly zonal jets with weak small-scale disturbances. Notably, these oscillations between quiescent phases and turbulent events have not been seen before in previous studies, e.g. Panetta and Held [1988] and Thompson and Young [2007]. These quiescent phases often exhibit a gradual latitudinal migration of the jets. In one particular example studied in detail, two distinct quiescent phases were observed, one of which was significantly more robust (long lived) than the other (further analysis may be found in appendix B.) The quasi-zonal jets occurring during the quiescent phases are typically highly baroclinic. There are different numbers of jets in each layer located at different mean latitudes. Moreover, the upper layer jets are predominantly eastward, while the lower layer jets are predominantly westward, or a mix between the two due to the strong influence of the upper layer potential vorticity on both layers.

The wider dependence of the flow evolution on thermal relaxation, vertical shear, stratification, heton intensity and enstrophy input rate has also been studied. Increasing thermal relaxation weakens the turbulence created during baroclinic instability, leading to less temporal variation especially of the zonal energy components. While baroclinic instability still occurs (for sufficient vertical shear), it only manages to create weak jets for strong thermal relaxation (i.e. for a 10 day or shorter relaxation period). On the other hand, no relaxation results in the destruction of the initial vertical shear and no further

chance for baroclinic instability. Weaker relaxation leads to baroclinic life cycles, here oscillations between turbulent and quiescent phases. Both phases extend in proportion to the relaxation period, though the recovery of the zonal part is significantly slower than the recovery of the eddy part.

Increasing vertical shear makes the flow more unstable, generally creating fewer, more intense jets. Changing the stratification to a form more appropriate to the oceans, we find that the jets exhibit significant meandering and are less well defined. Moreover, many more vortices are present which last for much longer times than found for atmospheric stratification. These results are consistent with the two-layer ocean study of Maximenko et al. [2005], Kamenkovich et al. [2009], Berloff et al. [2011]. The remaining model parameters (heton intensity, enstrophy input rate) have been found to have only a weak impact on the flow evolution.

A conspicuous feature of the atmospheric-like simulations we have conducted is the absence of long-lived vortices, despite an extensive exploration of parameter space. Vortices do form but they inevitably collide with a jet and are either incorporated or destroyed. A major question then is: is there a parameter regime within this two-layer quasi-geostrophic model favouring long-lived vortices? Or, is it necessary to go beyond the quasi-geostrophic model and consider ageostrophic effects (e.g. as in a shallow-water context)? Or again, is spherical geometry fundamental? Does the Great Red Spot, for instance, depend on its proximity to the equatorial region, whose dynamics can be starkly different from quasi-geostrophic? Are two-layers sufficient? We are presently working to answer some of these questions by building and applying a highly-accurate multi-layer shallow water numerical model.

Chapter 3

Two-layer quasi-geostrophic flow over topography

3.1 Introduction

The impact of topography on geophysical flows has been widely examined using different experimental approaches, numerical models, and theoretical analyses. For example, Hart [1975] conducted an experimental and analytical study investigating how bottom topography affects the stability of a circular vortex. He found that perturbations from the mean flow have a broader spectrum when using a linear topography rather than a flat bottom.

Previously, numerical studies such as Orlanski [1969] looked at the impact of bottom topography on a baroclinic flow. Orlanski applied his model to different topography profiles characteristic of the Gulf Stream region and showed that topography is an essential factor in the stability analysis for representing the behaviour of the Gulf Stream. Subsequently, various studies have been conducted to look at the impact of topography on oceanic flows, for example on the Antarctic Circumpolar Current (see Treguier and Hua [1988], Tréguier and McWilliams [1990], Wolff et al. [1991], Jackson et al. [2006] and Thompson and Sallée [2012]), on the Gulf Stream (see Tansley and Marshall [2000], Schmeits and Dijkstra [2001] and Chassignet and Marshall [2008]), and on the Agulhas current (see Darbyshire [1972] and Matano [1996]). In each case, topography was found to be an essential factor in the behaviour of these flows.

More theoretically, Pedlosky [1970] studied the behaviour and stability of baroclinic

waves using a two-layer quasi-geostrophic model. As a continuation of this work, Steinsaltz [1987] used a similar approach adding a sloping meridional topography and found that for a small vertical shear, large wavenumbers can be unstable, in contrast to what was found in Pedlosky's study. Additionally, large wavenumber perturbations have a greater amplitude in the lower layer than in the upper layer. To study the formation and evolution of waves and jets in a two-layer model, LaCasce and Brink [2000] used decaying turbulence while Thompson [2010] and Boland et al. [2012] used a forced-dissipative model. With a linear meridional sloping topography on the f-plane, LaCasce and Brink [2000] obtained an intensification of the flow in the bottom layer and surface vortices in the upper layer. Using a forced-dissipative model on the β-plane, with a meridional sloping topography, Thompson [2010] studied the dependence of jet spacing and jet variability. He found that jet spacing is characterised by the barotropic Rhines scale, defined by $L_{Rhbt} = 2\pi\sqrt{V_e/\beta_{bt}}$, with V_e the eddy velocity and β_{bt} the barotropic potential vorticity gradient. As a continuation of this work, Boland et al. [2012] added a zonal sloping topography to this meridional sloping topography, and used a doubly periodic barotropic and a two-layer baroclinic quasi-geostrophic model. They found that tilted jets drift latitudinally in time. They explained this drift by the difference of orientation between the PV gradient in each layer and the barotropic PV gradient. In a related study, Chen and Kamenkovich [2013] investigated the impact of topography on baroclinic instabilities using a QG eddy-resolving model. They found that a zonal sloping topography has a strong effect on the destabilisation of the flow. Conversely, a meridional sloping topography can either stabilise or destabilise the flow by either equalising or opposing the PV gradient sign of the two layers, respectively.

There is a wide variety of studies on the impact of topography in an oceanic context. This includes Venaille [2012], who showed that a topographic anomaly, such as a topographic bump, can create bottom-trapped currents. Poulin and Flierl [2005] and Poulin et al. [2014] further studied the influence of topography on the stability of jets using a two-layer QG model in an oceanic context with a linear slope. Growth rate and wavelength were found to vary with the topographic parameter, chosen as the ratio between the topographic slope and the isopycnal slope. Stern et al. [2015] investigated the evolution of a zonal jet around a continental shelf and over a very idealised topography. They studied the formation of jets over the continental shelf and then their migration off the shelf.

While most of these studies concentrate on oceanic flows, Thomson and McIntyre

[2016] focus on the co-existence of Jovian jets and vortices. They use a $1\frac{1}{2}$ layer QG model. To reproduce the Jovian jets, they impose a sinusoidal bottom interface. This feature imposes the positions of the jets. By injecting cyclone/anticyclone pairs (known as 'hetons'), they crudely mimic the convective motions thought to occur below the weather layer, as well as the co-existence of jets with long-lived vortices in the Jovian weather layer.

This chapter will focus on a very idealised topography consisting of a linear meridional sloping bottom. Previously, chapter 2 focused on the energetics of a two-layer QG β-channel shallow water model with an imposed vertical shear maintained by thermal relaxation and the injection of cyclone/anticyclone pairs. These pairs were randomly injected in space to mimic convective motions. We investigated the dependence of the flow on different parameters, such as thermal relaxation and vertical shear. Focusing on a characteristic simulation, we described the energy transfers occurring during two different phases of the flow; a quiescent phase and a turbulent phase. In this chapter, keeping the same parameters as in the characteristic simulation, we study the dependence of the flow evolution on a linear meridional topography.

First, the model is presented in section §3.2. Second, a stability analysis is conducted in section §3.3. Third, section §3.4 describes the main results, from their analysis to their interpretation. Section §3.5, finally, presents conclusions and perspectives.

3.2 Model formulation

To study the impact of topography on the emergence and evolution of jets and vortices in turbulent planetary atmospheres, we use the same model as in chapter 2 and add a linear meridional topography. The main aspects of the model will be briefly presented again (for more details see chapter 2). The model is based on the classic Phillips model (see Phillips [1951]), a two-layer shallow water quasi-geostrophic model in a channel on the β-plane, with bottom topography and a free surface at the top of each layer. The flow is governed by the equations:

$$\frac{Dq_1}{Dt} = F_1 \quad ; \qquad \frac{Dq_2}{Dt} = F_2 \tag{3.1}$$

$$q_1 = \beta y + \nabla^2\psi_1 - \frac{f_0(\delta_1 - \delta_b)}{H_1} \quad ; \qquad q_2 = \beta y + \nabla^2\psi_2 - \frac{f_0(\delta_2 - \delta_1)}{H_2} \tag{3.2}$$

$$\delta_1 = \frac{f_0(\psi_1 - \alpha\psi_2)}{g(1-\alpha)} \quad ; \qquad \delta_2 = \frac{f_0\psi_2}{g} \tag{3.3}$$

with D/Dt the material derivative, the subscript i referring to the layer $i = 1, 2$, q_i the quasi-geostrophic potential vorticity (QGPV), F_i representing the forcing and relaxation applied to the QGPV, β the linear gradient of the Coriolis frequency $f = f_0 + \beta y$, ψ_i the streamfunction, δ_i the displacement of the upper interface in layer i, δ_b the topography height, H_i the mean depth, ρ_i the uniform density, $\alpha = \rho_2/\rho_1$ the density ratio, and g the acceleration due to gravity. Layer 2 is above layer 1.

From the expression of the shallow-water Rossby-Ertel PV, we can obtain the QGPV using a series expansion. If we relate the pressure perturbations to the interface displacements using hydrostatic balance (see Mohebalhojeh and Dritschel [2004]) and to the streamfunction using geostrophic balance, we can write the QGPV (see Vallis [2006] for more details) as

$$q_1 = \beta y + \nabla^2\psi_1 + h_2\bar{k}_d^2(\alpha\psi_2 - \psi_1) - \beta_b y \tag{3.4}$$

$$q_2 = \beta y + \nabla^2\psi_2 + h_1\bar{k}_d^2(\alpha\psi_1 - \psi_2) \tag{3.5}$$

where $\beta_b y = -f_0\delta_b/H_1$ for the linear profile of topography considered, and

$$\bar{k}_d^2 = \frac{f_0^2 H}{g(1-\alpha)H_1H_2}$$

where $H = H_1 + H_2$ is the total mean depth.

As in chapter 2, we use a channel model, periodic in x and with free-slip rigid boundary conditions in y, where the zonally-averaged zonal velocity value imposed by the vertical shear is held fixed.

3.2.1 Topography

To study the impact of topography, we choose the simplest topography possible, a linear meridional slope, characterised by a single topography parameter $\tilde{\beta}_b = \beta_b/\beta$. A different topography, such as a parabolic or sinusoidal profile, would have required more parameters to characterise, thus complicating the analysis. Moreover, a constant-slope topography does not tie the location of the jets to features in the topography, enabling us to study how the topographic slope alone influences jet spacing and intensity.

3.2.2 Stratification

Two different basic-state density profiles have been adopted in this study. We first conducted ocean-like simulations using the Boussinesq approximation, with equal layer depths and a density ratio $\alpha = \rho_2/\rho_1 \approx 1$, i.e. $\alpha - 1 \ll 1$, see Vallis [2006], p67. Next, we conducted atmosphere-like simulations using an exponentially decreasing density profile approximated by two equal thickness layers, which gives a density ratio of $\alpha = \rho_2/\rho_1 = \mathrm{e}^{-c_\rho/2}$, with c_ρ the model depth as a multiple of the scale height H_ρ, defined by $c_\rho H_\rho = H_1 + H_2 = H$. (Note that in the Boussinesq case, we have $c_\rho = 0$.)

3.2.3 Forcing and relaxation

In chapter 2, stochastic forcing was applied to crudely model unresolved convective motions using hetons. This forcing however appears to have little impact on the flow evolution, apart from providing a greater level of background perturbations which make it more difficult for the thermal relaxation to restore the basic state (see section §3.4.2 below). In this study, we therefore remove this forcing. Instead, we add a small Rossby wave perturbation in the lower layer at the initial time to create a non-zonal disturbance, thus allowing the flow to destabilise without perturbing the flow subsequently.

As in chapter 2, a vertical shear is imposed to model the latitudinal thermal forcing variation between the equator and the poles. In the quasi-geostrophic approximation, thermal wind balance relates the latitudinal temperature gradient to a uniform velocity in each layer (in opposite directions). The quasi-geostrophic potential vorticity (QGPV) is linearly related to the streamfunction. In turn, the streamfunction is linearly related to the velocity. Thus, the vertical shear is imposed as an additional QGPV term varying linearly with the streamfunction. The total background PV is written as $\epsilon_i \beta y$ with ϵ_i the parameter controlling the vertical shear in layer i. See chapter 2 for the relation between ϵ_i and the shear.

3.2.4 Parameter choices

Most parameters have the same values as in the characteristic simulation in chapter 2. The domain is defined by the widths $L_x = 2\pi$ and $L_y = \pi$, the Rossby deformation length is

equal to $L_d = 1/\bar{k}_d$, and the fractional layer depth $h_1 = H_1/H = h_2 = H_2/H = 1/2$. The density ratio is $\alpha = \rho_2/\rho_1 = \mathrm{e}^{-c_\rho/2} \simeq 0.37$, with $c_\rho = 2$. We obtain $k_{d1} \simeq 8.87$ and $k_{d2} \simeq 17.93$ as the deformation wavenumbers of the two vertical modes. The planetary vorticity gradient is equal to $\beta = 8\pi$. The vertical shear is controlled by the parameters ϵ_i, so that the total PV gradient is equal to $\epsilon_i\beta$ in layer i. We consider $\epsilon_1 = -0.5$ and $\epsilon_2 = 3.79$. The thermal relaxation rate is fixed at $r = 0.01$. The initial Rossby wave, present in the lower layer to create a small perturbation of the flow, has a PV perturbation equal to $B\sin(kx)\sin(ly)$, with $B = 2$, $k = 5$ and $l = 2$. The topographic parameter $\tilde{\beta}_b$ varies between -0.5 and 0.25. We chose this range of topography as it captures all the regimes of interest, from the margin of stability to highly dynamic simulations where the flow oscillates between quiescent and turbulent phases.

Simulations were run on a grid of the following dimensions: $N_x \times N_y$ with $N_x = 256$ and $N_y = 129$ over 10^4 units of time, using the 'Combined Lagrangian Advection Method' (see Dritschel and Fontane [2010] for more details).

3.3 Linear Stability Analysis

We next perform a linear stability analysis for a Boussinesq two-layer problem on the β-plane with bottom topography but no forcing or relaxation on the QGPV. The set of equations governing the dynamics is the same as for equations 3.1 without forcing or relaxation.

We start with an initial state defined by a zonally averaged QGPV $\bar{q}_i$ and velocity in each layer $\bar{u}_i$, with β the linear component of the Coriolis frequency $f = f_0 + \beta y$, β_b the gradient of the topographic PV, i.e. $f_0\delta_b/H = -\beta_b y$. For equal layer depths, we have $-\bar{u}_1 = \bar{u}_2 = u_c/2 = \bar{u}$ with u_c the baroclinic or shear velocity. The basic-state PV is

$$\begin{aligned} \bar{q}_1 &= (-\bar{k}_d^2\bar{u}^2 + \beta - \beta_b)y = (\epsilon - \tilde{\beta}_b)\beta y \\ \bar{q}_2 &= (\bar{k}_d^2\bar{u}^2 + \beta)y = \lambda\beta y. \end{aligned} \tag{3.6}$$

Considering small perturbations to the QGPV q_i' and streamfunctions ψ_i' of the form

$$\begin{aligned} q_i'(x,y,t) &= \Re\{Q_i(y)e^{\mathrm{i}(k_x x - \sigma t)}\} \\ \psi_i'(x,y,t) &= \Re\{\Psi_i(y)e^{\mathrm{i}(k_x x - \sigma t)}\} \end{aligned} \tag{3.7}$$

with k_x the prescribed zonal wavenumber, σ the frequency, and $Q_i(y)$ and $\Psi_i(y)$ the amplitude of perturbations, the linearised PV conservation equations reduce to

$$(\bar{u}_i - c)Q_i + \frac{d\bar{q}_i}{dy}\Psi_i = 0, \quad i = 1, 2 \tag{3.8}$$

with $c = \sigma/k_x$ the phase speed.

Next, we use the inversion relation relating $\hat{q}_j$ to $\hat{\psi}_j$, with $j = 1, 2$ the vertical modes:

$$\begin{aligned} \hat{q}_1 &= \nabla^2\hat{\psi}_1 = -k_x^2\hat{\psi}_1 \\ \hat{q}_2 &= \nabla^2\hat{\psi}_2 - \bar{k}_d^2\hat{\psi}_2 = -(k_x^2 + \bar{k}_d^2)\hat{\psi}_2. \end{aligned} \tag{3.9}$$

The vertical modes' QGPV and streamfunctions are related to the layers' QGPV and streamfunctions by the relations (written only for QGPV, but similar for the streamfunctions)

$$\begin{aligned} \hat{q}_1 &= (q_1 + q_2)/2 \quad ; \quad q_1 = \hat{q}_1 - \hat{q}_2/2 \\ \hat{q}_2 &= q_2 - q_1 \quad ; \quad q_2 = \hat{q}_1 + \hat{q}_2/2. \end{aligned} \tag{3.10}$$

By combining equations 3.8, 3.9 and 3.10 we obtain a quadratic equation in c:

$$\begin{aligned} c^2k_x^2(k_x^2 + \bar{k}_d^2) + c(\beta - \beta_b/2)(2k_x^2 + \bar{k}_d^2) + (\beta - \beta_b/2)^2 \\ -\bar{u}^2k_x^2(k_x^2 - \bar{k}_d^2) + \bar{u}\beta_b/2(2k_x^2 - \bar{k}_d^2) - \beta_b^2/4 = 0. \end{aligned} \tag{3.11}$$

Or, in terms of ϵ, $\tilde{\beta}_b$, $\tilde{c} = c\beta/\bar{k}_d^2$ and $\tilde{k}_x = k_x/\bar{k}_d$, we have

$$\begin{aligned} c^2\tilde{k}_x^2(\tilde{k}_x^2 + 1) + c(1 - \tilde{\beta}_b/2)(2\tilde{k}_x^2 + 1) + (1 - \tilde{\beta}_b/2)^2 \\ -(1-\epsilon)^2\tilde{k}_x^2(\tilde{k}_x^2 - 1) + (1-\epsilon)\tilde{\beta}_b/2(2\tilde{k}_x^2 - 1) - \tilde{\beta}_b^2/4 = 0. \end{aligned} \tag{3.12}$$

To find the maximum growth rate and the stable and unstable regions in the ϵ-$\tilde{\beta}_b$ parameter space, we find the dispersion relation:

$$\tilde{c} = \frac{(-(1 - \tilde{\beta}_b/2)(2s + 1) \pm \sqrt{R}}{2s(s + 1)} \tag{3.13}$$

where $s = \tilde{k}_x^2$ and

$$R(s) = 4s^4(1-\epsilon)^2 - 4\tilde{\beta}_b s^3(1-\epsilon) + 4s^2(\tilde{\beta}_b^2/4 - (1-\epsilon)\tilde{\beta}_b/2 - (1-\epsilon)^2) + 4s\tilde{\beta}_b/2(\tilde{\beta}_b/2 + (1-\epsilon)) + (1-\tilde{\beta}_b/2)^2. \tag{3.14}$$

Instabilities occur where $R < 0$, and the maximum growth rate over s can be determined from the roots of a high-order polynomial (not shown).

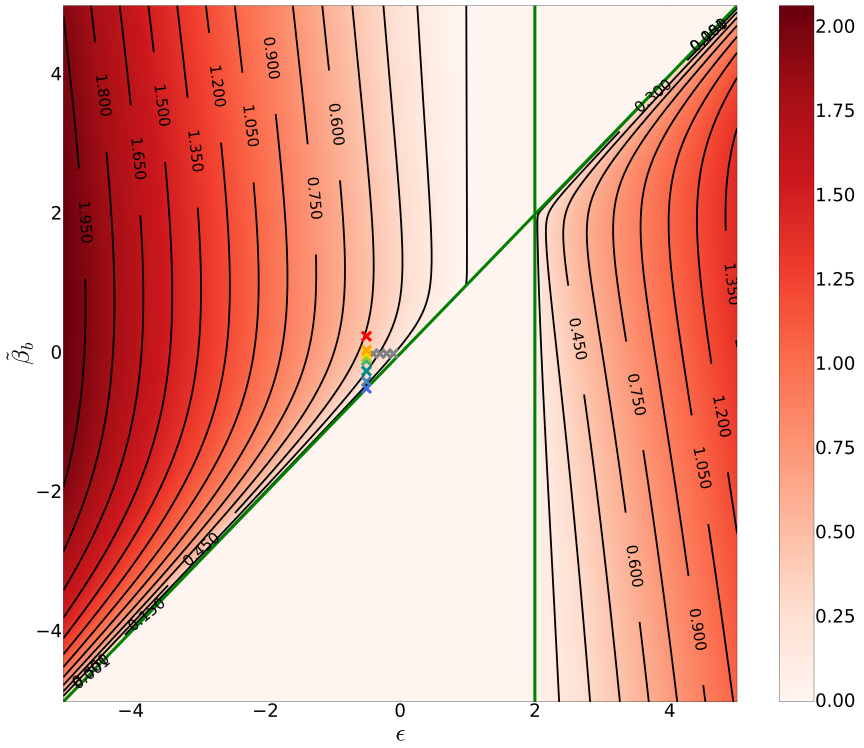

Figure 3.1: Dimensionless maximum growth rate $\tilde{\sigma}$ as a function of the vertical shear parameter ϵ and the topographic parameter $\tilde{\beta}_b$. Grey crosses mark the simulations conducted in chapter 2 while the coloured crosses mark the simulations conducted in the present chapter.

Figure 3.1 exhibits the dimensionless maximum growth rate $\tilde{\sigma} = \sigma\beta/\bar{k}_d^2$ for various $\tilde{\beta}_b$ and ϵ values. Baroclinic instabilities can occur when $\beta_1\beta_2 < 0$. The vertical green line corresponds to $\epsilon = 2$, and so $\lambda = 0$, therefore $\beta_2 = 0$ – the upper layer PV gradient vanishes. The slanting green line corresponds to $\tilde{\beta}_b = \epsilon$, and so the lower layer PV gradient $\beta_1 = \beta(\epsilon - \tilde{\beta}_b) = 0$. The upper left region, between the two green lines, corresponds to the unstable region where $\tilde{\beta}_1 < 0$ and $\tilde{\beta}_2 > 0$. The lower right region corresponds to the unstable region where $\tilde{\beta}_1 > 0$ and $\tilde{\beta}_2 < 0$. Finally, the two regions without contours are regions where the flow is stable. In chapter 2, no topography was

present. Simulations performed in that chapter are shown on the graph by grey crosses. Additional simulations performed with topography are shown on the graph by coloured crosses and described further below.

3.4 Results

We next discuss the results of a series of non-linear simulations investigating the influence of sloping bottom topography on jet formation and dynamics.

First, section §3.4.1 presents the energy decomposition into modal kinetic and available potential energies. Next, we focus on the dependence of the flow on the initial conditions and the stochastic forcing in section §3.4.2. Then, the dependence of the flow on the amplitude of topography is investigated in section §3.4.3. Finally, we present some conclusions and perspectives in section §3.5.

3.4.1 Energy decomposition

We next explain how to calculate the kinetic and available potential energies, whose sum gives the total conserved energy (in the absence of forcing and dissipation).

We start with the shallow-water equations:

$$\begin{aligned} \rho_1 \left(\frac{D\mathbf{u_1}}{Dt} + f\mathbf{k} \times \mathbf{u_1} \right) &= -\nabla p_1 \\ \rho_2 \left(\frac{D\mathbf{u_2}}{Dt} + f\mathbf{k} \times \mathbf{u_2} \right) &= -\nabla p_2 \end{aligned} \tag{3.15}$$

with D/Dt the material derivative, $\mathbf{u_i}$ the velocity in the layer i, and p_i the layer pressure.

The potential energy PE is found from

$$\begin{aligned} PE &= \rho_1 g \int_x \int_y \int_{z=\delta_b}^{h_1+\delta_b} z dz dy dx + \rho_2 g \int_x \int_y \int_{z=h_1+\delta_b}^{h_2+h_1+\delta_b} z dz dy dx \\ &= \frac{1}{2} g \rho_1 < (1-\alpha) h_1^2 + \alpha (h_1+h_2)^2 + 2\delta_b (h_1 + \alpha h_2) > \end{aligned} \tag{3.16}$$

with $< \ . \ >$ denoting an area average, h_i the mean layer thickness of layer i, δ_i the

displacement of the upper interface of each layer i and δ_b the topography height.

Similarly, the kinetic energy KE is found from

$$\begin{aligned} KE &= \frac{1}{2}\rho_1 \int_x \int_y \int_{z=\delta_b}^{h_1+\delta_b} \left(u_1^2 + v_1^2\right) dzdydx + \frac{1}{2}\rho_2 \int_x \int_y \int_{z=h_1+\delta_b}^{h_2+h_1+\delta_b} \left(u_2^2 + v_2^2\right) dzdydx \\ &= \frac{1}{2}\rho_1 < h_1(u_1^2 + v_1^2) + \alpha h_2(u_2^2 + v_2^2) > . \end{aligned} \tag{3.17}$$

with u_i and v_i the zonal and meridional velocities in layer i.

These relations can be simplified and generalised to an n-layer shallow water flow as

$$\begin{aligned} PE &= \frac{1}{2} g \sum_{i=1}^{n} \rho_i < z_i^2 - z_{i-1}^2 >= g \sum_{i=1}^{n} \rho_i < h_i \bar{z}_i > \\ KE &= \frac{1}{2} \sum_{i=1}^{n} \rho_i < h_i \left|\mathbf{u_i}^2\right| > \end{aligned} \tag{3.18}$$

with $z_i(x, y, t)$ the height of the layer i and $\bar{z}_i(x, y, t)$ the mean height of layer i.

In our two-layer context, we can write this relation in terms of the displacement δ_i of the upper interface of each layer i, using $h_1 = H_1 + \delta_1 - \delta_b$ each $h_2 = H_2 + \delta_2 - \delta_1$.

Typically, a large part of the potential energy is not available dynamically. This part is associated with the background undisturbed state, in which

$$z_i = \sum_{j=1}^{i} H_j.$$

The remaining potential energy is called the "available potential energy" (APE). The available potential energy is equal to

$$APE = \frac{1}{2} g\rho_1((1-\alpha) < \delta_1^2 > +\alpha < \delta_2^2 >). \tag{3.19}$$

Notably the topography does not contribute explicitly to the APE.

Under the QG approximation, the streamfunctions are related to the heights and dis-

placements by the relations:

$$\begin{aligned}\psi_1 &= \frac{g}{f}(h_1 + \alpha h_2 + \delta_b) = \frac{g}{f}((1-\alpha)\delta_1 + \delta_2) \\ \psi_2 &= \frac{g}{f}(h_1 + h_2 + \delta_b) = \frac{g}{f}\delta_2.\end{aligned} \tag{3.20}$$

So the APE can be written as

$$\begin{aligned}APE &= \frac{1}{2}\rho_1 \frac{f_0^2}{g(1-\alpha)} < (\psi_1 - \alpha\psi_2)^2 + \alpha(1-\alpha)\psi_2^2 > \\ &= \frac{1}{2}\rho_1(H_1 + H_2)h_1 h_2 \bar{k}_d^2(< (\psi_1 - \alpha\psi_2)^2 > + \alpha(1-\alpha) < \psi_2^2 >).\end{aligned} \tag{3.21}$$

Similarly, under the QG approximation, in the KE it is consistent to replace the θ_i by their mean values H_i. It is convenient to normalise APE and KE by $\rho_1(H_1 + H_2)$ to remove any dependence on the density ρ_1. This leads to the final expressions used here and in chapter 2

$$\begin{aligned}APE &= \frac{1}{2}h_1 h_2 \bar{k}_d^2(< (\psi_1 - \alpha\psi_2)^2 > + \alpha(1-\alpha) < \psi_2^2 >) \\ KE &= \frac{1}{2}(h_1(u_1^2 + v_1^2) + \alpha h_2(u_2^2 + v_2^2))\end{aligned} \tag{3.22}$$

where h_1 and h_2 are the fractional mean layer depths introduced previously.

3.4.2 Initial condition dependence

In chapter 2, stochastic forcing was implemented, modelling convective motions through the addition of hetons. In this chapter, no stochastic forcing is added, although a Rossby wave perturbation is added at the initial time in the lower layer to allow instabilities to develop. This subsection focuses on the dependence of the flow on this initial condition and stochastic forcing.

Figure 3.2 shows different analyses of the flow for the characteristic simulation of chapter 2 in burgundy. It also shows a simulation with the same parameters, namely no topography and the vertical shear parameter equal to $\epsilon = -0.5$. The difference here is the absence of stochastic forcing and the use of an initial Rossby wave perturbation in the lower layer. This simulation is represented in yellow in the following section, and

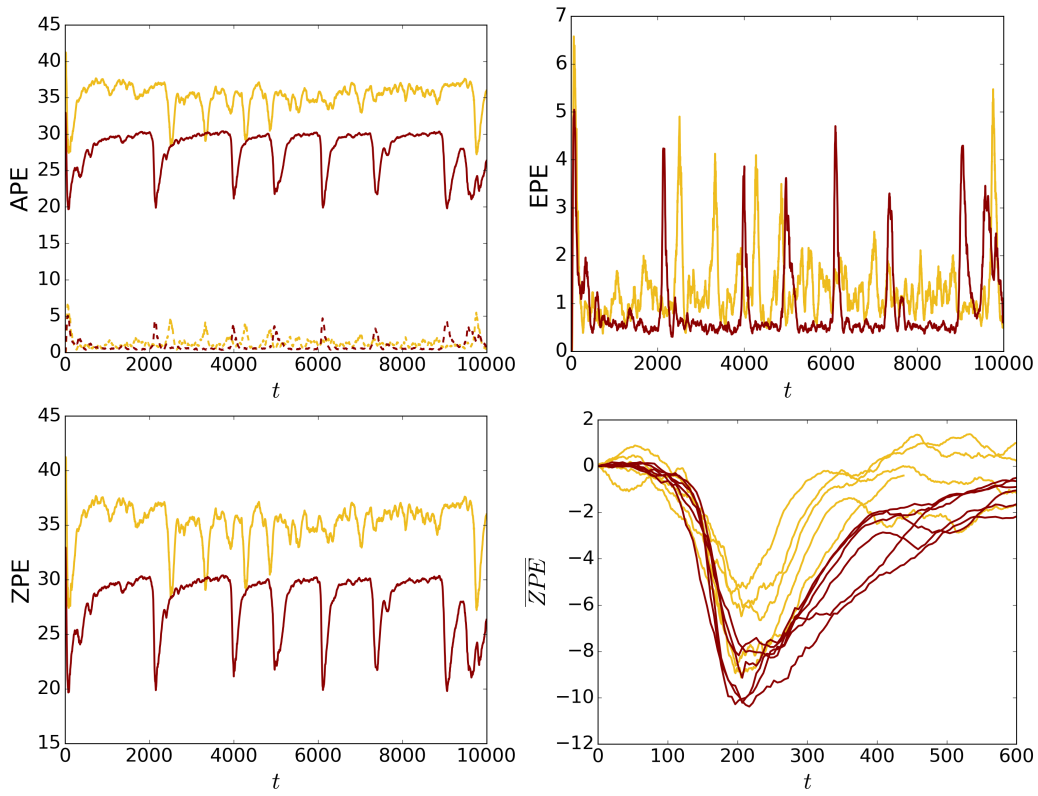

Figure 3.2: Top left panel: zonal available potential energy (solid lines) and eddy available potential energy (dashed lines). Top right panel: eddy available potential energy. Bottom left panel: zonal available potential energy. Bottom right panel: rearranged zonal available potential energy. In burgundy, the characteristic simulation of chapter 2, in yellow the reference simulation of this chapter (without topography).

will be called the reference simulation. The top left panel in figure 3.2 shows the zonal and eddy available potential energies. The zonal available potential energies (ZPE) at the top are considerably higher than the eddy available potential energies (EPE) closer to the bottom. The modal kinetic energies are very weak and therefore are not shown here. The top right panel in the figure concentrates on EPE and the bottom left panel in the figure concentrates on ZPE.

ZPE (and to a lesser extent EPE) are generally higher for simulations without stochastic forcing. The same simulations likewise show greater fluctuations from the mean value, as can be seen in the EPE plots (as well as in the ZPE plots). This means that in the absence of stochastic forcing, the flow is more energetic and fluctuates more. The stochastic forcing mixes the flow more efficiently, which has a damping effect. This damping decreases small fluctuations and generally reduces the energy over time. As in the characteristic simulation, the flow exhibits turbulent events distinguished by a fast and considerable

drop of ZPE and an increase of EPE. We see that in order to obtain a comparable ratio of energy fluctuations during quiescent phases to the drop of energy during turbulent events as in simulations forced with stochastic noise, we need to add sufficiently steep topographic slope (see further remarks in section §3.4.3).

The bottom right panel in the figure focuses on the different turbulent events. In this plot, for each turbulent event, ZPE values are shifted down by the first value of the considered window. We can see that turbulent events are more energetic in the characteristic simulation, the loss of ZPE being higher and steeper, while the recovery period is longer. In both cases, a secondary drop is visible during the recovery phase (as can also be seen in section §3.4.3). It is difficult to compare the time between two turbulent events due to their small number.

In summary, the stochastic forcing and the initial conditions have an impact on the flow, affecting the mean value of ZPE, the fluctuations, loss of energy during turbulent events and their recovery period. Stochastic forcing contributes to mixing and effectively results in turbulent damping. In the following, the yellow curves illustrated here will be considered as the reference simulation.

3.4.3 Topography dependence

This section uses the following colour coding to distinguish results for different topographies (i.e. $\tilde{\beta}_b$). For a constant value of the vertical shear parameter, we vary the topographic parameter $\tilde{\beta}_b$ from the margin of stability in blue to no topography in yellow, and up to a high positive topographic parameter in red. As in section §3.4.2, a burgundy line shows the characteristic simulation of chapter 2. The top left panel in figure 3.3 shows the growth rate as a function of the horizontal wavenumber for different topographic slopes. The solid lines are for an atmospheric stratification characterised by an exponential decrease of the density profile, the dashed lines are for an ocean-like like stratification under the Boussinesq approximation. Dark blue flat lines correspond to $\tilde{\beta}_b = -0.5$, light blue lines to $\tilde{\beta}_b = -0.4$, turquoise lines to $\tilde{\beta}_b = -0.25$, forest green lines to $\tilde{\beta}_b = -0.1$, light green lines to $\tilde{\beta}_b = -0.05$, yellow lines to $\tilde{\beta}_b = 0$, orange lines to $\tilde{\beta}_b = 0.05$, and red lines to $\tilde{\beta}_b = 0.25$. Qualitatively, both oceanic and atmospheric stratification display the same dependence on topography. The further we are from the margin of stability, the higher is the growth rate, with a small shift towards higher wavenumbers for higher topographies. However, the difference in the wavenumber for which the growth rate is the

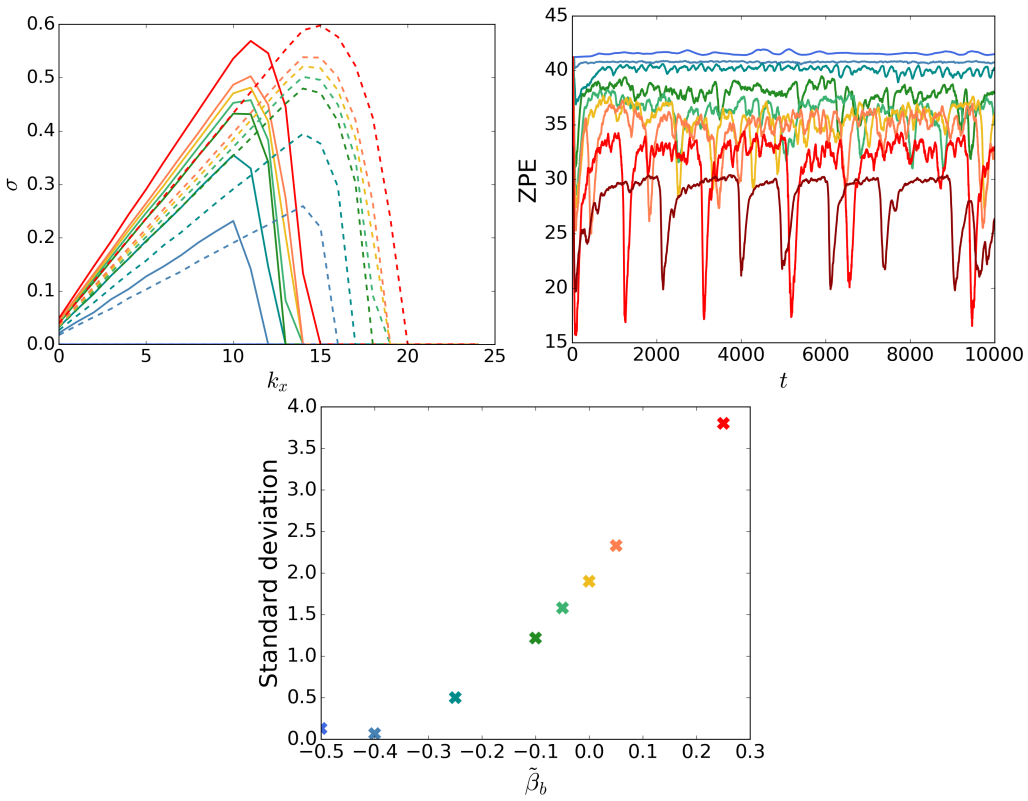

Figure 3.3: Growth rate versus horizontal wavenumber (top left panel), zonal available potential energy versus time (top right panel), standard deviation of ZPE (bottom panel) for different topographic slopes. In the top left panel, solid lines correspond to the atmospheric configuration and dashed lines correspond to the oceanic configuration. The colour code is: $\tilde{\beta}_b = -0.5$ in dark blue, $\tilde{\beta}_b = -0.4$ in blue, $\tilde{\beta}_b = -0.25$ in turquoise, $\tilde{\beta}_b = -0.1$ in forest green, $\tilde{\beta}_b = -0.05$ in light green, $\tilde{\beta}_b = 0$ in yellow, $\tilde{\beta}_b = 0.05$ in orange and $\tilde{\beta}_b = 0.25$ in red. The burgundy line in the right panel shows ZPE for the characteristic simulation of chapter 2.

highest is more pronounced between oceanic and atmospheric stratification. While atmospheric cases present a maximum growth rate for a wavenumber of $k_x = 10 - 11$, oceanic cases present a maximum growth rate for $k_x = 14 - 15$. Thus, atmospheric stratification favours larger scales, but results in slightly weaker baroclinic instabilities.

The top right panel in figure 3.3 exhibits the time evolution of ZPE for different topographic slopes. The following paragraphs focus on different aspects of these results to help understand the influence of topography on the flow's behaviour. First, we focus on simulations near the margin of stability, before studying simulations with a small topography and finally considering the impact of large topography.

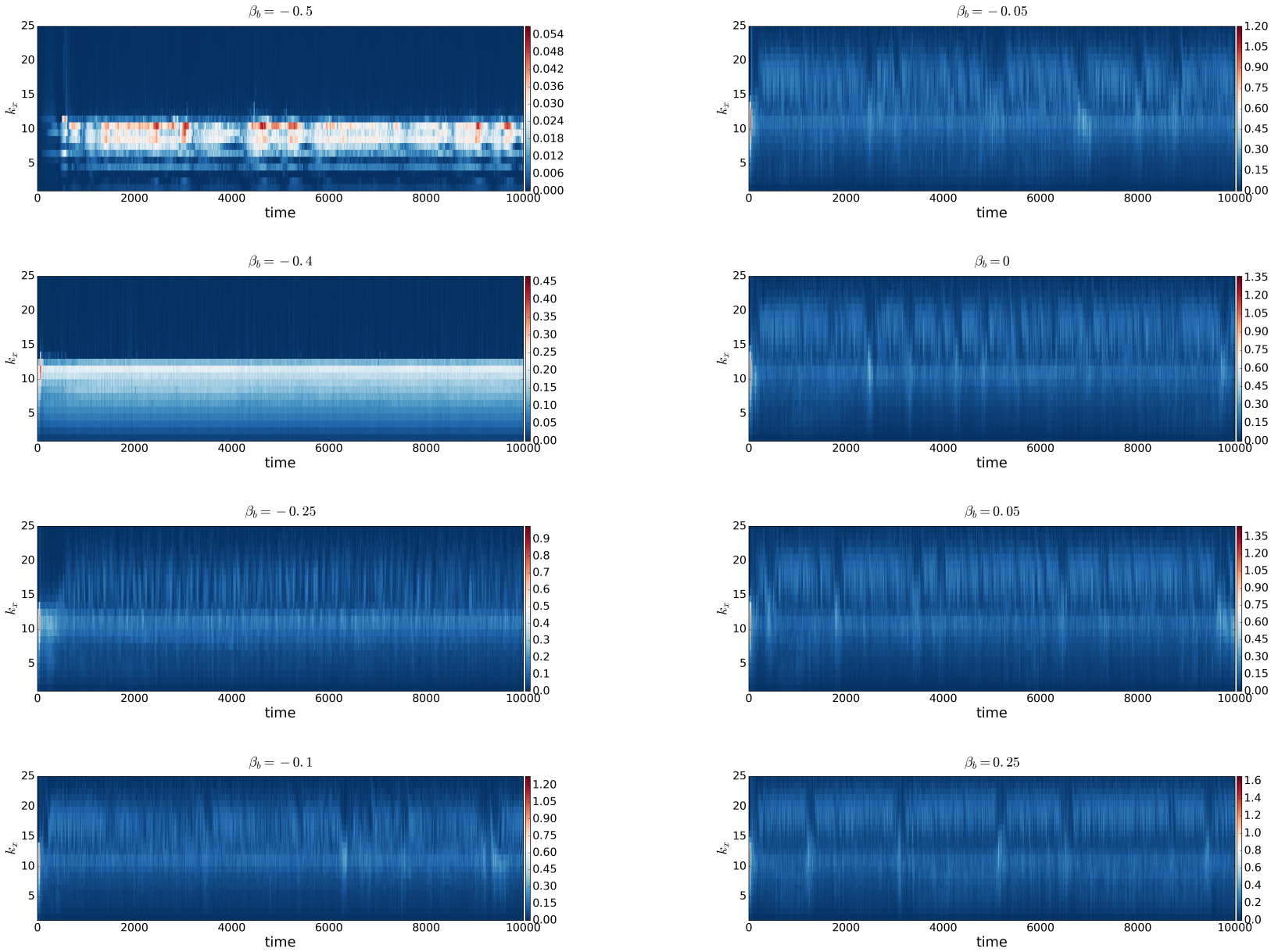

Figure 3.4: $\log_{10}$ of the maximum growth rate of the zonally-averaged flow versus zonal wavenumber k_x and time.

Margin of stability

In section §3.3, we found regions where the flow is stable using a linear stability analysis for a Boussinesq case. However, the Boussinesq approximation is not applied to the simulations run. Simulations were conducted to see if the margin of stability occurs for similar vertical shear and topographic parameters as in the Boussinesq case. Figure 3.5 shows ZPE for different topographic parameters: the upper blue line corresponds to $\tilde{\beta}_b = -0.5$, the lower blue line corresponds to $\tilde{\beta}_b = -0.4$, $\tilde{\beta}_b = -0.25$ for the turquoise line, $\tilde{\beta}_b = -0.1$ for the green line, and $\tilde{\beta}_b = 0$ for the reference simulation in yellow. In the Boussinesq case, the margin of stability occurs for $\tilde{\beta}_b = -0.5$.

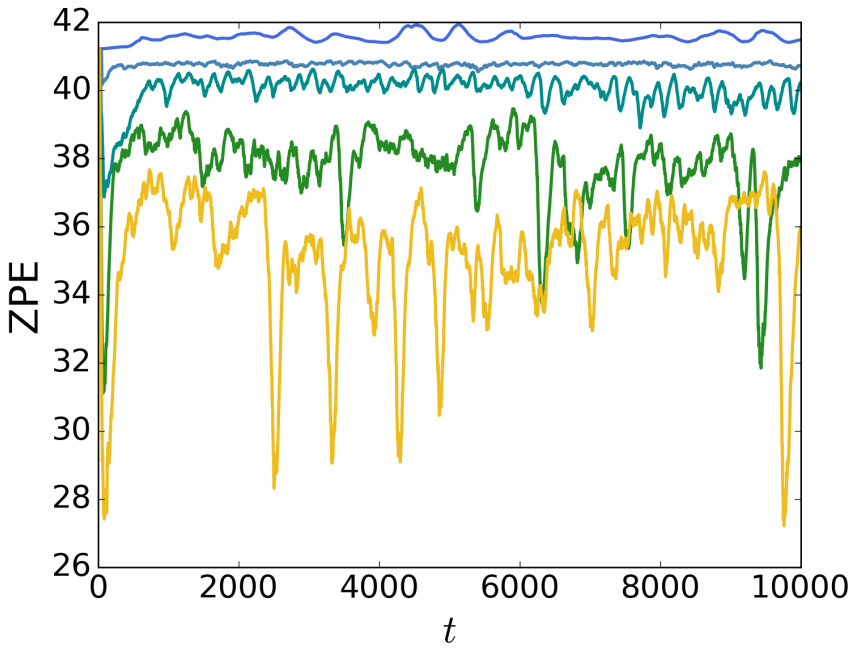

Figure 3.5: Evolution of the zonal available potential energy for different topographic slopes: $\tilde{\beta}_b = -0.5$ in dark blue, $\tilde{\beta}_b = -0.4$ in blue, $\tilde{\beta}_b = -0.25$ in turquoise, $\tilde{\beta}_b = -0.1$ in forest green and $\tilde{\beta}_b = 0$ in yellow.

The upper blue line ($\tilde{\beta}_b = -0.5$) exhibits strong stability with little variation in ZPE. When the flow is unstable and baroclinic instabilities can develop (as for the lower blue line corresponding to $\tilde{\beta}_b = -0.4$), there is an initial (small) drop in ZPE and a subsequent recovery to a reduced value at later times. The weak initial instability reorganises the zonal mean flow to a marginally stable state. As the initial flow becomes more unstable (see the turquoise line corresponding to $\tilde{\beta}_b = -0.25$), the initial drop in ZPE is larger and the recovery is less certain; a lower time-mean value of ZPE is found together with

more significant fluctuations associated with persistent weak baroclinic instabilities. The green line shows the evolution of ZPE for $\tilde{\beta}_b = -0.1$. After the initial (now larger) drop in ZPE, the flow exhibits numerous fluctuations and even turbulent events. The first turbulent events are smaller than in the reference simulation (in yellow), although the last one is comparable to those in the reference simulation. Figure 3.4 exhibits the maximum growth rate of the instantaneous zonally-averaged flow for various topographies. Growth rates are generally higher for higher values of $\tilde{\beta}_b$. The presence of an initial drop is visible and additionally weaker drops during turbulent phases are noticeable. The impact of topography on the turbulent events is discussed in the subsection below, focusing on the dependence of the flow on large topography.

It follows that, as for the Boussinesq case, the margin of stability occurs at $\tilde{\beta}_b = -0.5$ for $\epsilon = -0.5$. Additionally, the more we increase the topographic parameter, the more unstable the flow becomes. Baroclinic instabilities are often most pronounced at early times and the flow is globally more dynamic with higher topographic parameters. The initial instability tends to re-organise the flow into a less unstable basic state (with a lower mean value of ZPE), leading to weaker fluctuations in ZPE (weaker baroclinic instabilities) at later times.

Small topography dependence

The left panel in figure 3.6 shows ZPE variations for the reference simulation ($\tilde{\beta}_b = 0$) in yellow, and two simulations with a small topography. The green line shows a simulation with $\tilde{\beta}_b = -0.05$, and the orange line shows a simulation with $\tilde{\beta}_b = 0.05$. The time-averaged ZPE is greater for smaller values of topography: the green simulation has a greater time-averaged ZPE than the yellow simulation, which in turn has a greater time-averaged ZPE than the orange simulation. Fluctuations from the time-averaged ZPE are greater for higher values of the topography, as seen in the bottom panel in figure 3.3. Additionally, turbulent events are stronger, with, in addition, a greater drop of ZPE. The right panel in figure 3.6 shows the rearranged $\overline{\text{ZPE}}$ during turbulent events, i.e. shifted down by the first value of the considered time window. The drop of ZPE is comparable or larger for $\tilde{\beta}_b = 0.05$ than in the reference simulation, but smaller for $\tilde{\beta}_b = -0.05$ than in the reference simulation. Additionally, the slope from quiescent phases to turbulent events is steeper for higher topographic parameters. In other words, $\tilde{\beta}_b = 0.05$ slopes are steeper than $\tilde{\beta}_b = 0$ ones, which are steeper than $\tilde{\beta}_b = -0.05$ ones.

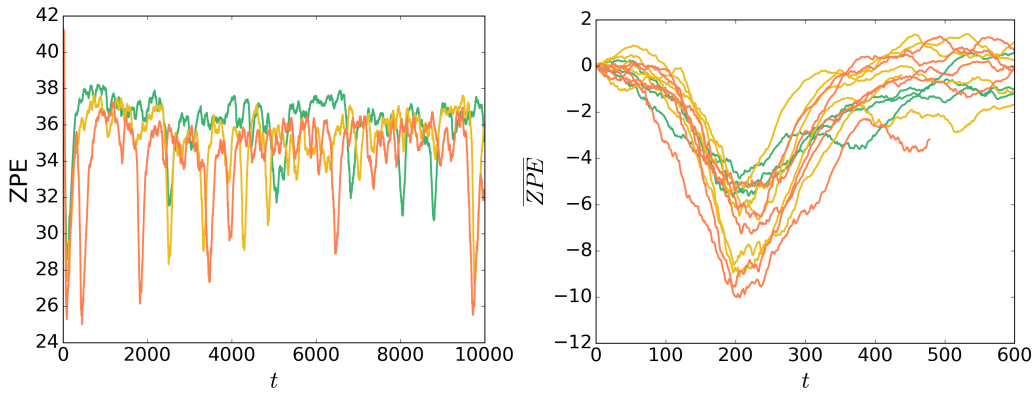

Figure 3.6: Evolution of the zonal available potential energy (left panel) and rearranged ZPE around turbulent events (right panel) for different topographic slopes: $\tilde{\beta}_b = -0.05$ in light green, $\tilde{\beta}_b = 0$ in yellow and $\tilde{\beta}_b = 0.05$ in orange.

This leads us to the conclusion that a small topography has a significant impact on the flow, and that ZPE is reduced with more oscillations for higher topographic parameters. Furthermore, turbulent events are more intense.

Large topography dependence

The previous two subsections discussed the impact of a small topography (either $\tilde{\beta}_b$ positive or $\tilde{\beta}_b$ negative) on the flow. In this part, we turn to the impact of larger topography. Three simulations are considered: first, the reference simulation, second, the simulation introduced in the margin of stability section with a topographic parameter equal to $\tilde{\beta}_b = -0.1$, and third, a simulation with a topographic parameter equal to $\tilde{\beta}_b = 0.25$.

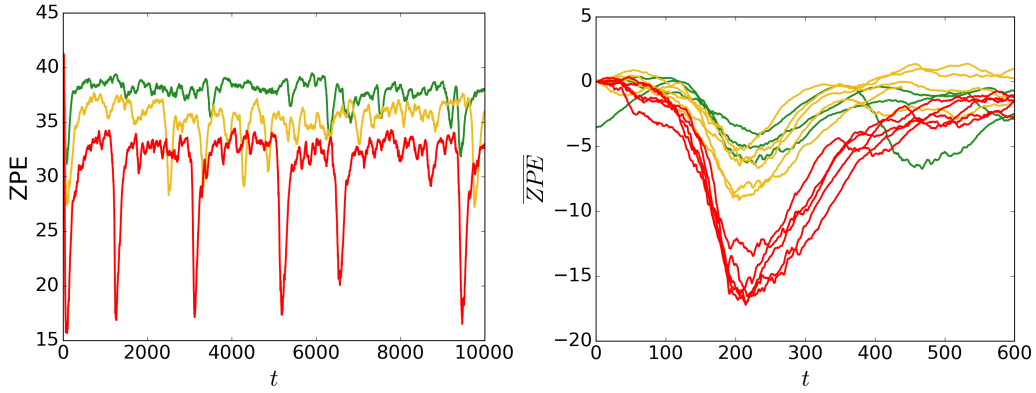

Figure 3.7: Evolution of the zonal available potential energy (left panel) and rearranged ZPE around turbulent events (right panel) for different topographic slopes: $\tilde{\beta}_b = -0.1$ in forest green, $\tilde{\beta}_b = 0$ in yellow and $\tilde{\beta}_b = 0.25$ in red.

The left panel in figure 3.7 exhibits the evolution of ZPE for the three simulations, with the reference simulation in yellow, $\tilde{\beta}_b = -0.1$ in turquoise, and $\tilde{\beta}_b = 0.25$ in red. The patterns observed above in the small topography cases recur, only with more pronounced variations. With increasing $\tilde{\beta}_b$, the time-averaged ZPE decreases. The increasingly turbulent character of the flow more effectively flattens interface displacements against the restoring effect of thermal relaxation. Fluctuations from the time-averaged value are also greater. It is difficult to accurately quantify the period between turbulent events, as we only have a small number of them. The simulation with $\tilde{\beta}_b = -0.1$ exhibits few turbulent events, which are also relatively weak. Again, their small number makes it difficult to compare the periods between them. The right panel in figure 3.7 shows the rearranged $\overline{\text{ZPE}}$ for these three simulations. The drop in ZPE is clearly greater in simulations with positive $\tilde{\beta}_b$ than in the reference simulation. The reference simulation, in turn, exhibits a greater drop in ZPE than in the simulation with a negative $\tilde{\beta}_b$. A similar pattern is found with regard to the slope between a quiescent phase and a turbulent event: the slope is steepest for positive $\tilde{\beta}_b$, followed by that found in the reference simulation, and is least steep for negative $\tilde{\beta}_b$.

Topography, then, has a strong impact on the flow. A positive $\tilde{\beta}_b$ results in more intense turbulent events. On the other hand, a negative $\tilde{\beta}_b$ is stabilising relative to a flat bottom; the reduction in mean ZPE is less, and turbulent events are weaker.

QGPV variations

We have seen that topography has a strong impact on the evolution of the flow and on the intensity of turbulent events. In this section, we focus on the evolution of the rearranged zonally-averaged QGPV (as introduced in section §2.3.1 of chapter 2). Figure 3.8 shows Hövmoller diagrams of the upper and lower layer rearranged PV. First, topography directly affects the lower layer PV. At the initial time, in the stable case ($\tilde{\beta}_b = -0.5$), the topography completely cancels the lower layer QGPV gradient. For larger $\tilde{\beta}_b$, the topography leads to reversed PV gradients relative to the upper layer, thus creating the potential for baroclinic instability. The upper layer PV range is only indirectly affected via the influence of the lower layer due to vertical mode interactions. Initial baroclinic instabilities develop in all simulations except for $\tilde{\beta}_b = -0.5$. For $\tilde{\beta}_b = -0.4$, small variations of the PV are visible, but the flow exhibits strong overall stability. Jets are present but remarkably weak and thus scarcely visible. For $\tilde{\beta}_b = -0.25$, the flow is still very steady, though

jets are more visible here than in the previous simulation. The first turbulent events are clearly visible for $\tilde{\beta}_b = -0.1$. Only a small number of weak turbulent events are visible until $t = 9000$. They are characterised by a breakdown of the staircase profile with a tendency to adopt a more linear profile. A larger turbulent event is visible between $t = 9000$ and $t = 10000$. All simulations for larger $\tilde{\beta}_b$ exhibit prominent turbulent events.

In addition, some simulations exhibit latitudinal jet drifts, either northward (e.g. for $\tilde{\beta}_b = -0.1$) or southward (e.g. for $\tilde{\beta}_b = -0.25$ and $\tilde{\beta}_b = 0$). We know that in Nature, jets can drift (see Thompson and Wallace [2000] and Barnes and Polvani [2013]). Boland et al. [2012] observed jets drifting in a two-layer quasi-geostrophic model with a sloping meridional and a sloping zonal topography. They attribute the jets' drift to the difference of orientation between the PV gradient in each layer and the barotropic PV gradient. This explanation, however, cannot be applied to our study, as no zonal topography is present. Drifting jets were also observed in chapter 2, but not all drifted in the same direction. Typically, the central jet remains at the same latitude, while the nearest jet north of it drifts southward and symmetrically, and the nearest jet south of it drifts northward. In contrast, our study includes simulations in which all jets drift in the same direction. This was previously observed by Panetta [1993] and Smith et al. [2014], who noted that jet drift (and merger or split) is associated with the domain width not being an integer multiple of the Rhines scale.

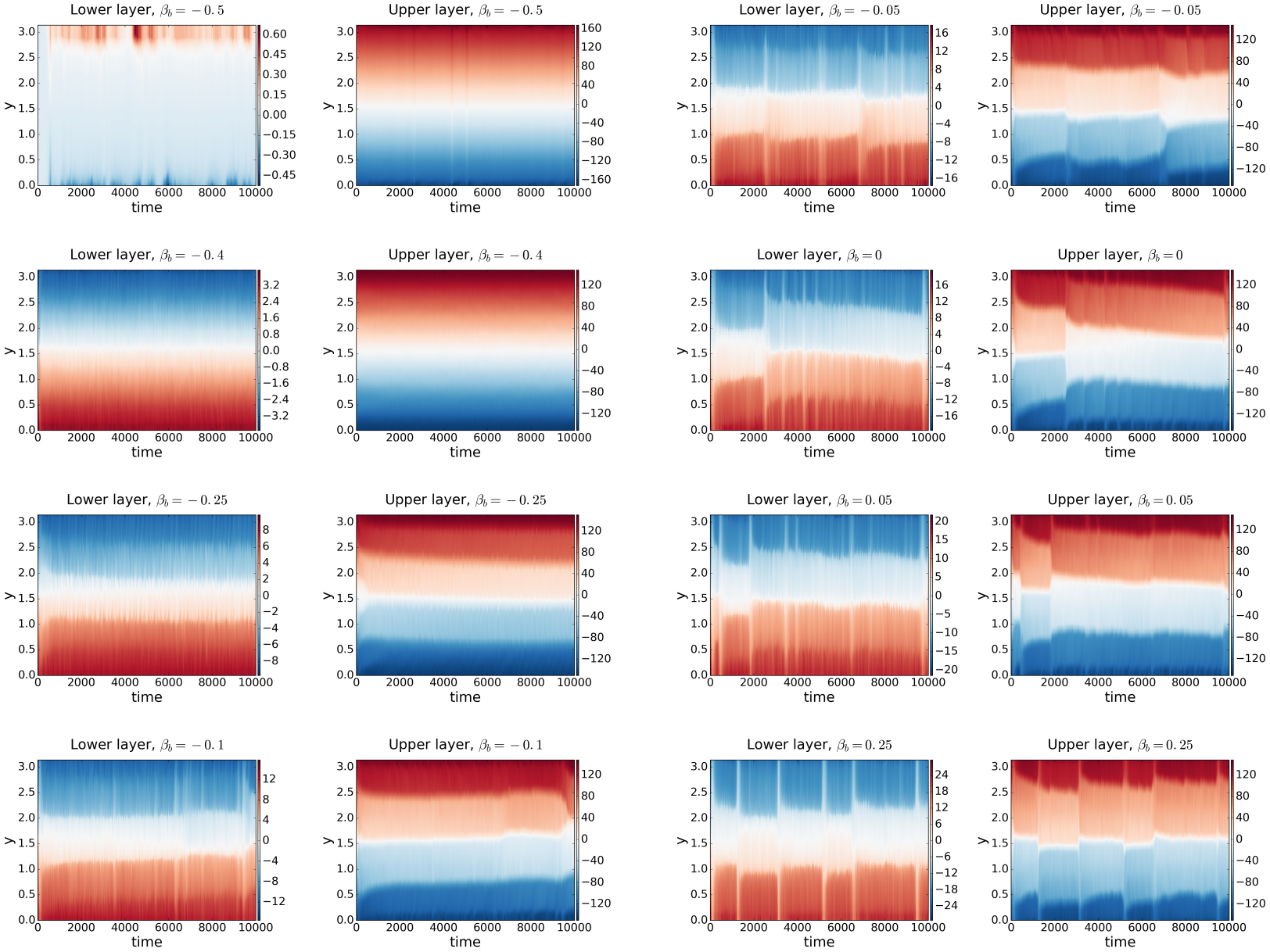

Figure 3.8: Hövmoller diagram of the rearranged QGPV in the upper and lower layers for different topographic parameter $\tilde{\beta}_b$.

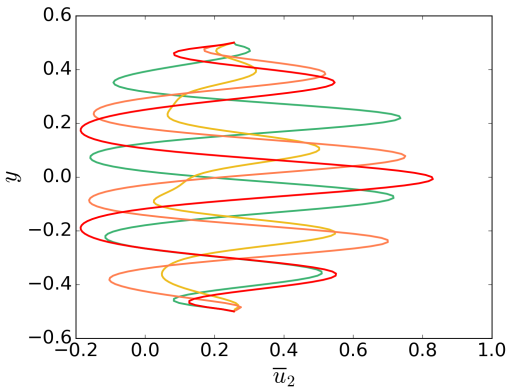

Figure 3.9: Zonally-averaged zonal velocity averaged over the entire simulation, for different topographies: $\tilde{\beta}_b = -0.05$ in light green, $\tilde{\beta}_b = 0$ in yellow, $\tilde{\beta}_b = 0.05$ in orange and $\tilde{\beta}_b = 0.25$ in red.

Thompson [2010] found that jet spacing is characterised by the barotropic Rhines scale L_{Rhbt}. He defined it as $L_{Rhbt} = 2\pi\sqrt{U_e/\beta_{bt}}$, with U_e the eddy velocity nondimensionalised by U_s, where $U_s = \bar{u}_2 - \bar{u}_1$ is the shear velocity, and $\bar{u}_i$ is the mean velocity in layer i, and $\beta_{bt} = \beta L_d^2/U_s + s_l/2$ with $s_l = \alpha_{sl} f_0 L_d^2/(U_s H)$, where α_{sl} is a constant (unspecified) and H the mean layer depth. Following the approach of Thompson [2010], we compute both the barotropic Rhines scale $L_{Rhbt} = \pi\sqrt{U/\beta_{bt}}$ (marked by circles in the top panels in figure 3.10), with, in our case, $\beta_{bt} = \beta(1 + \tilde{\beta}_b)$, and the usual Rhines scale $L_{Rh} = \pi\sqrt{U/\beta}$ (marked by crosses in the top panels in figure 3.10). We multiply by a factor of π to rescale it to our domain's size and thus define it as a wavelength, not a wavenumber. As in Dritschel and McIntyre [2008], we choose for U either U_{vortex} defined as the vortex peak velocity, as in the top left panel in figure 3.10, or $U_{jet} = \max u - \min u$, as in the top right panel in figure 3.10. In the top left panel, values of the barotropic Rhines scale decrease with $\tilde{\beta}_b$, despite our result from figure 3.9, namely, that jet spacing increases with $\tilde{\beta}_b$. However, the usual Rhines scale using U_{vortex} qualitatively matches observations from figure 3.9. U_{jet} values are obtained from the maximum and minimum values of the zonally-averaged zonal velocity. As jets shift from one quiescent phase to another, the time averaged flow is not a good representation of the flow for some simulations (e.g. for $\tilde{\beta}_b = 0$). The Rhines scale defined with U_{jet} is thus not appropriate when jets drift or shift, to represent jet spacing. Here, neither the barotropic Rhines scale nor the Rhines scale defined with U_{jet} are a good representation of jet spacing.

The bottom panels in figure 3.10 exhibit two other ways to compute a qualitative jet spacing. In both panels, the Rhines scale is defined by $L_{Rh} = 5^{1/4}\sqrt{U_{rms}/\beta}$ as in Scott and Dritschel [2018], with U_{rms} the root mean square of the velocity over the

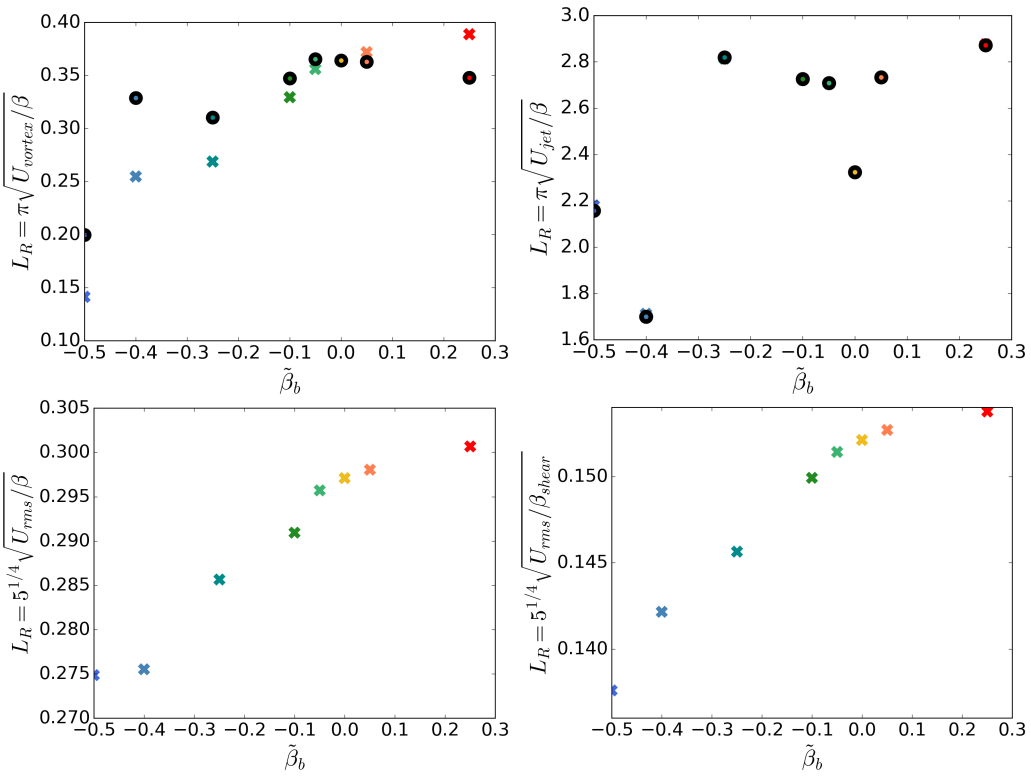

Figure 3.10: Four different ways to compute the Rhines scale for different topographic slopes. The top left panel shows $L_{Rhbt} = \pi\sqrt{U_{vortex}/\beta}$ for crosses and $L_{Rhbt} = \pi\sqrt{U_{vortex}/\beta_{bt}}$ for circles; the top right panel shows $L_{Rhbt} = \pi\sqrt{U_{jet}/\beta}$ for crosses and $L_{Rhbt} = \pi\sqrt{U_{jet}/\beta_{bt}}$ for circles; the bottom left panel shows: $L_{Rh} = 5^{1/4}\sqrt{U_{rms}/\beta}$; the bottom right panel shows: $L_{Rh} = 5^{1/4}\sqrt{U_{rms}/\beta_{shear}}$. The colour code is: $\tilde{\beta}_b = -0.5$ in dark blue, $\tilde{\beta}_b = -0.4$ in blue, $\tilde{\beta}_b = -0.25$ in turquoise, $\tilde{\beta}_b = -0.1$ in forest green, $\tilde{\beta}_b = -0.05$ in light green, $\tilde{\beta}_b = 0$ in yellow, $\tilde{\beta}_b = 0.05$ in orange and $\tilde{\beta}_b = 0.25$ in red.

entire domain, i.e. $\sqrt{2KE}$. In the right panel, instead of using β as on the left, we use $\beta_{shear} = \beta_2 - \beta_1$ with β_i the time-averaged zonal mean PV gradient in layer i. Both results show a good qualitative agreement with figure 3.9. These different graphs confirm the fact that the Rhines scale is only one possible qualitative estimation of jet spacing.

3.5 Conclusion

In this chapter, we investigated the impact of a sloping topography on a very idealised two-layer quasi-geostrophic shallow water model with an imposed vertical shear maintained by thermal relaxation. This model is based on the model used in chapter 2, although differing from it through the absence of stochastic forcing and the early introduction of

a lower layer Rossby wave perturbation. These differences have an impact on the flow. Simulations with stochastic forcing exhibit a lower mean value of ZPE and overall energy, as well as fewer small fluctuations. Stochastic forcing contributes to the mixing and damps perturbations over time. It further intensifies turbulent events, causing a greater and steeper decrease in ZPE, followed by a longer recovery period.

Topography also has a strong impact on the flow. A linear stability analysis has been carried out to determine the conditions favouring baroclinic instability. Topography that deepens northwards was found to be destabilising and vice-versa. This analysis was then used to choose appropriate initial conditions for a series of nonlinear simulations investigating the impact of topography. By running different simulations for various topographies without changing the constant vertical shear, we were able study the flow's behaviour from the margin of stability to unstable cases exhibiting oscillations between quiescent phases and turbulent events. Close to the margin of stability, the flow is very steady, and only a small initial drop in energy is visible due to baroclinic instability developing. This is followed by a steady phase, where jets are more or less visible depending on the topography. For simulations further away from the margin of stability, the first turbulent events appear. The greater the topography, the more intense the turbulent events, with high, steep drops of ZPE. Topography impacts the mean value of ZPE, which is smaller for higher values of the topographic parameter. Jet spacing also depends on topography, and is found to increase with the topographic parameter, i.e. with the effective β in the lower layer, contrary to a naive interpretation of the Rhines scale.

Finally, we observe continuous latitudinal drifts of jets. In chapter 2, jets were also found to drift, but they were not all moving in the same direction. Here, on the other hand, we find jets drifting together northward or southward. Further work on jet drifting would be an interesting addition to this study. Is the drifting direction randomly distributed? Does the direction depend on the topography or on the PV gradient in one of the two layers? Are drifting jets more stable (with fewer turbulent phases) than steady jets? Do drifting jets change the period between two turbulent phases?

Chapter 4

Occurence and evolution of waves and vortices at a front in amplitude vacillation.

4.1 Introduction

In the 50's and 60's, Hide [1953], Hide [1958], Fultz et al. [1959] and Hide and Fowlis [1965] started using rotating tanks of cylindrical geometry with the flow induced by a lateral temperature gradient. The idea of using a temperature gradient in a rotating tank goes back to James Thomson in 1882, who had the original idea to heat an outer ring at the bottom of the tank, representing the equator, and to cool the surface, representing one pole. The experiment of Hide consisted of three concentric cylinders, the outer ring filled with hot water, the inner ring filled with cold water and in between the ring where the circulation should take place, which he called the 'convection chamber'. He observed jets of different baroclinic modes emerging from the flow and analysed them. In addition to the baroclinic modes, he observed an oscillation in the amplitude of the baroclinic instability, which he called amplitude vacillation. Thus, the study of jets started with the study of Hide [1958]. Following these studies, different groups have continued to work with this setup, although, now, most of the apparatus is with hot water in the inner cylinder, as in Hide and Mason [1970] and Bastin and Read [1997]. Amplitude vacillation has been studied in various ways, theoretically by Lindzen et al. [1982], numerically by Ohlsen and Hart [1989] and Randriamampianina et al. [2007] or experimentally by

Buzyna et al. [1989], Larcher et al. [2005], Harlander et al. [2011] and Scolan et al. [2014].

Investigating the baroclinic instability regime is fundamental, as baroclinic instabilities are a predominant source of stirring in the oceans and in the planetary atmospheres, as presented in Galperin et al. [2004], Maximenko et al. [2005] and Richards et al. [2006], the small scales eddies created by baroclinic instabilities might be responsible for the energy input to form zonal jets.

To investigate the formation of jets in planetary atmospheres, Read et al. [2007] conducted experiments on the thirteen metre large Coriolis platform. Topography was used to simulate the variation of the Coriolis force with latitude, assuming a constant variation with latitude also known as the β-plane. Salty water was sprayed at the surface to model vertical convection. The idea of adding a conic topography to a baroclinic experiment goes back to Mason [1975]. This strong β-topography and the small-scale input will create large-scale zonal structures, separated by a distance close to the Rhines scale as on the Earth's oceans, see Richards et al. [2006], or on planetary atmospheres, see Vasavada and Showman [2005].

More recently, Scolan and Read [2017] have built a new experimental setup to study baroclinic instabilities created by convection motions. They use an annulus in which they cool a ring-shaped region near the surface close to the centre and heat a ring-shaped region at the bottom. They obtain two turbulent convective regions near the inner and outer boundary and a baroclinic region in the centre. Varying the rotation rate and the differential heating allows them to study different regimes, and to observe the interactions between convection and baroclinic instabilities.

Rodda et al. [2018] studied another kind of differentially heated rotating annulus, using the classical configuration of Hide. They added a salt stratification to the experiment and observed internal gravity waves emitted from large-scale baroclinic jets.

In 1972, Hart decided to use salinity instead of temperature to impose the density gradient. He used two immiscible fluids to do his experiments, silicone oil and salty water, which corresponds to the Phillips model, see Phillips [1951]. Following this approach, Ohlsen and Hart [1989], Lovegrove et al. [2000] and Williams et al. [2005] have continued the work on large-scale phenomenon, with amplitude vacillation, but they also started to focus on smaller-scale effects such as waves. Flór et al. [2011] and Scolan et al. [2014] have started to study the dynamics of fronts and waves in a relatively large 2m wide rotat-

ing tank with two miscible fluids, salt-stratified with a rigid lid, capturing various instabilities, such as Kelvin-Helmholtz, Holmboe and Rossby Kelvin instabilities, and possibly, the emission of spontaneously emitted internal gravity waves. Miscible fluids have the advantage of allowing the opportunity to have a continuous density gradient between the two layers. Here, we are focusing on the emergence and interaction between fronts waves and vortices in the baroclinic unstable regime with amplitude vacillation. Can we confirm the existence of spontaneous emitted inertia-gravity waves observed in Flór et al. [2011] and Scolan et al. [2014], do these small waves play a role for the generation of vortices, and how does this regime change with Rossby number? To investigate these questions, I further processed the data acquired on fronts by Jo-Hendrick Thysen (MI student in 2014 in the MEIGE team at the LEGI, direction JB Flór), and have conducted some tests for similar parameters to become familiar with the flow evolution and measurement procedure (see table 4.1, experiments in green), as a mean to better interpret our results. To obtain more information about this front and wave field, we employed novel approaches in examinations of the entire flow field's modes. However, interesting insight was further gained by exploring the derivative of the density fields and their contours.

This chapter is structured as follows: section §4.2 presents the experimental setup and the dimensionless parameters. Next, section §4.3 focuses on the different analyses we use to inspect the data. We then present two experiments and analyse them in section §4.4. Finally, we conclude with section §4.5.

4.2 Experimental setup

4.2.1 Apparatus

We use a cylindrical tank of 1.3 metre diameter and 50cm working depth, filled with 30cm of fluid. The tank is placed on a rotating platform, which can spin at a maximum speed of πrad s^{-1}. To create a vertical shear between the two layers and to be able to enter the baroclinic instability regime, we use a rigid lid spinning faster than the rotating platform (as in Hart [1972]), which creates an inverse parabolic profile ($h(r) = -Ar^2$, with A a constant, r the radius and h the interface height). Figure 4.1 exhibits the apparatus of the experiments. This profile is due to Ekman pumping induced by the rigid lid. As the rigid lid spins faster than the rotating platform, it provokes a transport at the surface to

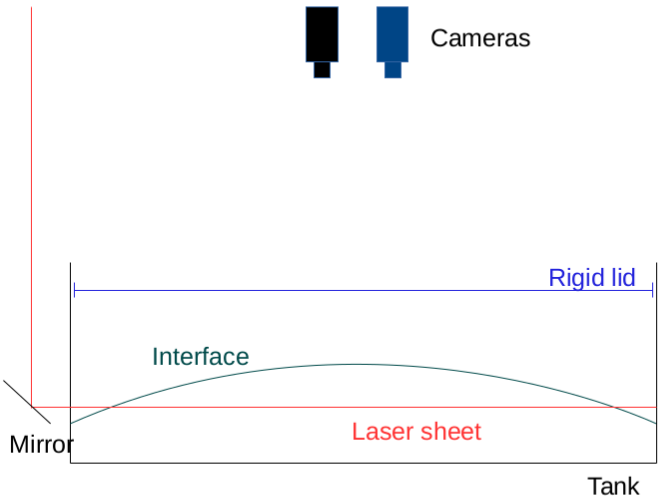

Figure 4.1: Apparatus of the experiments, with the rotating tank in black, the rigid lid in blue, the parabolic interface in green and the horizontal laser sheet which intersects it, in red, and two cameras on top.

the outside of the tank, which pumps the fluid up in the centre, thus leading to a parabolic profile. The shape of the profile has been theoretically studied by Berman et al. [1978] and Bradford et al. [1981]. The entire platform is covered by a green tarpaulin to avoid light beams reflecting in the entire laboratory and to prevent light from outside entering the platform.

We use different methods to detect the fluid motions: particle image velocimetry (PIV) and laser-induced fluorescence (LIF). For the PIV, we use orgasol particles of diameter 60μm, of a density of $1.02 - 1.04$ kg L^{-1} for the lower layer and of 1.014 kg L^{-1} for the upper layer. The particles are illuminated by a Coherent Verdi solid $Nd : YVO_4$ continuous laser, with a 532 nm wavelength and a maximum power of 5 watts. To create a horizontal laser sheet, we use a system of mirrors which brings the laser at the top of the platform to an oscillating mirror, which generates a vertical sheet which is subsequently converted into a horizontal sheet via a mirror at an angle of 45 degrees. We synchronise the oscillating mirror with the camera's exposure time, such that one exposure covers an entire number of oscillations. The position of the oscillating mirror is controlled by a computer, so that the vertical position of the laser sheet in the tank can be chosen and either a horizontal sheet via the inclined mirror is generated or a vertical sheet is generated. Here, we only use views of the horizontal plane. To detect the particles, we use a Dalsa 1M60 camera, with a Nikkon AF 20mm f2.8d A lens, on which we put a band passed filter FF01-543/3-50. Section §4.3.5 presents the method of analysis used to study

the particle measurements.

For the LIF measurements, we use rhodamine 6G with a concentration of 6.5×10^{-5} kg L^{-1}. The rhodamine is mixed into one of the two fluid layers; the upper layer in the experiments is considered here. It fluoresces with a different wavelength when excited with the laser light. As the lower layer does not have any dye and the laser beam intersects the two layers, the interface between the two layers is visible from the contrast in light intensity. Thus, the evolution of the interface between the two layers is visible from the contrast between the layers. The second camera is also a Dalsa 1M60, with a Nikkon AF 20mm f2.8d A lens and a band-passed filter HOYA 62mm R(25A) and allows us to observe only the fluorescein dye. Sections §4.3.1, §4.3.2, §4.3.3 and §4.3.4 present the analysis of the LIF measurements.

In order to correct the refractive index variations near the interface caused by the gradient in salt-concentration, we add a specific amount of alcohol to the watery upper layer fluid. Here, we used the relations linking density and optical indices from Daviero et al. [2001] to match the optical indices and obtain the expected density ratio. Note that by adding alcohol to plain water, we decrease its density and thereby increase the density ratio.

The density and the temperature of each layer is measured using an Anton Paar density metre DMA 35N. The optical index is measured with a Brix refractometer.

4.2.2 Dimensionless Parameters

Following former investigations (see Gula et al. [2009], Flór et al. [2011] and Scolan et al. [2014]), we characterise the flow by the Rossby number and the Burger number. The Rossby number characterises the effect of inertial forces compared to Coriolis forces. For very small Rossby numbers, the flow is in geostrophic balance, whereas for $Ro > 0.5$, a-geostrophic effects become important. This has consequences for the stability of the flow, as has been shown in the stability regime diagrams in the Rossby-Burger number space (see Flór et al. [2011]). We define the Rossby number as $Ro = \Delta\Omega/(2\Omega)$, with Ω the rotation frequency of the tank, and $\Delta\Omega$ the rotation frequency of the rigid lid compared with the tank.

The Burger number is defined by $Bu = g'H/f^2R^2$, with $R = 65cm$ the radius of the tank, H the height parameter defined as $H = H_1H_2/(H_1 + H_2) = 15$cm, f the Coriolis

Experiment	Ω	$\Delta\Omega$	g'	Ro	L_d	Bu	Re	d
	$rads^{-1}$	$rads^{-1}$	cms^{-2}		cm		$\times 10^4$	
	0.25	0.093	12.821	0.186	25.41	0.153	3.929	0.043
	0.25	0.143	12.821	0.286	25.41	0.153	6.042	0.028
	0.25	0.193	12.821	0.386	25.41	0.153	8.154	0.021
	0.25	0.243	12.821	0.486	25.41	0.153	10.267	0.016
	0.3	0.093	13.983	0.155	22.46	0.120	3.929	0.045
1	0.3	0.243	13.983	0.405	22.46	0.120	10.267	0.017
	0.3	0.293	13.983	0.488	22.46	0.120	12.379	0.014
2	0.3	0.343	13.983	0.572	22.46	0.120	14.492	0.012
	0.3	0.393	13.983	0.655	22.46	0.120	16.604	0.011
	0.3	0.493	13.983	0.823	22.46	0.120	20.829	0.009
	0.7	0.28	549.448	0.2	64.81	0.1	11.830	0.020
	0.7	0.28	489.900	0.2	61.17	0.1	11.830	0.020
	0.7	0.42	489.900	0.2	61.17	0.1	17.745	0.013

Table 4.1: Parameters used in the different experiments, in blue the experiments of Jo-Hendrick Thysen, in green the experiments of Thibault Jougla.

parameter $f = 2\Omega$, $g' = 2g(\rho_1 - \rho_2)/(\rho_1 + \rho_2)$ the reduced gravity with $g = 9.81$m s^{-2} the gravity parameter, and ρ_1 and ρ_2 the density in, respectively, the bottom and top layer, giving typical values of the order of $g' = 10 - 15$cm s^{-2} (see table 4.1). It indicates the impact of stratification compared with rotation, with baroclinic instability occurring for values of $Bu < 0.1$. We can write the Burger number as $Bu = (L_d/R)^2$, with $L_d = \sqrt{g'H}/f$ the Rossby radius of deformation, i.e. the radius at which rotation affects a gravitationally driven flow.

Further relevant numbers are the aspect ratio, which is $\gamma = H/R = 15/65 \simeq 0.25$, the Reynolds number, which characterises inertial forces compared to viscous forces and is equal to $Re = \Delta\Omega R^2/\nu$, the dissipation number d characterising the ratio of the typical time scale linked with the forcing compared with the time of the spin-down, $d = 1/\Delta\Omega/(H/\sqrt{\nu\Omega}) = \sqrt{\nu\Omega}/H\Delta\Omega$.

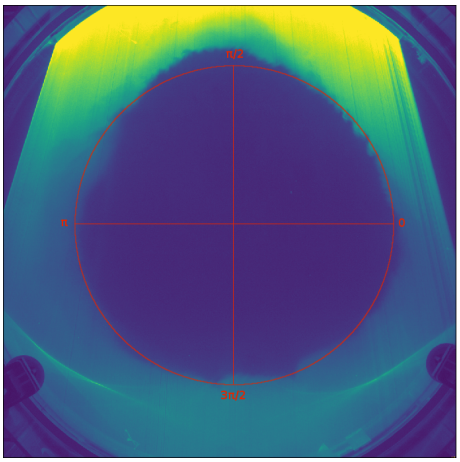

Figure 4.2: Raw LIF image with a red circle around a radius $r = 41cm$ showing where the light intensity is caputred for experiment 1 at time 410s.

4.3 Data analysis methods

Different methods have been developed to analyse the flow. Section §4.3.1 presents an analysis of the light intensity variation around a circle. Section §4.3.2 presents a method detecting the contour of the front. Another method of a polar interpolation followed by a radial average to detect is presented in section §4.3.3. Then, a method of the derivative of the density field is presented in section §4.3.4. Finally, section §4.3.5 shows the particle image velocimetry method to obtain the vertical vorticity of the flow.

4.3.1 Analyse around a circle

The interface between the two layers is made visible by the light intensity variation (dark in the lower layer and lit in the upper layer). Since the front's basic stable state is circular, an analysis of the light intensity variation around a chosen circle was developed following Vincze et al. [2013] and Thysen [2014]. Using this method, we detect small wavenumber perturbations rather than large wavenumber perturbations. Here, we aim at visualising small-scale wave perturbations. First, we choose the radius of a circle, see the red circle in figure 4.2. In their methods, the circle is centred in the centre of the tank, which might be shifted from the centre of the image. Next, we look at the light intensity variations around this circle. Plotting the light intensity variations with angular position against time, we can create a Hövmoller diagram. The evolution of the flow, the propagation of waves, and the formation and the evolution of vortices are visible on such a diagram.

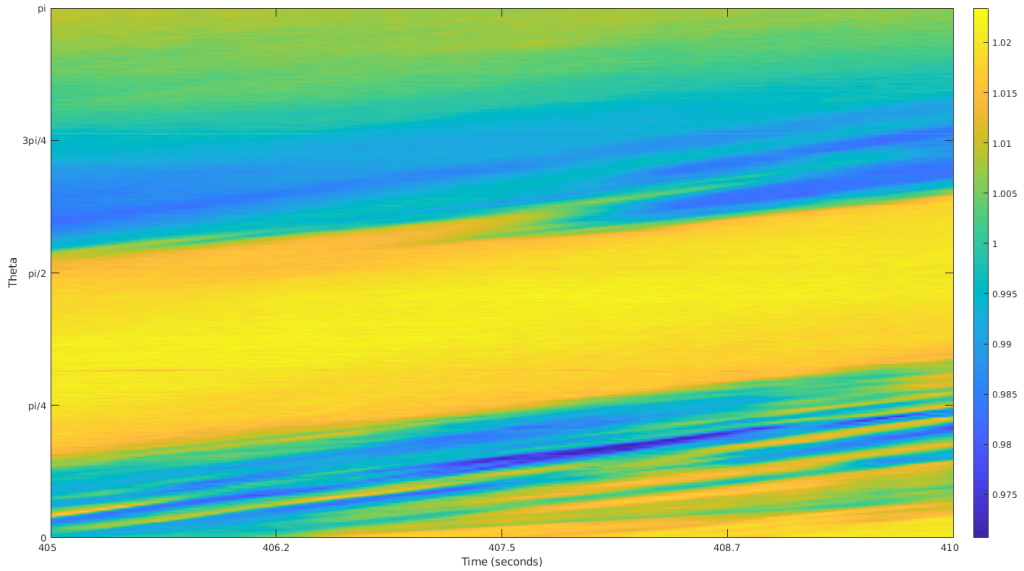

Figure 4.3: Hövmoller diagram of the light intensity around a radius $r = 41cm$ for experiment 1.

Figure 4.3 shows the light intensity around a circle of a radius of $r = 41$cm for experiment 1 between times $t = 405$s and $t = 410$s. We can see the different waves with varying wavelengths propagating, as well as waves emerging, e.g. around $t = 409$s just above $\pi/4$, where new waves with higher wavelengths appear.

Figure 4.4 shows four different diagrams. The top panel represents the light intensity around a chosen circle $r = 41cm$. In order to improve the resolution, data is interpolated to a finer grid. We then subtract the temporal mean to emphasise the emerging waves rather than the permanent wavenumbers. The second panel in figure 4.4 shows the fft – calculated for each unit of time – of the light intensity around the circle considered here.

The shape of the interface is no longer circular as soon as small wavenumber perturbations appear, in which case large wavenumber perturbations may not be visible; thus, small wavenumber perturbations may outside the chosen circle and thus not be visible. Therefore, instead of considering only one circle, we considered a ring and radially-multiply the data by either a Gaussian, a constant, or a sinusoidal function. We eventually opted for a sinusoidal function, which best captures the radial variations. It is defined by $data(r) = data(r)\cos(\pi(r - r_1)/(\delta r))$, with $r_1 = 41cm$ the originally chosen circle and $\delta r = 2.5cm$ a small radial displacement. This method deletes the mean value and highlights variations from the mean value. The rearranged data are visible in the third panel in figure 4.4. As above, we compute the fft of the rearranged data. It is shown in

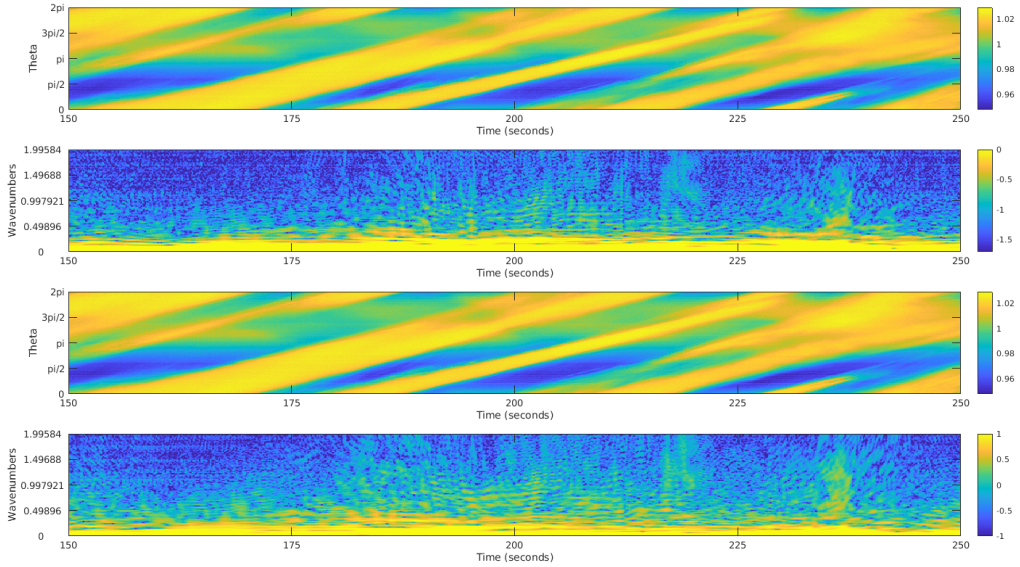

Figure 4.4: First panel: Hövmoller diagram of the light intensity around a radius $r = 41cm$ for experiment 1. Second panel: spectral diagram as a function of time, obtained from the light intensity in the first panel. Third panel: Hövmoller diagram of the rearranged light intensity around a radius $r = 41cm$ and $\delta_r = 2.5cm$. Fourth panel: spectral diagram versus time, obtained from the light intensity in the third panel.

the fourth panel of figure 4.4, it is neater and high wavenumbers are more clearly visible than in the second panel.

4.3.2 Contour analysis

A contour detection method was developed to enable us to capture the different waves and large-scale behaviour of the flow. By examining a light level contour, we can estimate the different wavenumbers. To this end, we first have to capture the adequate light level. Next, we can find the arc-length of the contour and compute the fft. Finally, we consider the time evolution of the wavenumbers. The following paragraphs elaborate the different steps of this method.

First, the image is cleaned to avoid capturing any spurious effect. To exclude contours around the edge of the tank and because the dynamics take place in its centre, we create a circular mask, whose diameter is defined by the size of the image. Next, to remove small-scale fluctuations that we consider noise, we apply a smoothing routine, which will be presented in the following paragraph. We then choose a light level (see below for more details) and obtain the contour at this light level. Note that the contour is obtained

in a grid four times finer than the original image, which gives a very precise and neat contour, and using the contour detection algorithm developed by Dritschel and Ambaum [1997]. Next, we compute the arc-length of the contour between contour points. Then, we redistribute the contour points so that each point is separated from the next one by the same arc length. Thus, for each point on the contour, we obtain its position (x, y) as a function of arc length s. Finally, we compute the 1D ffts of $x(s)$ and $y(s)$. By summing the square of the two spectra, we obtain the power spectrum of the contour shape.

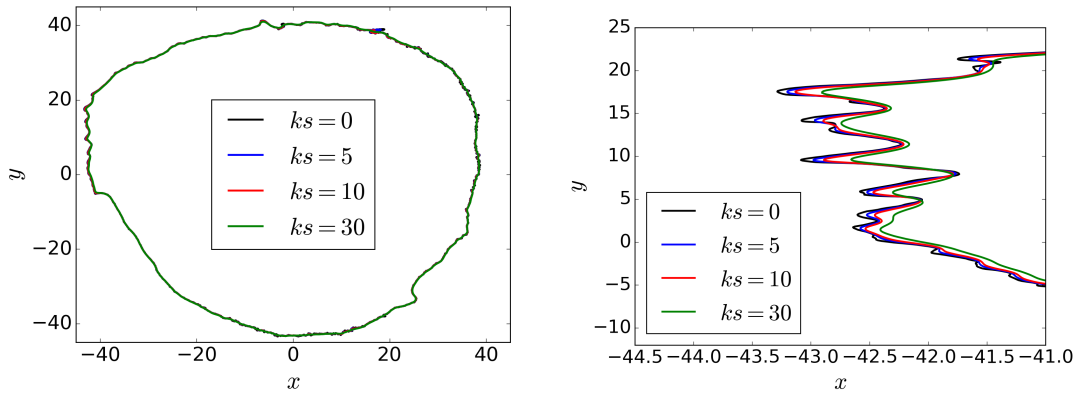

Figure 4.5: Contours obtained from experiment 1, at time $t = 405$s for the light level $l = 32882$ for four different levels of smoothing. Black line: no smoothing, blue line: $ks = 5$ smoothing iterations, red line: $ks = 10$ smoothing iterations, green line: $ks = 30$ smoothing iterations. Left panel: whole contour, right panel: zoom on a specific region.

The smoothing routine is based on a diffusive process. Images can display many small variations from one pixel to another, due, for example, to the presence of a particle, or any other perturbation on the laser beam. In order to smooth the data, a diffusive filter is applied of the form $data(x, y) = 0.5data(x, y) + 0.25(data(x - 1, y) + data(x + 1, y))$ as equally applied to the y direction. Different numbers of iterations k_s of this diffusive process were tested. Figure 4.5 exhibits contours obtained from experiment 1 at time $t = 405$s for the contour level $l = 32882$ for different smoothing treatments. The black line corresponds to no smoothing, the blue line to $k_s = 5$ iterations, the red line to $k_s = 10$ iterations, and the green line to $k_s = 30$ iterations. The left panel shows the whole contour while the right panel zooms into the waves with the wavelengths of greatest interest. We can see that the smoothing process represented by the black line captures very small scales. These small scales are in part due to very small fluctuations from one pixel to another. Typically, at the rim of the tank where the laser enters it, small perturbations such as bubbles can create small waves on the contours. Conversely, the smoothing process represented by the green line largely inhibits the waves we are

interested in. The interesting waves are captured best using $k_s = 5$ to $k_s = 10$ smoothing iterations.

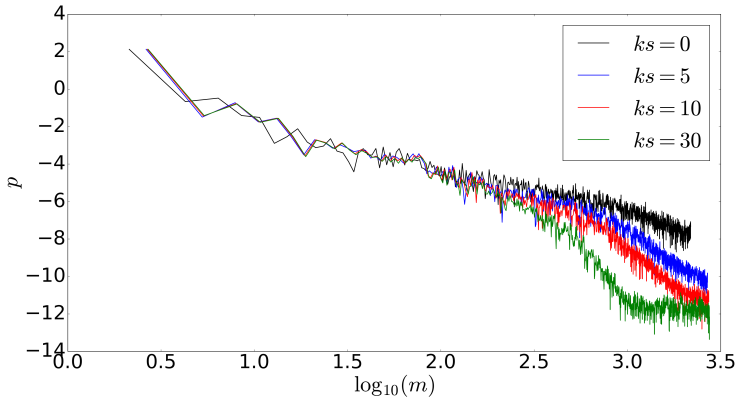

Figure 4.6: Log profile of the power spectrum around a level contour equal to 32884, at time 150s, for various smoothing iterations. Black line: no smoothing, blue line: $k_s = 5$ iterations, red line: $k_s = 10$ smoothing iterations, green line: $k_s = 30$ smoothing iterations.

Figure 4.6 shows the logarithm power spectrum of a light level contour equal to $l = 32882$ at time 105s for different smoothing iterations, for experiment 1. Note that for small wavenumbers, the results are very similar for most of the different numbers of smoothing iterations. For higher wavenumbers however, the smoothing acts as a low-pass filter. The more we iterate the smoothing process, the more we damp the high wavenumbers. In the following analyses, we chose to use $k_s = 10$ iterations (red line). For k_s smaller than five, the contour exhibits too many fluctuations. We chose ten iterations rather than five, as this results in a clearer profile.

To find the relevant light level which will capture the front, we plot the area covered by this level in the image (i.e. a probability density function not scaled between 0 and 1). Figure 4.7 shows the area covered by each level. The interface is characterised by a region of a high positive gradient of the area covered by each contour. The first high positive gradient corresponds to the centre of the tank, while the most interesting contour levels are found in the second and third high positive gradients.

This method yields a precise spectrum of the wavenumbers around a specific contour. However, as the contour's size changes with time, so too do the wavenumbers. This method is, therefore, used mainly for single images rather than time evolutions.

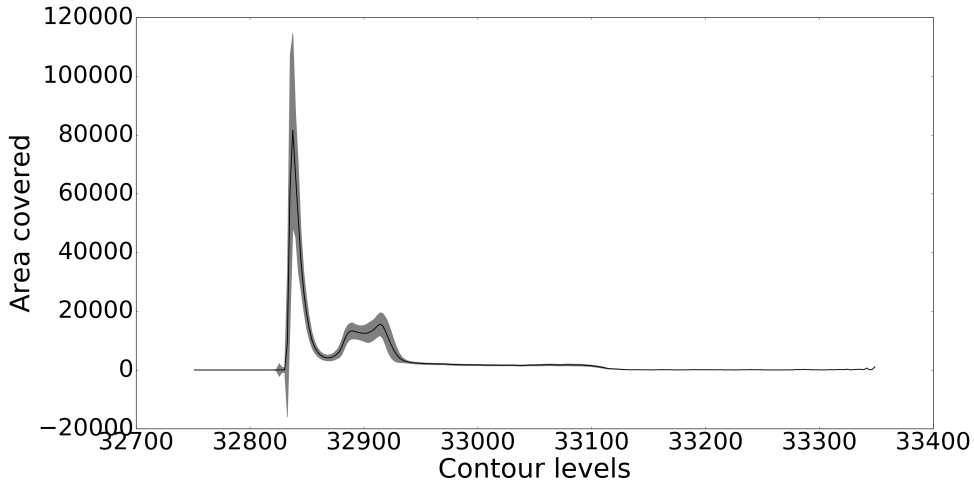

Figure 4.7: Area covered by each light level compared with light intensity levels. The black line exhibits the time averaged area covered by each level over 9000 images and the grey regions exhibit the time averaged area minus the area covered by each level variance over 9000 images.

4.3.3 Radially averaged analysis

Using light intensity around a circle does not capture waves outside the circle, so if we have small wavenumber perturbations, a lot of information may be missed using this approach. With the contour method, we obtain a precise contour for a single image. As stated above, however, the variation in contour length over time makes it impossible to simultaneously follow the time evolution. We developed another method based on radial integration. First, we smooth the image to delete the small light aberrations, as we did in the contour method, before interpolating the image to polar coordinates. We then radially integrate the light intensity by applying the following function: $\int_{r=0}^{R} data(r,\theta) r dr / \int_{r=0}^{R} r dr$. We can apply this function by assuming that waves mainly propagate azimuthally, not radially. The left panel in figure 4.8 displays the signal obtained in the first experiments after applying the routine between times $t = 350$s and $t = 450$s. Next, we apply a 2D fft to the signal which depends on θ and time and obtain an array with frequencies and azimuthal wavenumbers.

The right panel in figure 4.8 exhibits a phase diagram with azimuthal wavenumbers on the abscissa and frequencies on the ordinates. We can see a clear pattern of several linear profiles. The blue line corresponds to the dispersion relation of surface gravity waves, linearly varying as $\sqrt{g'h}$. The two dashed lines are a large estimation of the error on the computation of the dispersion relation. The dispersion relation of inertia-gravity

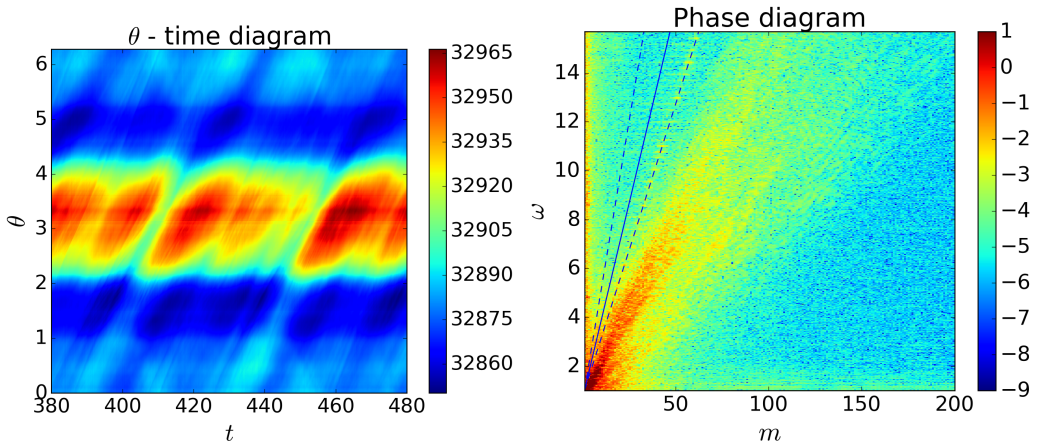

Figure 4.8: Left panel: time evolution of the radially-averaged azimuthal light intensity. Right panel: logarithm of the phase diagram for frequency versus azimuthal wavenumber.

waves is $\omega^2 = (f^2k^2 + N^2(l^2 + m^2))/(k^2 + l^2 + m^2)$ with the limit frequencies N and f. While the vertical and radial wavenumbers (k and l) are not known, we expect the slope of the dispersion relation to be lower for inertia-gravity waves, and indeed this is consistent with the observed signal (red area in figure 4.8). This indicates the presence of inertia-gravity waves that propagate between half and a quarter of the speed of the disk. The origin of the waves could be Kelvin-Helmholtz or Holmboe, as well as spontaneously emitted inertial-gravity waves as was also confirmed by Scolan et al. [2014], who showed the waves in space set by Richardson – wave number. Note that the less steep dashed blue line also corresponds to the rotation of the rigid lid. To find the mean radius where these patterns are observed, we computed the mean radius over a contour obtained from the contour method. Although it is biased by the choice of the light intensity level, it does give a first approximation of the localisation of these waves.

4.3.4 Density derivative

By subtracting two consecutive LIF images, we obtain information about the temporal evolution of the density (as the density can be directly related to light intensity) and on the divergence of the density times the velocity by mass conservation. To improve the signal, we apply the same diffusive smoothing process after the subtraction. From this signal, we apply a two-dimensional Fourier transform. To obtain the power spectrum, we average the power (squared amplitude) over concentric shells in wavenumber space, centered on $m = \sqrt{k_x^2 + k_y^2} =$ constant. In this way, we capture both the wavelength in

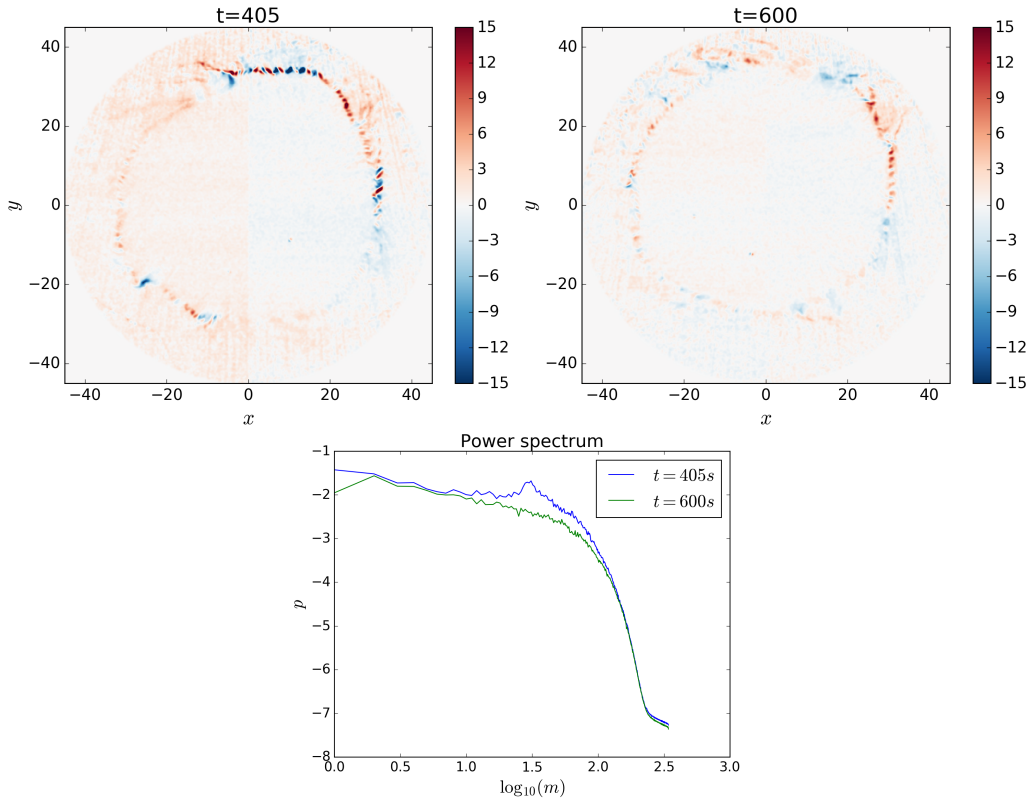

Figure 4.9: Top panel: subtraction of two images for time $t = 405$s on the left panel and $t = 600$s on the right panel. Bottom panel: $\log_{10}$ of the power spectrum versus $\log_{10}$ of wavenumbers m.

the direction of propagation as well as the width of the waves in the orthogonal direction. Figure 4.9 shows this method applied at two different times: at $t = 405$s on the top left panel and at $t = 600$s on the top right panel. The bottom panel shows the power spectrum versus the $\log_{10}$ of wavenumbers. Waves are clearly visible on the top left panel, but absent or very weak at time $t = 600$s. This difference in wave activity matches the power spectrum variations between these two times.

This method focuses on the derivative of the density with time. We tried different derivative schemes by subtracting one image from the consecutive image or using order three and five schemes. Figure 4.10 shows the signal for two different derivative schemes. The left panel shows the first order derivative scheme $(f(t) - f(t - \delta t))/\delta t$, while the right panel shows the fifth order derivative scheme $(2(f(t + \delta t) - f(t - \delta t)) + f(t + 2\delta t) - f(t - 2\delta t))/8\delta t$. The fifth order derivative scheme tends to smooth the signal over time and, diminish some waves that could be of interest to our study. We will, therefore, use the first order derivative scheme in this study.

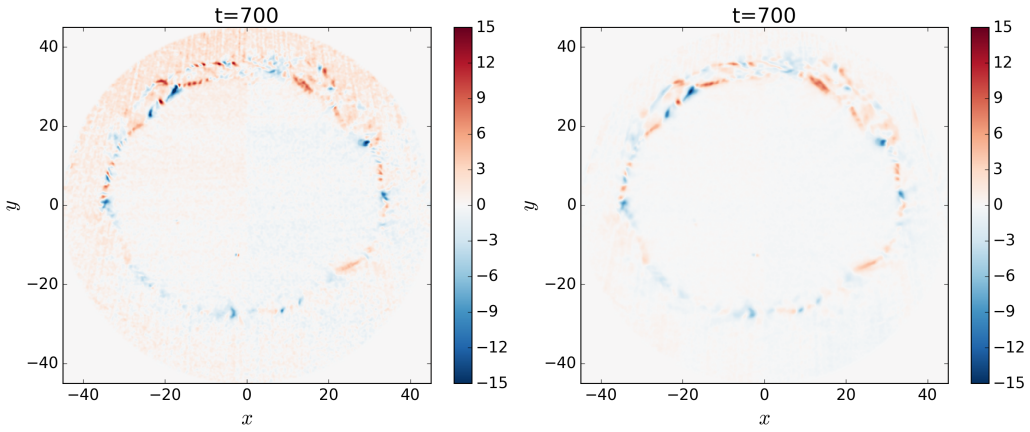

Figure 4.10: Left panel: image after applying a first order derivative temporal scheme. Right panel: image after applying a fifth order derivative temporal scheme, both at time $t = 700$s.

4.3.5 Particle image velocimetry

To analyse the particle images, we use the PIV method with the software UVmat developed with Matlab by Joël Sommeria. From the particle images, we obtain the velocity field. This then allows us to extract information about the vorticity and divergence of the flow field. The PIV is computed between images separated by a time step, which is here 0.2 seconds.

4.4 Results

In this section, we analyse two experiments which have the same parameters except for the Rossby number, which is equal to $Ro = 0.405$ for experiment 1 and $Ro = 0.572$ for experiment 2. Different phenomena are visible in the two experiments: whereas experiment 1 exhibits baroclinic vortices preceded by small waves, experiment 2 reveals large-scale barotropic vortices emerging from the flow. We look at the impact of small waves on the formation of vortices, at the different ways in which vortices form in the two experiments, the typical recovery period, mixing, and at the overall impact of the Rossby number on amplitude vacillations. Section §4.4.1 presents the evolution of the flow in experiment 1 and section §4.4.2 presents the evolution of the flow in experiment 2.

Here, since the mean flow moves anti-clockwise, upstream and downstream mean in a clockwise and anti-clockwise direction, respectively. Positions are characterised by their

angle in a classic trigonometry reference, with the centre located at the centre of the tank, as in figure 4.2.

4.4.1 Experiment 1

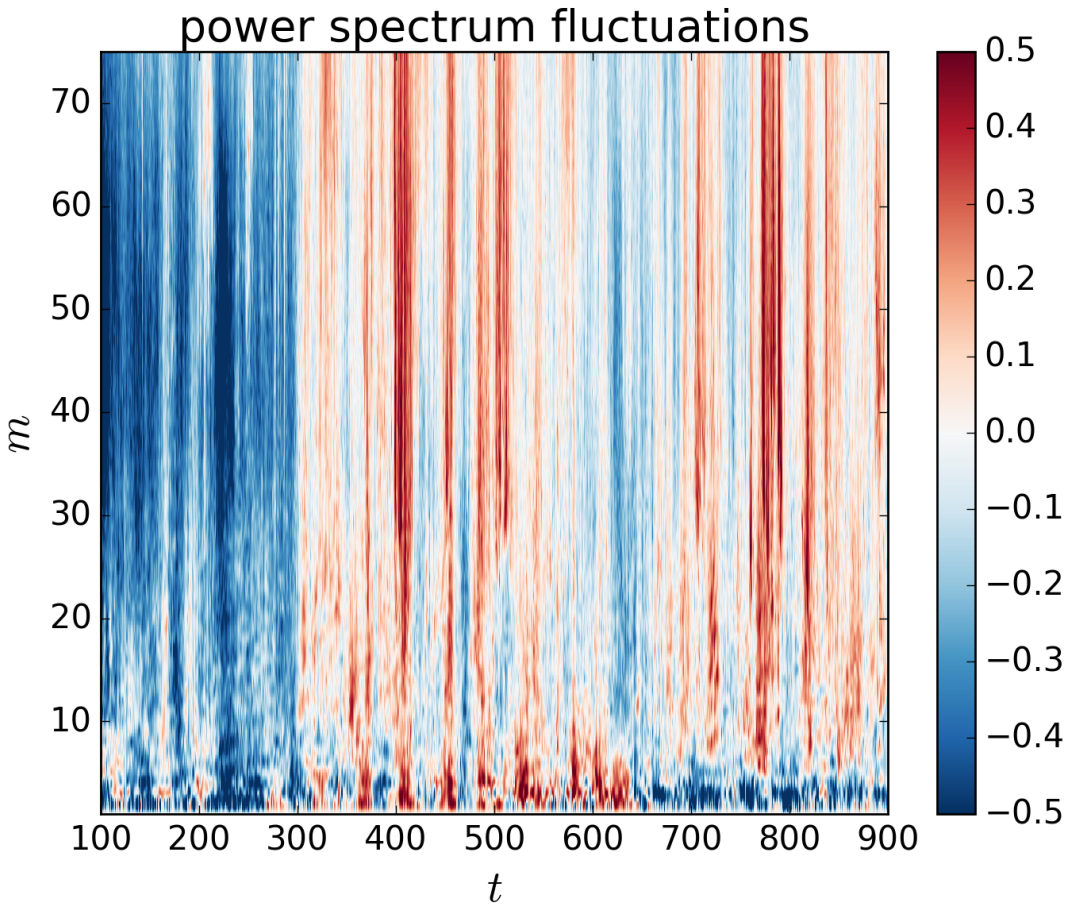

Figure 4.11: Power spectrum fluctuations of experiment 1, obtained using the density derivative method, between times $t = 100$s and $t = 900$s, with azimuthal wavenumber in ordinates and time in abscissa.

Experiment 1 has been conducted over 1000s. It has a Burger number of $Bu = 0.120$ and a Rossby number of $Ro = 0.405$. We start recording when the flow is already in solid body rotation. Figure 4.11 shows the power spectrum fluctuations between times $t = 100$s and $t = 900$s, with azimuthal wavenumbers along the ordinates and time along the abscissa. The power spectrum fluctuations are obtained from the density derivative method presented in section §4.3.4. Until time $t = 300$s, the flow is quite steady, with only a small number of visible perturbations. Between times $t = 300$s and $t = 520$s,

many azimuthal wavenumbers are excited. First, we will present the main characteristics of the flow during this period. Next, we will focus on the formation and evolution of a dipole. Finally, we present the main characteristics of the flow during the recovery phase, between $t = 700$s to $t = 820$s.

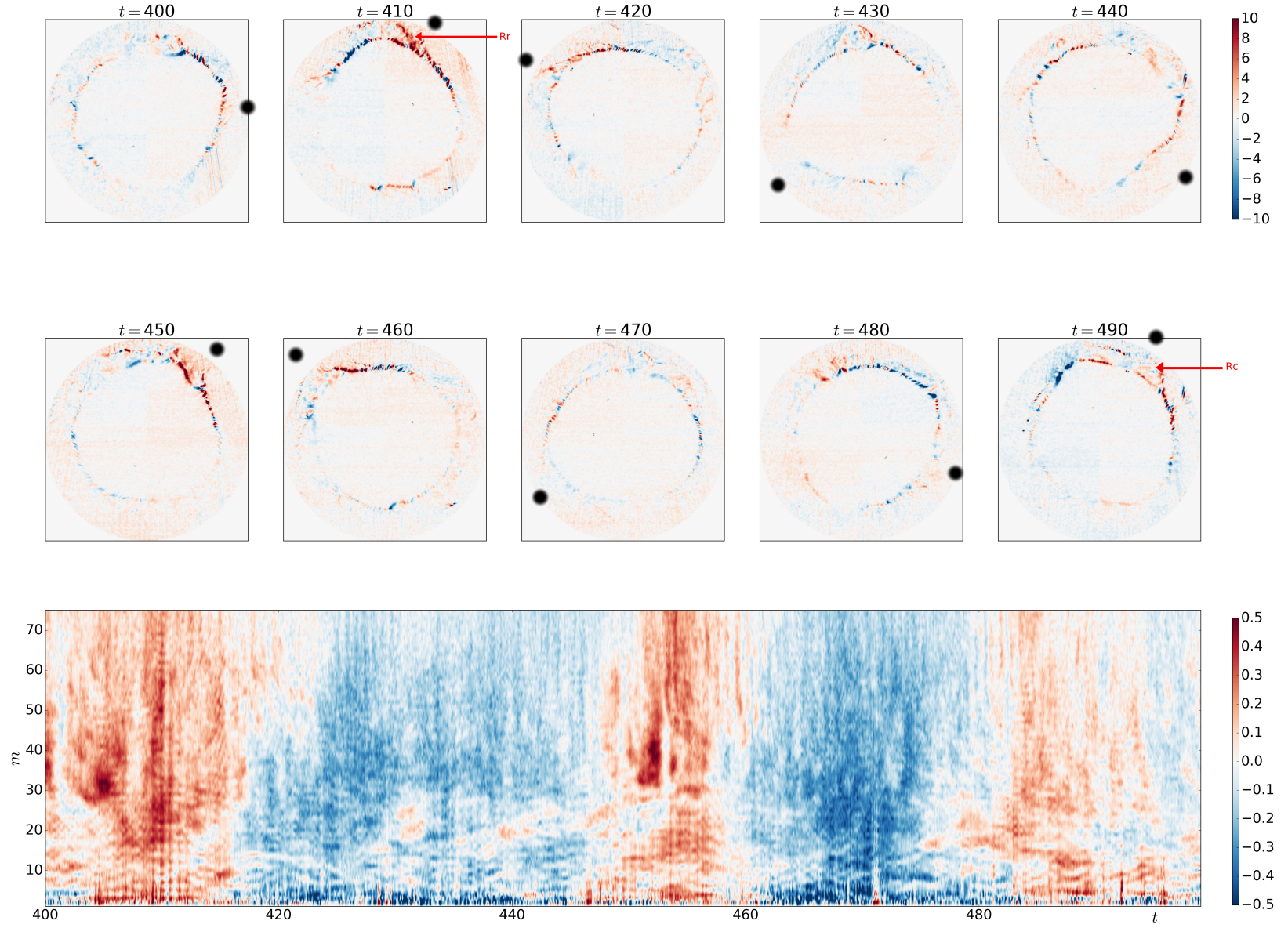

Figure 4.12: Top and middle panels: time sequence of the front from LIF images processed as in section §4.3.3. The black dot represents the region where the futur vortex will develop, and it gives a point of reference to follow the evolution of the flow. Bottom panel: power spectrum fluctuations of experiment 1, obtained using the density derivative method, between times $t = 400$s and $t = 500$s. The azimuthal wavenumbers are represented at the ordinate and time in the abscissa.

Figure 4.12 shows a Hövmoller diagram of the power spectrum fluctuations between approximately $t = 400$s and $t = 500$s, in the bottom panel and ten snapshots of the flow using the density derivative method. These snapshots allow us to follow the evolution of the flow and to see wave activity and vortex precursors. As seen in the central diagram, a large number of wavenumbers are excited during the first twenty seconds, followed by a more quiescent phase between approximately $t = 420$s and $t = 445$s. Next, a new active phase appears between approximately $t = 445$ and $t = 460$s, followed by another quiescent phase between $t = 460$s and $t = 480$s, which in turn precedes another active phase.

To enable us to follow the flow evolution, a black dot gives a point of reference in the top and middle panels in figure 4.12. The region marked by the black dot is particularly interesting as it is from this region that the first vortex will form. A clear front is visible at $t = 400$s at $\pi/3$, and at $t = 410$s at $\pi/2$. Small waves upstream of this front are visible (between $\pi/3$ and $\pi/6$ at $t = 400$s). To study the flow in between these times, figure 4.13 shows different analyses performed at $t = 405$s: the top left panel shows the LIF image, the top right panel shows an image obtained from the density derivative method, the bottom left panel shows the particle image, and the bottom right panel shows the vertical vorticity field. Around $\pi/2$, a sharp front is visible, with small-scale waves upstream. Around the angle $\pi/4$, the vertical vorticity field exhibits a larger-scale perturbation. This is the seed of the future vortex. Upstream of this large-scale perturbation, small-scale waves are visible. Small waves upstream of a vorticity anomaly are a recurring pattern in this experiment.

At $t = 410$s, azimuthal wavenumber three is excited, giving the flow a droplet shape with a pointed top and small waves on its flanks. Additional mixing occurs, characterised by a continuous red spot (region R_r in figure 4.12) at an angle between $\pi/3$ and $\pi/2$ (other parts of the flow are barely visible at this time). This active region is less visible at $t = 420$s and $t = 430$s, before being visible again between $t = 440$s and $t = 460$s, again barely visible between $t = 470$s and $t = 480$s, before finally reappearing at $t = 490$s. These oscillations match the oscillations visible in the central diagram. The fluctuations of the power spectrum are qualitatively comparable between times $t = 400 - 420$s, $t = 445 - 460$s, and $t = 480 - 500$s, where we have a high wave activity. Similarly, quiescent phases are also qualitatively comparable. It is unclear if these oscillations between quiescent and active phases are due to oscillations in wave activity or the rotation of the mean flow (and so the rotation of active regions) linked to the attenuation of light

on one side of the tank. The signal is clearer at the top than the bottom of the image due to the unavoidable light attenuation caused by rhodamine (the laser beam enters at the top of the image). But we can at least say that quiescent and active phases are correlated with the mean flow.

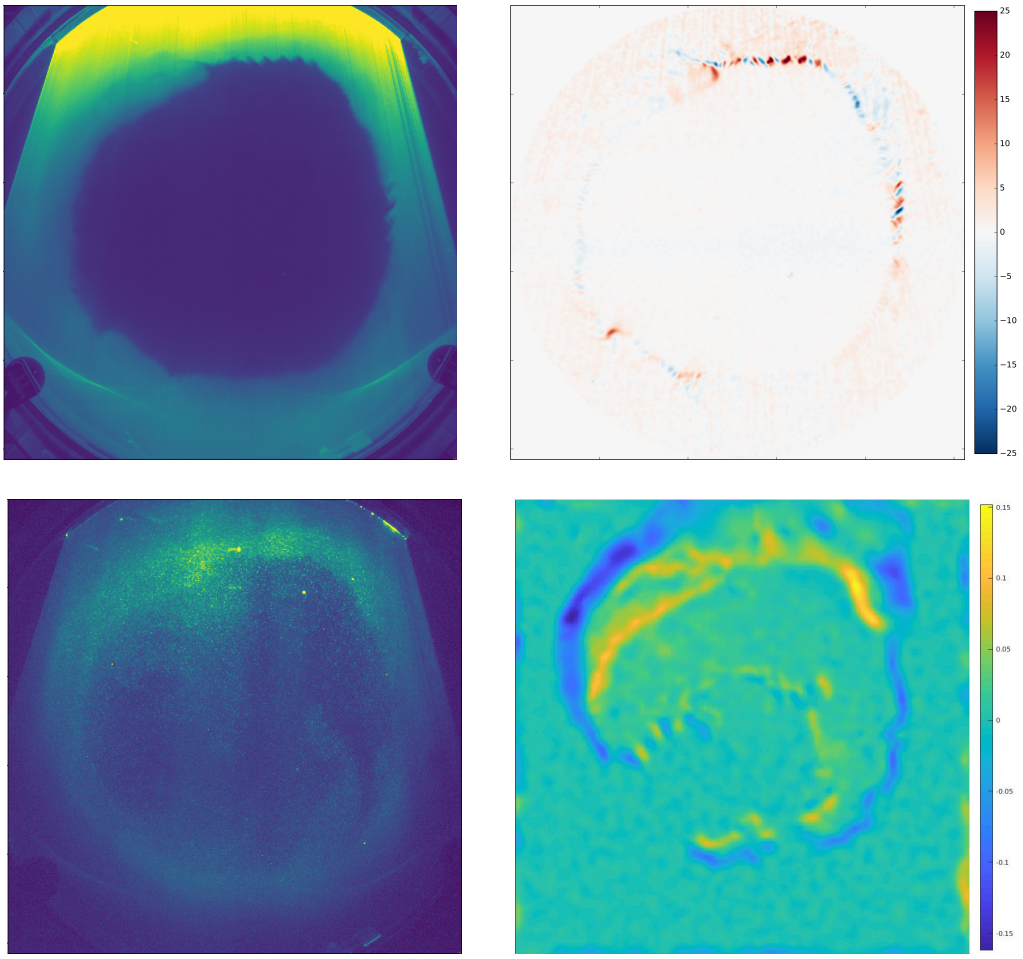

Figure 4.13: Top left panel: LIF image. Top right panel: image obtained with the derivative method. Bottom left panel: particle image. Bottom right panel: vertical vorticity field. All these images are taken at time $t = 405$s.

At $t = 490$s, a peculiar pattern is visible between $\pi/3$ and $\pi/2$: two lines of waves are visible for the same azimuthal position. This phenomenon is also vaguely visible at other times, such as $t = 450$s or $t = 470$s. At $t = 490$s, the outside part exhibits more wave patterns than the inner side, which shows an almost continuous line. These two lines are not two separated and unrelated lines but rather the contour of a common region. This contour encloses a region R_c where mixing between the two layers has occurred. The interface has a certain thickness characterised by a transition in density. Jumps in density

occur at the limits of the interface and are recognised as fronts. This region is of interest to us as its evolution will lead to the formation of the first vortex. In other words, the vortex is formed from regions of high wave activity. The following section will present its appearance and its evolution.

Baroclinic vortices

Figure 4.15 displays in the top and middle panels ten snapshots obtained using the density derivative method between times $t = 500$s and $t = 600$s, and a Hövmoller diagram in the bottom panel showing the time evolution of azimuthal wavenumbers obtained from the density derivative method.

In the previous section, we introduced a region R_c defined by a contour visible at time $t = 490$s. This region is still visible at time $t = 500$s, and barely visible but present at time $t = 510$s. Later, at time $t = 520$s, a vortex starts to form between $-\pi/3$ and 0 that it is characterised by the intrusion of the region R_c in the lower layer.

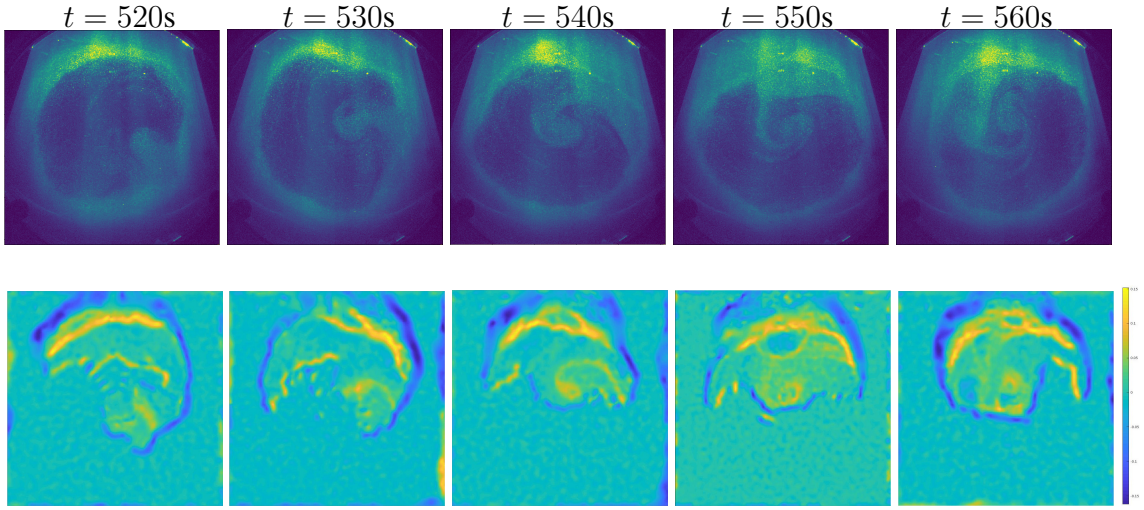

Figure 4.14: Top panel: particle images. Bottom panel: vertical vorticity field.

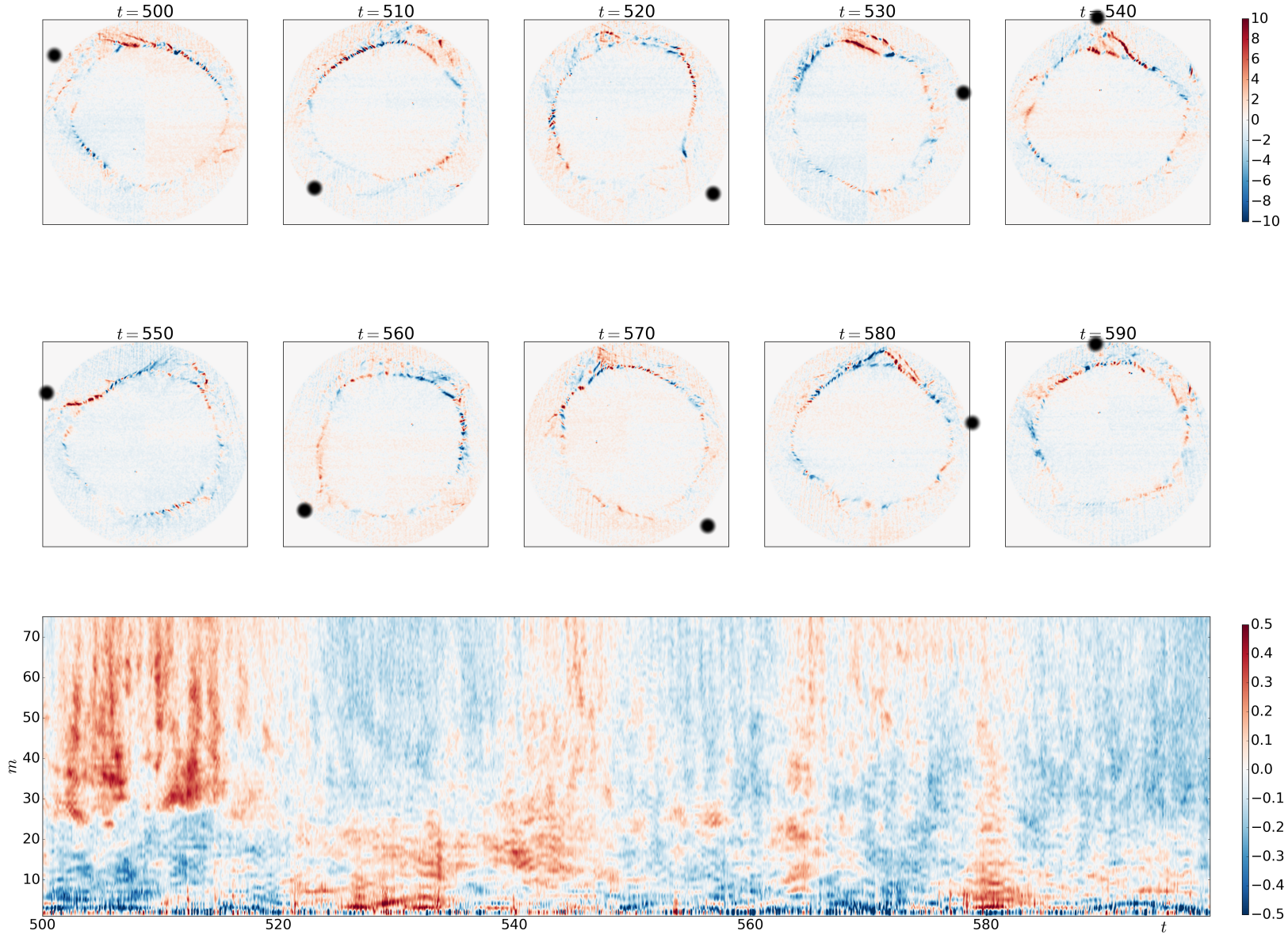

Figure 4.15: Top and central panels: time sequence of the front from LIF images processed as in section §4.3.3. The black dot represents the region where the first vortex develops, and it gives a point of reference to follow the evolution of the flow. Bottom panel: power spectrum fluctuations of experiment 1, obtained using the density derivative method, between times $t = 500$s and $t = 600$s. The azimuthal wavenumbers are represented at the ordinate and time in the abscissa.

Figure 4.14 shows particle images on the top panels and the vertical vorticity field on the bottom panels for five different times during the formation of a vortex. At time $t = 520$s, a vortex emerges from the front. It is visible on the vorticity image at an angle of $-\pi/6$. Later, the vortex develops, as seen over the subsequent times. When the vortex's size increases, it centres and slows down, since the lower layer has a lower velocity than the front. On the vorticity images, we can see the development of the vortex and the emergence of a second vortex close to the front. While the first vortex is a cyclone with a positive vorticity (yellow spot), the second one is an anti-cyclone with a negative vorticity (blue spot). These two vortices, which form a dipole, centre and dissipate (see Thysen [2014]).

The vortices come from the front of the flow, from a region where mixing occurred and then moved toward the centre. The vortex is visible on the vorticity field and particle images, but barely visible on the LIF images. Since the dye is in the upper layer and the particles are everywhere, this means that there are no, or only few, intrusions from the top into the bottom layer. Vortices, then, only add to the large-scale mixing to a limited extent, as we will see in experiment 2 (see section §4.4.2). Moreover, vortices are only visible in the lower layer. Additionally, the radius of each vortex is comparable to the Rossby deformation radius defined by $L_d = \sqrt{g'H_1}/f$. We therefore have vortices with components in the barotropic and baroclinic modes in this experiment.

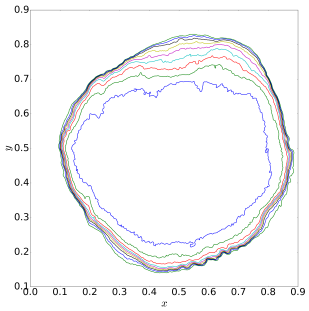

Figure 4.16: Contours at time $t = 550$s, for nine contours between $l = 32840$ and $l = 32880$, separated from one another by five light levels.

Figure 4.16 shows different contour levels at time $t = 550$s. We can see on the upper part that the contours are more spread than in the other parts. This upper region corresponds to the area where the anticyclones settle, i.e., vortices contribute to a small extent to the mixing between the two layers.

Recovery Phase

Later, around time $t = 650$s, another cyclone appears, soon followed by another vortex. The two form a dipole, centre and then dissipate with the flow.

The recovery phase begins when the second dipole starts to centre. During this phase, the vortices first centre and the small waves on the front disappear, before the vortices slowly dissipate with the flow. After that, small waves start reappearing. This recovery phase starts at around $t = 700$s and lasts until $t = 820$s, when a new vortex forms and the process repeats, as being part of the process of amplitude vacillation.

4.4.2 Experiment 2

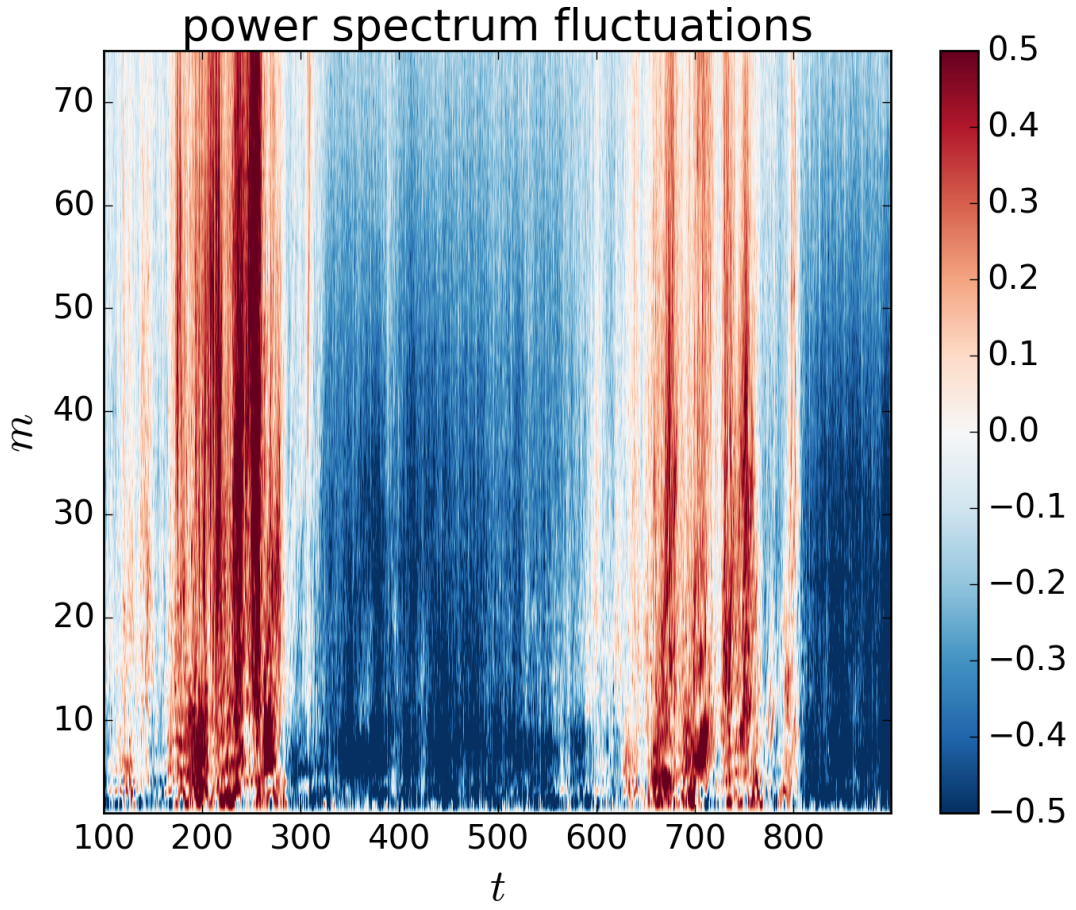

Figure 4.17: Power spectrum fluctuations of experiment 2, obtained using the density derivative method, between times $t = 100$s and $t = 900$s, with azimuthal wavenumber in the ordinates and time in the abscissa.

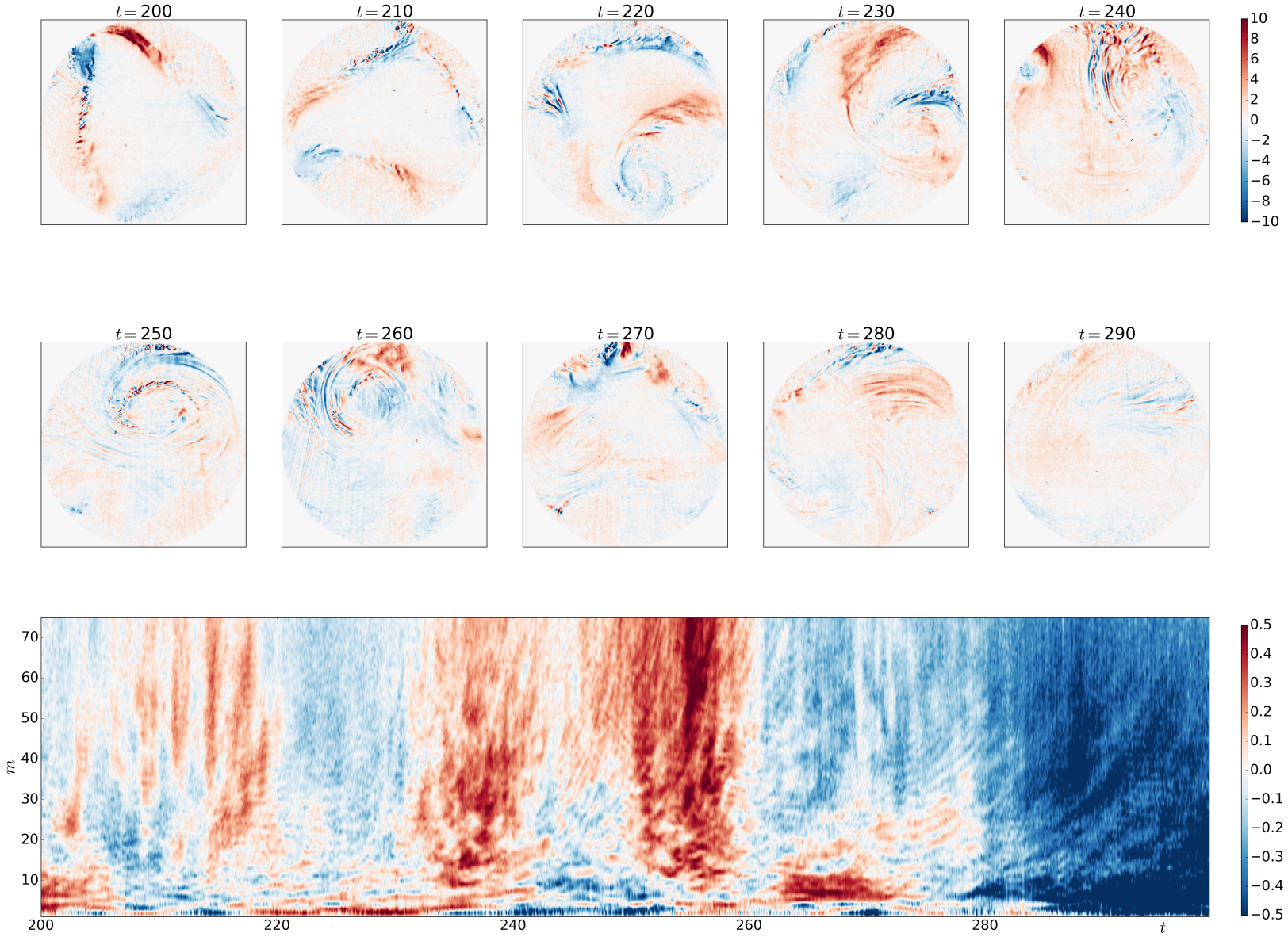

Figure 4.18: Top and central panels: time sequence of the front from LIF images processed as in section §4.3.3. Bottom panel: power spectrum fluctuations of experiment 2, obtained using the density derivative method, between times $t = 200$s and $t = 300$s. The azimuthal wavenumbers are represented at the ordinate and time in the abscissa.

Experiment 2 was conducted over 1000s. It has the same Burger number as experiment 1, $Bu = 0.120$, and a Rossby number of $Ro = 0.572$. As in experiment 1, the records begin when the flow starts to be in solid body rotation.

Figure 4.17 illustrates the power spectrum fluctuations between times $t = 100$s and $t = 900$s obtained using the density derivative method. A first vortex emerges around time $t = 180$s and centres around time $t = 300$s. A quiescent phase follows where the vortex dissipates into the flow. The merging of the flow between times $t = 300$s and $t = 450$s contributes to the mixing. This mixing is responsible for a flattening of the interface between the two layers. It is characterised by a shrinking of the front at this height, visible around time $t = 450$s. Then, between $t = 450$s and $t = 650$s, the vertical shear imposed by the rigid lid again increases the slope of the interface. At time $t = 650$s, a second vortex starts to form until its final centring around time $t = 800$s. As before, the interface is flatter and slowly recovers its vertical shear.

Although the power spectrum fluctuations look qualitatively comparable to experiment 1, they are different. First, positive fluctuations appear while the vortex is forming rather than appearing as a precursor of the vortex. Fluctuations present at different scales in experiment 2 are a signature of mixing, whereas in experiment 1, they are a signature of waves propagating. Vortices in experiment 2 arise from small wavenumber perturbations; typically, wavenumber three in this case. Figure 4.18 shows ten images of the flow using the density derivative method, between times $t = 200$s and $t = 300$s. The bottom panel shows the power spectrum fluctuations between the same times obtained from the density derivative method. At time $t = 200$s, the excitation of wavenumber three is clearly visible, with one of the corners already more dynamic (the upper corner, called C_1), and small waves forming upstream on the flank of the front. At time $t = 220$s, the breaking of corner C_1 is visible, forming a vortex. This vortex is visible in the subsequent times, where it further soon centres. In contrast to experiment 1, the vortex radius is about two times larger and completely dominates the entire flow. This suggests a barotropic vortex that extends uniformly over the entire depth and mixes the fluid at the interface. The radius of the vortex is comparable to the Rossby radius of deformation defined by $L_d = \sqrt{g'H}/f$ with $H = H_1 + H_2$.

Figure 4.19 shows three contours for the same light intensity at three different times. The blue line shows the contour when the vortex has finished to dissipate into the flow, at time $t = 400$s, when the interface is at its flattest. The other two contours show the flow at time $t = 500$s (green line) and $t = 600$s (red line). We can see the contour area

increasing with time, corresponding to the recovery period of the flow, when the vertical shear imposed by the rigid lid sharpens the interface.

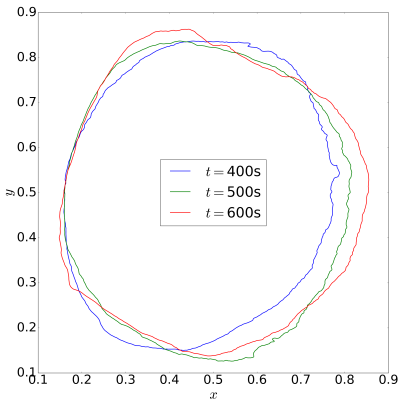

Figure 4.19: Contours for a light intensity of $l = 32880$ at times $t = 400$s, $t = 500$s and $t = 600$s, for experiment 2.

In experiment 2, then, we have barotropic vortices which emerge from small wavenumber perturbations and contribute to the mixing between the two layers. Small-scale waves are visible in the bottom panel in figure 4.18, but they are not predominant as in experiment 1.

4.5 Conclusion

In this chapter, we have analysed two experiments conducted by JH Thysen in 2014 to understand the formation of waves and vortices. To do so, different analysis methods have been used: a method to find the contour and obtain the wavenumbers from it, a method based on the interpolation of the signal into polar coordinates followed by a radial integration yielding a phase diagram, and a method based on the derivative of the density field, which reveals the waves and PIV using the software UVmat.

Using these methods, we have been able to analyse the two experiments. While both have the same Burger number, they differ in their Rossby numbers and behaviours. In both cases, amplitude vacillations are present, vortices emerge from the flow, before centring, merging into the mean flow and thus stabilising it. This is followed by the formation of a new vortex, and the process repeats. However, amplitude vacillations are strongly different for the two Rossby numbers. In experiment 1 ($Ro = 0.405$) baroclinic dipoles form following small inertial-gravity wave activity. Vortex radii are comparable to the Rossby

radius of deformation using the lower layer height H_1. These vortices contribute to the mixing between the two layers only to a limited extent. In experiment 2, on the other hand ($Ro = 0.572$), only barotropic vortices form. They play an important role in the mixing between the two layers. Their radius is comparable to the Rossby deformation radius defined with the total height $H = H_1 + H_2$. Carton [2010] presented different vortices: a baroclinic vortex present in the thermocline and a barotropic vortex which extends further down. Their radii also vary depending on their vertical extension. Additionally, the recovery period of the amplitude vacillation differs between the two experiments, being around 120s for experiment 1 and around 200s for experiment 2. It follows that amplitude vacillations strongly depend on Rossby number: the recovery period is much longer and the mixing is more important for higher Rossby numbers. Furthermore, the nature of the resulting vortices is different; baroclinic dipoles versus barotropic vortices, and their origins also differ considerably, baroclinic vortices emerging from high wavenumber activity while barotropic vortices emerge from small wavenumber perturbations.

More research on the small waves' nature and the way energy is transferred from these waves to vortices is needed. Hilbert transform could be applied to the LIF measurements, though as the information is very localised in space, it has a broad range in the spectral space, making it potentially difficult to draw clear conclusions from results. Experiments with Rossby numbers between $Ro = 0.405$ and $Ro = 0.572$ for the same Burger number should be conducted to see if the transition between baroclinic dipoles to barotropic vortices is continuous or more abrupt, and to determine for which Rossby number it takes place.

To obtain more general information, we have developed a new optical method to detect the height of the entire profile. We plan to use this method on a two-layer immiscible fluids configuration. This apparatus and method will offer precise data over a long period and could reveal unknown behaviours. The following chapter presents this optical method.

Chapter 5

An optical method for measuring the interface height of two-layer immiscible fluids.

5.1 Introduction

A precise method able to detect small perturbations and large-scale dynamics is essential to analyse laboratory experiments. Currently, various methods are used to detect the two-dimensional motion of a fluid surface, such as synthetic Schlieren, Altimetry Image Velocimetry (AIV), Particle Image Velocimetry (PIV), Laser-Induced Fluorescence (LIF), polarimetry and dye intensity variations. Cox [1958] developed a method to obtain a one-dimensional slope using collimated light beams. Jähne et al. [1994], Zhang et al. [1996] extended his work to a two-dimensional slope. Dabiri and Gharib [2001] developed a non-intrusive colour-based method to detect the perturbation of a free surface, which combines the PIV method and optical laws of reflection. Rhines et al. [2007] developed another non-intrusive method using the reflection of a black and white pattern with the PIV method to detect the interface perturbations. Afanasyev et al. [2009] combined the method developed by Dabiri and Gharib [2001] and Rhines et al. [2007] to detect the elevation of a free surface in a rotating tank. For this method, a colour pattern is used that consists of red, green and blue gradients, are all shifted one from the other by $2\pi/3$, to give a unique colour to each point. The free surface of a rotating tank has a parabolic shape, plus perturbations due to, for example, forcing or instabilities. This

pattern is projected at the surface of the rotating fluid, which has a parabolic shape and is detected by a camera placed above near the centre of the rotation axes. By comparing the observed colour profile (with perturbations) with the initial profile (purely parabolic), the inclination of the free surface is obtained and the variation in height deduced. Supposing a quasi-geostrophic flow, the velocity field in the layer can be derived. By using a high definition image and camera, with this method one is able to obtain a very high spatial resolution of the slope of the free surface.

Another optical method for different layers of fluids is based on the detection of perturbations of the profile compared with an initial profile. This is the pseudo-Schlieren method. A pattern of random dots placed below the fluid at the bottom of the tank is deformed due to perturbations of the fluid surface. Using a digital image correlation algorithm the velocity field can then be obtained. This method is based on the pioneering work of Kurata et al. [1990], next applied to geophysical problems by Sutherland et al. [1999], Dalziel et al. [2000], and finally developed by Moisy et al. [2009]. However, this method can only be applied to flows with weak deformations and weak slopes of the surface of the fluid.

The aim of the research presented in this chapter is to find the height and slope of the *interface* between two layers of fluid in a rotating tank with a rigid rotating lid on top. As seen in chapter 4, the LIF and PIV methods have limitations, such as the difficulty of capturing the entire profile of the interface due to the concentration of particles at the interface. Information about the slope and height can be acquired for the surface of a single layer of fluid with the synthetic Schlieren method provided that these slopes are small. We are, however, interested in flows with slopes bigger than those tolerated by this method. In view of safety constraints at the LEGI we have chosen to use silicone oil instead of limonene. This is because limonene is more flammable, but this means we cannot use the polarimetry method. Our method is inspired by the AIV method which gives very high spatial resolution slopes of the free surface, using reflection laws. Here, we want to investigate the interface between two layers of fluid of different refraction index, so that we can use the refraction laws to calculate the motion of the interface (see Afanasyev et al. [2009]). Thus, we have developed a method to detect the height and the slope of an interface between two layers of fluids with a rigid lid at the surface.

In section §5.2 we describe the apparatus. Next, equations to find the height and the slope of the interface are presented in section §5.3. Section §5.4 details the numerical implementation. Then, the different configurations used to test the code are discussed

in section §5.5. Finally, section §5.6 concludes this chapter and examines the different possibilities of improvement for this method.

5.2 Experimental setup

5.2.1 Apparatus

Let us first introduce the flow and experimental setup. The experimental setup is similar to the one presented in chapter 2. Instead of two fluid layers with different salt content to set the density difference, we use water for the lower layer and silicon oil for the upper layer. The relevant properties of the two fluids (density, viscosity and refractive index) are given in table 5.1. Also included are the properties of 1 centiStockes Silicon oil, which is more interesting because of its viscosity being equivalent to that of water. In view of the numerous safety precautions related to fast evaporation and an explosive nature, we focus here on the safer 2 centiStockes Silicon oil.

Fluid	ρ	ν	n
	kg L^{-1}	cSt=10^{-6}m^2 s^{-1}	
Water	1	1	1
Brine	1.2		1.383
Ethanol 95%	0.78		1.41
Silicon oil 1cSt	0.816	1	1.3874
Silicon oil 2cSt	0.872	2	1.3904

Table 5.1: Density ρ, cinematic viscosity ν and optical index n of fluids.

If the lower layer is plain water, we have $g' = 134$cm s^{-2}. From the value of the reduced gravity, we can compute the Burger number, assuming $H = 15$cm, $R = 65$cm and $\Omega = 0.7$rad s^{-1}, we have $Bu = 0.24$. Silicon oil is immiscible with water and also with other fluids that are miscible with water, such as alcohol or salty water. The density of the lower layer can be increased or decreased by adding salt or alcohol to water, respectively. Brine density is around $\rho = 1.20$kg L^{-1}, so $g' = 2g(\rho_2 - \rho_1)/(\rho_2 + \rho_1) = 310$cm s^{-2}. With a solution of ethanol of 95%, the lower layer has a density of $\rho = 0.78$kg m^{-3}, by mixing 95% alcohol with plain water, we can reach $g' = 10$cm s^{-2} (note that adding salt or alcohol also changes the optical index of the fluid). The rotation speed can

vary from 0.1rad s^{-1} to π rad s^{-1} for a constant mean height of $H = 15$cm, the possible range of Burger numbers for this flow, using background rotation and density, goes from $Bu = 0.0009$ to $Bu = 27.5$, so that a wide range of Burger numbers can be investigated.

Immiscible fluids have several advantages but also some dynamical inconveniences. Since the fluids do not mix, an experiment may last forever. For a typical rotation of $\Omega = 0.7$rad s^{-1}, we can model a period of a year in a bit less than an hour. We could therefore simulate the evolution of a front for a period of nine years in a single day. PV is conserved and results may therefore be compared with two-layer shallow-water simulations, such as the Phillips model from Phillips [1951]. Mixing, however, is absent, so waves and instabilities due to a continuous variation of density will not be present or will exhibit a different behaviour.

As mentioned, we measure the refraction of light rays passing through the interface. To detect the different rays a colour pattern is used, illuminated by LEDs from below. A camera is placed at the top of the tank, at a height of $H_c = 210$cm from the bottom of the tank. Figure 5.2 shows a two-dimensional sketch of the apparatus. Because of the different refraction indices of the two fluids, interface perturbation will result in a change of direction of a light beam. Because of the colour pattern, each light ray has a different colour. With the laws of refractive optics one can then calculate the appropriate variation in interface height for each light beam. We implemented a virtual 30cm diameter tank, with $H_1 = 3.5$cm and $H_2 = 2.8$cm, with the camera placed at a height of $H_c = 210$cm from the bottom of the tank. The lower layer fluid has an optical index of $n_1 = 1.33$ and the upper layer has an optical index of $n_2 = 1.3787$.

Since this method allows us to measure the variations in height, one reference height, somewhere in the tank, for a ray of reference is also needed. A point on the edge of the tank would not be useful, for example, as no ray goes from the bottom of the tank to the edge up to the camera. So, a probe or any other method to obtain the height at one point in the field of view of the camera has to be used.

5.2.2 Colour profile

We use a colour profile based on that used by Afanasyev et al. [2009]. It is an rgb colour profile, with the intensity of each of the three colours, red, green and blue, linearly going from 0 to 1 with a rotating shift of $2\pi/3$ between each of them. Our profile differs from

the one chosen by Afanasyev et al. [2009], as each colour varies linearly in our case and not in theirs. We chose a linear profile as it simplifies the following equations, since the colour gradient can directly be related to the pixel gradient.

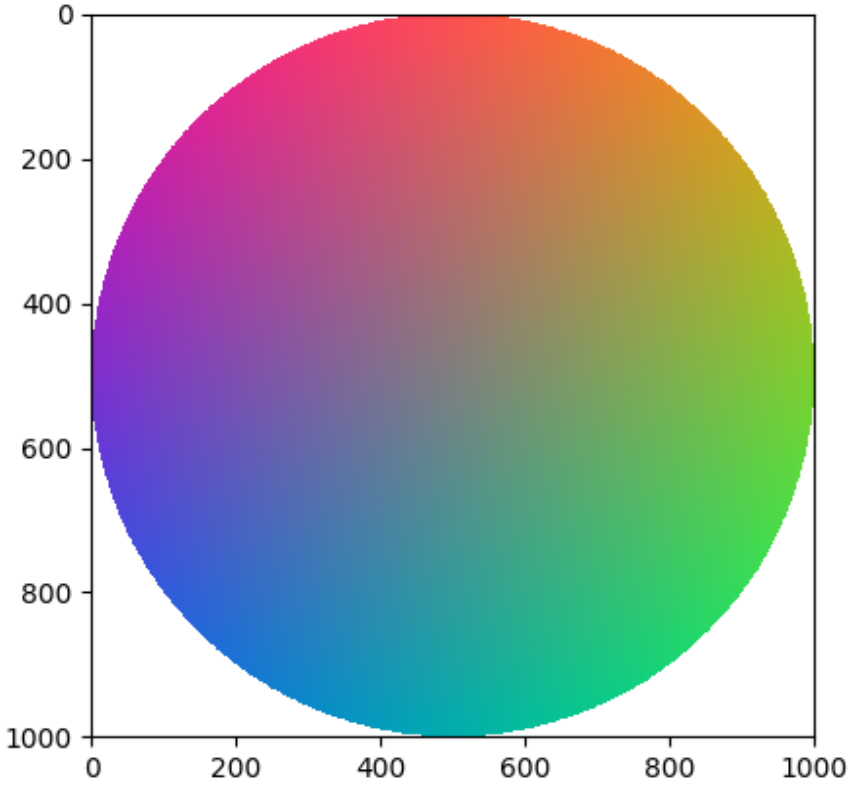

Figure 5.1: RGB colour profile.

5.3 Height and slope equations

In the following section, index 3 refers to the air, index 2 refers to the upper layer, index 1 refers to the lower layer, angles θ are computed between rays and the vertical vector $\vec{z}$, angles β are computed between rays and the normal at the middle interface, the symbol $\tilde{}$ is used for variables in the middle interface incident plane.

We consider a light ray coming from the colour profile at the point M_i. In the absence of fluid, this ray arrives at the camera with an angle θ_3 defined by $\cos(\theta_3) = H_c/\sqrt{x_i^2 + y_i^2 + H_c^2}$ with H_c representing the camera height. M_i can be written in the (x, y, z) coordinate system as $M_i = (x_i, y_i, 0)$, with x and y the coordinates of the colour profile and z the vertical coordinate. Figure 5.2 shows a two-dimensional sketch of a ray

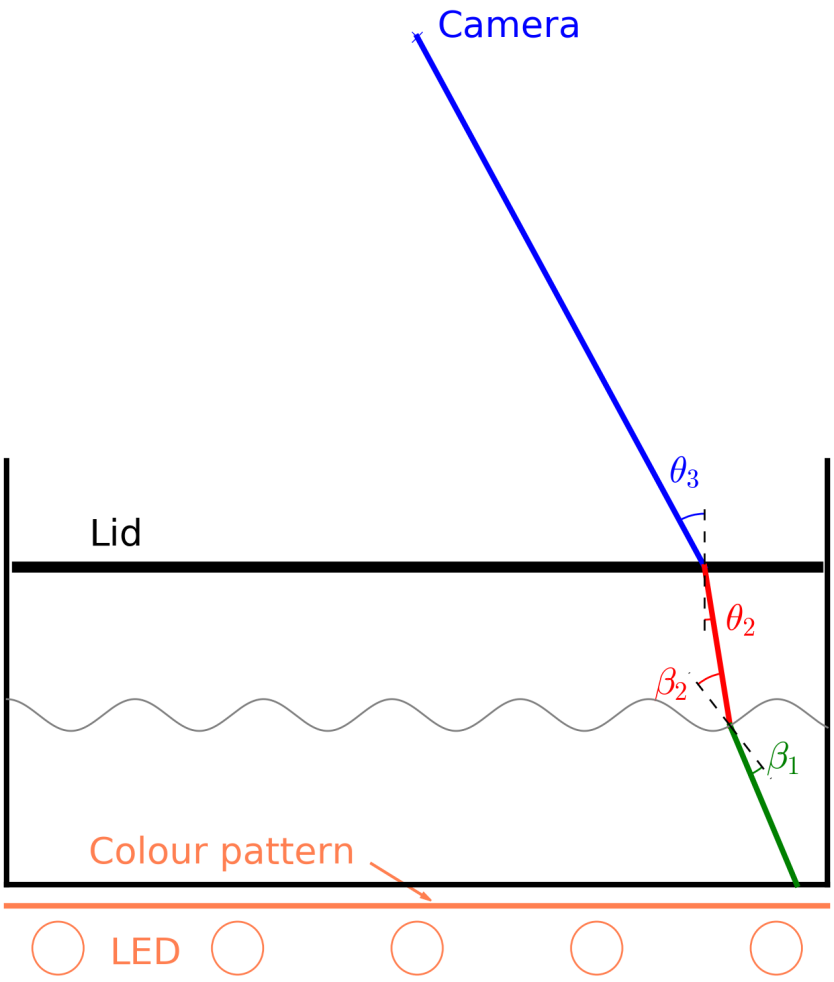

Figure 5.2: Two-dimensional sketch of the experiment, with the trajectory of a ray from the bottom of the tank up to the camera. The camera is placed at the top of the tank. A colour pattern is placed underneath, illuminated by LEDs. The grey wavy line represents the interface between the two layers. The blue line shows the trajectory of the ray in the air, the red one in the upper layer, and the green one in the lower layer.

trajectory between the colour pattern underneath the tank up to the camera at the top of the tank.

We consider an inverse ray trajectory coming from the camera with the same angle θ_3. Note that each light ray is marked by colour. By applying Snell-Descartes law, $n_3 \sin(\theta_3) = n_2 \sin(\theta_2)$, with n_3 and n_2 the optical indices of the air and the upper layer, respectively, on the top-rigid interface, we know the angle θ_2 of the ray to this plane. The ray encounters the top interface at the position $M_2 = (x_2, y_2, H)$, with H the height of the top interface, and we call $\vec{I_2}$ the refracted vector, defined by the position M_2 and the angle

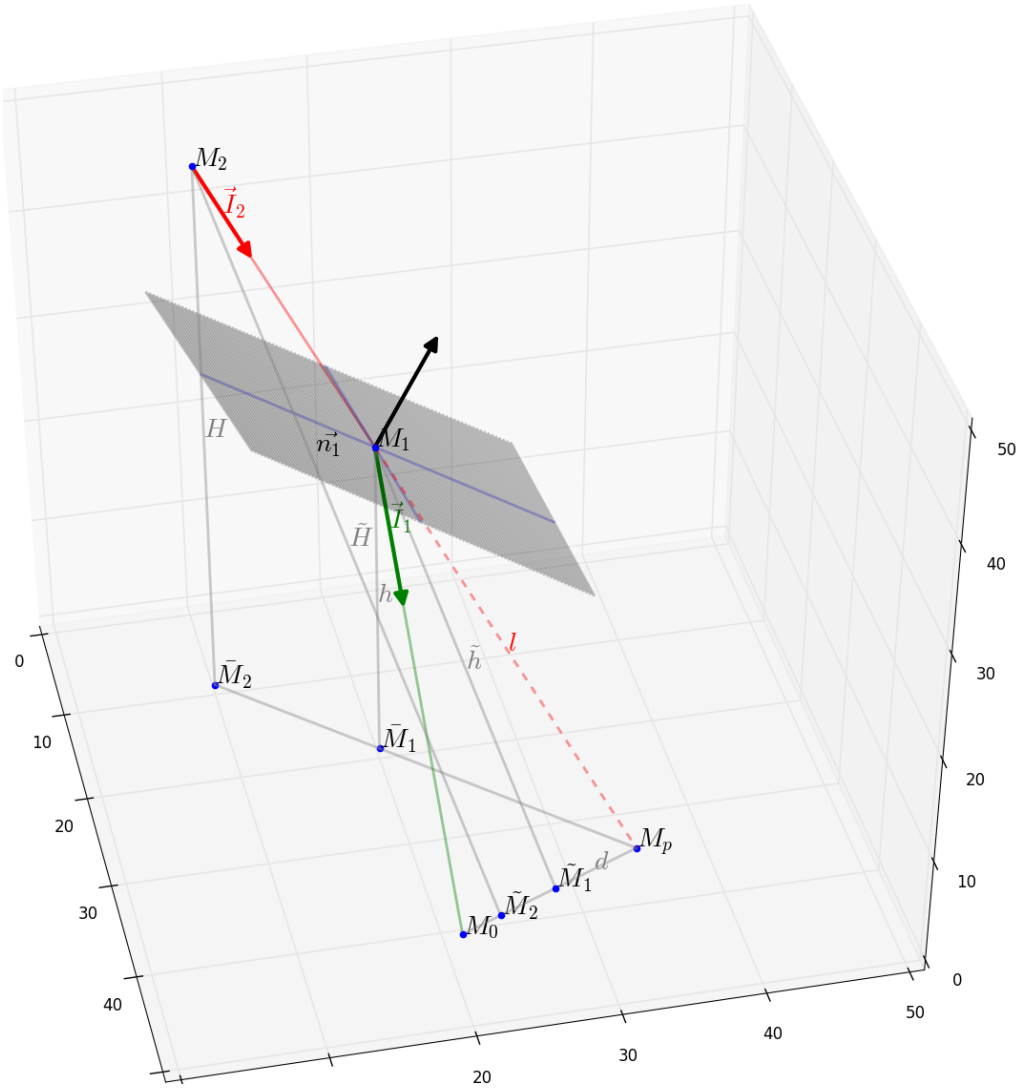

Figure 5.3: Sketch of an inverse light trajectory in the two layers. The solid red line is the light trajectory in the upper layer, with its director vector $\vec{I}_1$, the dashed red line corresponds to the trajectory light would have if the optical indices of the two layers were similar. Its length is l. The green line corresponds to the light trajectory in the lower-layer, with director vector $\vec{I}_1$, and length $\tilde{h}$. The grey plane is normal to the interface, with $\vec{n_1}$ its normal vector.

θ_2. This ray intersects the interface at the point $M_1 = (x_1, y_1, h)$, which is unknown. Next, the ray encounters the colour profile, at the point $M_0 = (x_0, y_0, 0)$. We know the position of this point from its colour (as each pixel has a unique colour) and by converting the colour position to a pixel position and next to a position in centimetres. The incident plane P_1 of the middle interface is defined by the incident vector $\vec{I}_2$ and point M_0. The different points and vectors are shown in figure 5.3, representing the inverse trajectory of

a light ray in the two layers of fluids.

The goal is to find the height and slope in x and y of the middle interface. We can apply Snell-Descartes law at this interface, at point M_1 of the incident plane P_1, $n_2 \sin(\beta_2) = n_1 \sin(\beta_1)$. β_2 and β_1 (see figure 5.2) are respectively the incident and refracted angles compare to the normal at the surface $\vec{n}_1$ and n_1 the optical index of the lower layer. We define a two-dimensional orthonormal coordinate system $(\vec{\tilde{r}}, \vec{\tilde{z}})$ in the incident plane, defined by the vectors $\vec{\tilde{r}}$ and $\vec{\tilde{z}}$, with $\vec{\tilde{r}} = (x_p - x_0, y_p - y_0, 0)/\sqrt{(x_p - x_0)^2 + (y_p - y_0)^2}$, where $M_p = (x_p, y_p, 0)$ is the point at the intersection between the colour profile, the line defined by the vector $\vec{I}_2$ and the point M_2. In other words, the point M_p is the point where the ray should go in case $n_1 = n_2$. $\vec{\tilde{z}}$ is a vector perpendicular to $\vec{\tilde{r}}$ in the incident plane. Note that if the incident planes of the interface and the lid at the surface are similar, we have $\vec{\tilde{r}} = \vec{r}$, the radial vector $\vec{r} = (x_p - x_2, y_p - y_2, 0)/\sqrt{(x_p - x_2)^2 + (y_p - y_2)^2}$, and $\vec{\tilde{z}} = \vec{z}$ the vertical vector $\vec{z} = (0, 0, 1)$. $\beta_2 = \tilde{\theta}_2 - \tilde{s}$, with $\tilde{\theta}_2$ the angle between the vector $\vec{I}_2$ and the vector $\vec{\tilde{z}}$, and $\tilde{s}$ the slope of the interface in the incident plane, defined by $\tan(\tilde{s}) = d\tilde{h}/d\tilde{r}$, with $\tilde{h}$ the height of the interface in the incident plane, i.e. minimum distance between the point (x_1, y_1, h_1) and the line M_0M_p. Similarly, we have $\beta_1 = \tilde{\theta}_1 - \tilde{s}$, with $\tilde{\theta}_1$ the angle between the refracted ray directed by the vector $\vec{I}_1$ and the vector $\vec{\tilde{z}}$.

We can simplify this system to a two-dimensional problem. We call $\tilde{M}_2 = (\tilde{r}_2, 0)$ and $\tilde{M}_1 = (\tilde{r}_1, 0)$ the projections of the point M_2 and M_1 on the line M_0M_p, expressed in the coordinate system $(\vec{\tilde{r}}, \vec{\tilde{z}})$. Similarly, we can write the point M_0 and M_p in this coordinate system: $\tilde{M}_0 = (\tilde{r}_0, 0)$ and $\tilde{M}_p = (\tilde{r}_p, 0)$.

We define d as the distance between the points $\tilde{r}_p$ and $\tilde{r}_0$, and we can link d with $\tilde{\theta}_2$, $\tilde{\theta}_1$ and $\tilde{h}$ using these relations:

$$\left.\begin{aligned} \tan(\tilde{\theta}_2) &= \frac{\tilde{r}_p - \tilde{r}_2}{\tilde{H}} = \frac{\tilde{r}_1 - \tilde{r}_2}{\tilde{H} - \tilde{h}} \\ \tan(\tilde{\theta}_1) &= \frac{\tilde{r}_0 - \tilde{r}_1}{\tilde{h}} \\ d &= \tilde{r}_p - \tilde{r}_0 \end{aligned}\right\} \quad d = \tilde{h}(\tan(\tilde{\theta}_2) - \tan(\tilde{\theta}_1)) \tag{5.1}$$

with

$$\tilde{\theta}_2 = \arcsin\left(\frac{\vec{I}_2.\vec{\tilde{r}}}{\left\|\vec{\tilde{r}}\right\|}\right). \tag{5.2}$$

We can relate the projected height $\tilde{h}$ to h by the relation:

$$\left.\begin{aligned}\cos(\tilde{\theta}_2) &= \frac{\tilde{h}}{l}\\ \cos(\theta_2) &= \frac{h}{l}\end{aligned}\right\} \quad h = \tilde{h}\frac{\cos(\theta_2)}{\cos(\tilde{\theta}_2)} \tag{5.3}$$

with l the length between the point $M_1 = (x_1, y_1, h)$ and the point M_p.

As $\beta_2 = \tilde{\theta}_2 + s$ and $\beta_1 = \tilde{\theta}_1 + s$, using Snell-Descartes law, we obtain:

$$\tilde{\theta}_1 = \arcsin(n_2/n_1 \sin(\tilde{\theta}_2 - s)) + s. \tag{5.4}$$

So, we get

$$\tilde{h} = \frac{d}{\tan(\tilde{\theta}_2) - \tan(\arcsin(n_2/n_1 \sin(\tilde{\theta}_2 - s)) + s)}. \tag{5.5}$$

Using the relation of the tangent $\tan(a+b) = \frac{\tan a + \tan b}{1 - \tan a \tan b}$, we can simplify the equation 5.5 to:

$$\begin{aligned}&\frac{n_2(\sin(\tilde{\theta}_2) - \cos(\tilde{\theta}_2)\tan(s)) + \tan(s)q(s)}{q(s) - \tan(s)(n_2(\sin(\tilde{\theta}_2) - \cos(\tilde{\theta}_2)\tan(s)))} - \tan(\tilde{\theta}_2) + \frac{d}{\tilde{h}} = 0\\ &q(s) = \sqrt{n_1^2(1+\tan(s)^2) - n_2^2(\sin(\tilde{\theta}_2) - \cos(\tilde{\theta}_2)\tan(s))^2}\\ &\tan(s) = \frac{d\tilde{h}}{d\tilde{r}} = \tilde{h}'.\end{aligned} \tag{5.6}$$

From equations 5.6, we know the slope in the incident plane P_1. We can write the normal vector $\vec{n_1} = (n_{1x}, n_{1y}, n_{1z})$ to the interface in terms of the obtained slope in the coordinate system (x, y, z). And from the normal vector, we have the slope in x and y directions

$$\begin{aligned}\vec{n}_1 &= \frac{\vec{\tilde{r}} + (0, 0, \tilde{h}')}{\sqrt{\vec{\tilde{r}}^2 + \tilde{h}'^2}}\\ \frac{\partial h}{\partial x} &= \frac{n_{1z}}{n_{1x}}\\ \frac{\partial h}{\partial y} &= \frac{n_{1z}}{n_{1y}}\end{aligned} \tag{5.7}$$

5.4 Numerical implementation

Equations 5.6 represent a non-linear first order differential equation, for which an initial condition is needed to solve it. We will use a reference height of the interface at one point (x_i, y_i). Knowing the height of the interface at this point, we can find the height and the slope of the entire flow.

The algorithm to find the slope in x and y from the height is the following. We compute the distance d and the angle $\tilde{\theta}_2$ from the relations 5.1 and 5.2. From equation 5.3, we obtain a relation between the height h in the coordinate system (x, y, z) and the projected height $\tilde{h}$ in the coordinate system $(\tilde{r}, \tilde{z})$. To find the slope of the interface from the height at this given point, we need to solve the non-linear differential equation 5.6. First, by iterating the slope angle s, defined by $\tilde{h} = \tan(s)$, from 0 to 2π, with a chosen increment $k_{\tilde{h}'}$, we find in between the increments $k_{\tilde{h}'}$ the function

$$f(\tilde{h}') = \frac{n_2(\sin(\tilde{\theta}_2) - \cos(\tilde{\theta}_2)\tan(s)) + \tan(s)q(s)}{q(s) - \tan(s)(n_2(\sin(\tilde{\theta}_2) - \cos(\tilde{\theta}_2)\tan(s)))} - \tan(\tilde{\theta}_2) + \frac{d}{\tilde{h}}$$

that changes sign. Next, we apply the Newton-Raphson method to find the root of this function.

Thus, we have the slope $\tilde{h}'$ of the projected interface in the incident plane P_2 at this point. Thanks to the relations 5.7 we can obtain the normal vector $\vec{n}_1$ and the slope in x and y directions. Finally, we obtain the height h.

We consider a circular tank, so we have adapted the code to be able to compute the height for this geometry. Two different ways of computing the height of the interface are implemented. Sketches in figure 5.4 illustrate these two ways. In both cases, we know the height at the point (x_i, y_i), which is represented by a red cross on the sketches. We focus first on the sketch in the left panel. From this point, we find the height of the next point in the x direction (x_{i+1}, y_i) by applying a predictor-corrector method. This process can be iterated until the end of the domain; it is represented by the big turquoise arrow in the left panel. Next, we repeat for x positions smaller than x_i – the green arrow. Similarly, for each x position, the same algorithm can be applied for y higher than y_i (orange arrows) and smaller than y_i (coral arrows). However, with this procedure, we miss two areas which are delimited by dashed lines. For these areas, we compute for each y value the missing x values. We call the height obtained from this procedure h_{xy}. Similarly, the

same procedure can be applied though we start by computing the height for all y values for x_i and next for each y value for all x values, we obtain a height called h_{yx}. The right panel in figure 5.4 illustrates this procedure. In order to improve the result, the final height h_c is taken as the average between these two heights. Section §5.5.3 shows the error difference obtained using h_{xy}, h_{yx} and h_t.

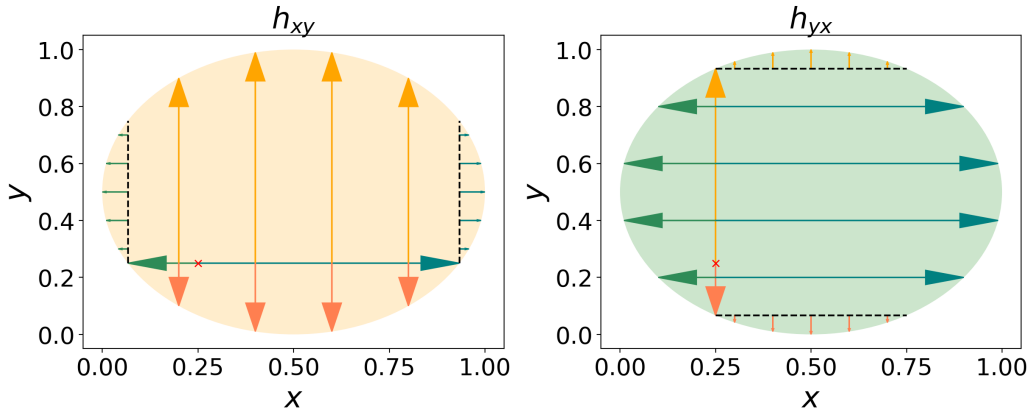

Figure 5.4: Two different ways to obtain the height are sketched here, h_{xy} on the left panel and h_{yx} on the right panel. Turquoise arrows are directed rightward, green arrows are directed leftward, orange arrows are directed upward and coral arrows are directed downward.

5.5 Numerical validation

To verify the code, we numerically build a two-layer profile with an imposed interface. Two setups have been used to test the code. The first one is a small virtual tank of a $30cm$ diameter, with $6.3cm$ of water filled with two layers of immiscible fluids. This configuration allows the efficiency of the code for capturing small perturbations to become apparent. The second configuration is similar to the tank used in chapter 4. We use a virtual tank of a diameter of $1.30m$ filled with two layers of immiscible fluids, each $15cm$ deep. For the two setups, we have a tank with a colour profile at the bottom, two layers of fluids in the tank, a rigid lid on the top and a camera at a height of H_c from the bottom of the tank. The lower layer fluid has an optical index of $n_1 = 1.3787$ and the upper layer has an optical index of 1.33. Section §5.5.1 shows the difference between the two configurations. Section §5.5.2 shows the difference for one configuration between different height profiles. Finally, section §5.5.3 shows the impact on the height of different ways of computing the height.

5.5.1 Different setups

Different configurations have been tested, either a small tank of 30cm diameter, filled with two layers of fluids with the mean lower layer equals to $H_1 = 3.5$cm and the mean upper layer equal to $H_2 = 2.8$cm. In the second setup, we have a bigger tank of a 130cm diameter, with $H_1 = 15$cm and $H_2 = 15$cm. In both cases, the camera is placed at a height of $H_c = 210$cm from the bottom of the tank. Two simulations have been run for the two configurations with a comparable perturbation value. The amplitudes of the perturbations are similar in terms of pixel, though as the factor linking pixels to centimetres is different in the two experiments, the slope is different.

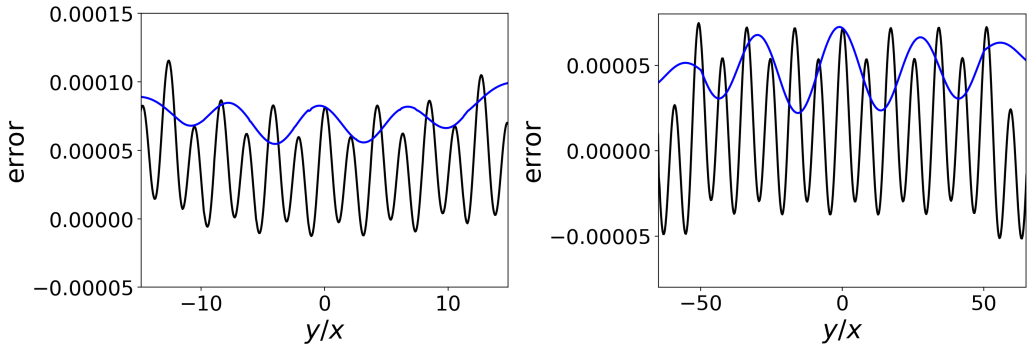

Figure 5.5: Error $(h_t - h_c)/h_t$ between the theoretical profile h_t and the computed profile h_c, for the small tank configuration (left panel) and the big tank configuration (right panel). Black lines: values for $x = 0$cm, blue lines: values for $y = 0$cm.

Figure 5.5 exhibits two different graphs. The left figure shows the error $(h_t - h_c)/h_t$ for the small tank setup, with h_t the theoretical height and h_c the computed height. The right figure shows the error $(h_t - h_c)/h_t$ for the large tank setup. Black lines correspond to the error for $x = 0$cm, and blue lines correspond to the error for $y = 0$cm. The two setups have comparable error values and profiles, with errors smaller than 10^{-4} almost everywhere except for the error for $x = 0$cm in the small tank configuration, where the error exceeds 10^{-4} around $y = -13$cm. The error's range, then, does not strongly depend on the configuration.

5.5.2 Different perturbations

Different interface profiles h_t have been implemented to verify the consistency and precision of the numerical method. A monochromatic wave in x direction and next in y

direction have been implemented. Then, an interface profile based on the addition of three monochromatic waves with different amplitudes propagating in different directions has been implemented:

$$h_t = H_1 + \sum_{i=1}^{3} a_i \cos(2\pi\lambda_i(\alpha_i x + \beta_i y))$$

with a_i the amplitude of each wave i and λ_i the wavenumber, α_i and β_i are coefficients which control the direction of the wave. Figure 5.6 shows the theoretical profile h_t on the left panel and the error $(h_t - h_c)/h_t$, with h_c the computed profile in the small tank configuration for small amplitude waves on the right panel.

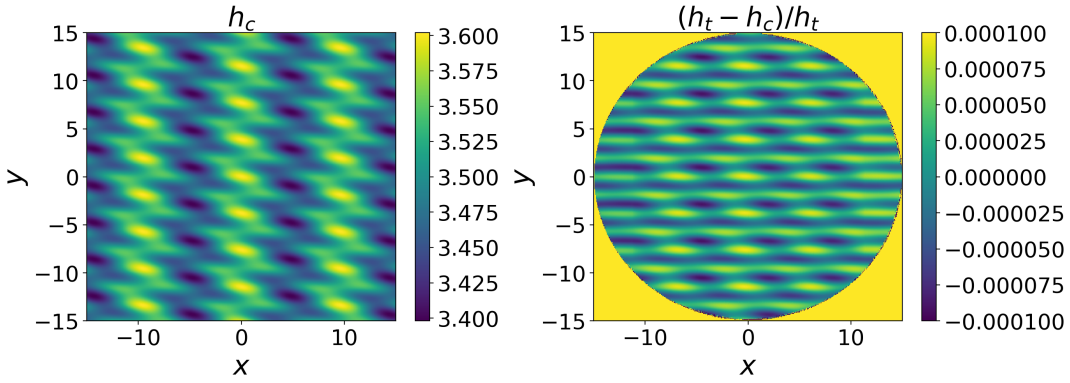

Figure 5.6: Left panel: numerical interface profile based on the addition of three small amplitude monochromatic waves propagating in different directions, for the small tank configuration. Right panel: ratio of the difference between the imposed profile h_t and the profile h_c obtained from the code, $(h_t - h_c)/h_t$.

Different amplitudes of waves have been tested to know the impact of the slope on the error. A first wave has amplitude of the order of a millimetre, a second one is ten times bigger, i.e. amplitude of a centimetre. A third wave has amplitude of the order of 10^{-3}cm. Similarly, we implemented two simulations with different amplitudes for the large tank configuration, the first one with amplitude of the order of a centimetre and the second one with amplitude of ten centimetres. As seen previously in section §5.5.2, the setup does not have a strong impact on the error. This is also the case for these different simulations, i.e. one-centimetre amplitude perturbations in the small tank are equivalent to ten-centimetre amplitude perturbations in the large tank, and one-millimetre amplitude perturbations in the small tank are equivalent to one-centimetre amplitude perturbations in the large tank.

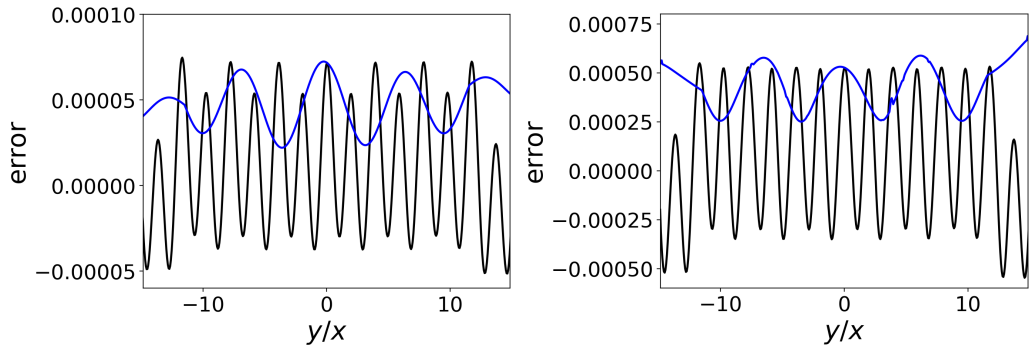

Figure 5.7: Error $(h_t - h_c)/h_t$ between the theoretical profile h_t and the computed profile h_c, for small perturbations (left panel) and large perturbations (right panel), for the small tank configuration. Black lines: values for $x = 0$cm, blue lines: values for $y = 0$cm.

Figure 5.7 shows the error differences between large-scale (centimetre) perturbations and small-scale (millimetre) perturbations, for the small tank configuration. The left panel shows the small-scale perturbations error $(h_t - h_c)/h_t$, the right panel shows the large-scale perturbations error, with black lines the error for $x = 0$cm and blue lines the error for $y = 0$cm. The order of magnitude is ten times larger for large-scale perturbations than for small-scale perturbations. Note that, for the simulation with very small amplitude perturbations – 10^{-3}cm – we obtain an error of the order of 10^{-6}.

In order to know whether the amplitude of the perturbation or the slope is the main factor of the difference of error between the small perturbations and the large perturbations, we implemented three simulations with monochromatic waves with different amplitudes and wavenumbers. Figure 5.8 shows the slope (top left panel), the height (top right panel) and the error (bottom panel) for the three simulations. The black and red lines have the same amplitude but different wavenumbers. Conversely, black and blue lines have different amplitudes but the same wavenumbers. We can see that the blue and the black simulations have comparable slopes, but the error is twice more important for the red simulation. Furthermore, black and red simulations have the same amplitude perturbations, although the error is drastically more important for the red simulation. The error seems to be directly proportional to the derivative of the slope. So, the major factor seems to be the second derivative of the height.

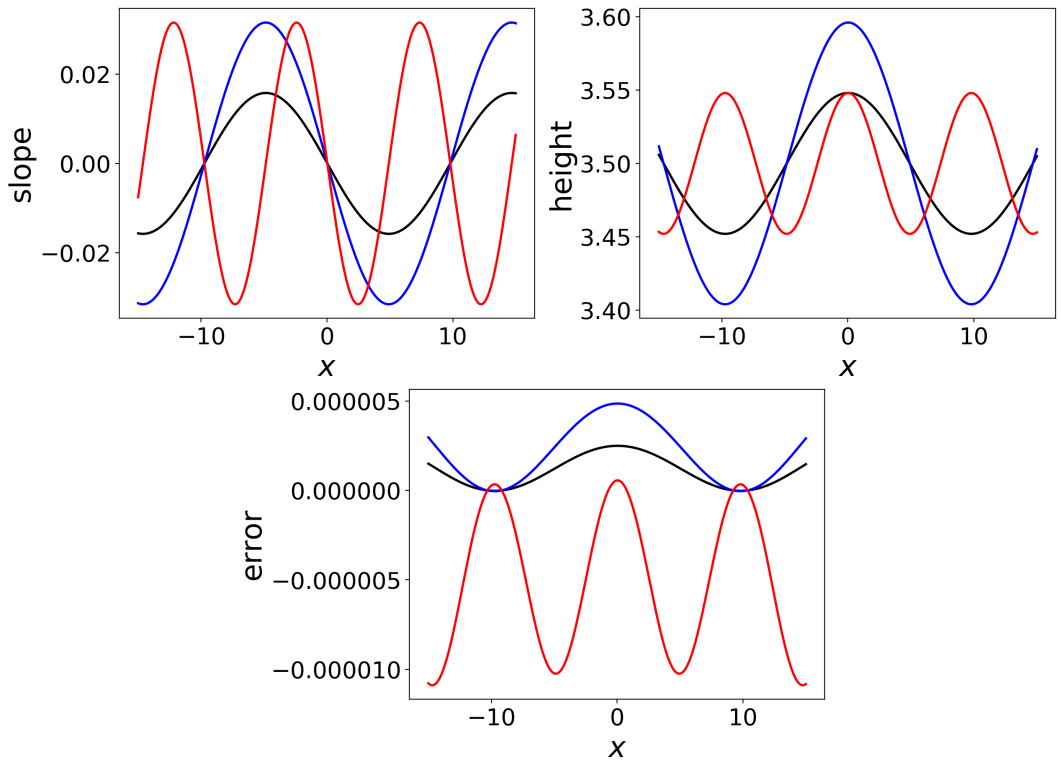

Figure 5.8: Top left panel: slope of the interface for three different simulations. Top right panel: height of the interface. Bottom panel: height error. Blue and red simulations have same perturbations' slope amplitudes. Black and red simulations have same perturbations' height amplitude.

5.5.3 Different height computations

First, we compare the different ways to compute the height presented in the former section. This is done either by computing first the height for all x for y_i and next iterating the algorithm for each x for all y indices; h_{xy}, or the other way around, by first iterating for all y for x_i and next for each y for all x, to obtain h_{yx}. By taking the average of these two heights, we obtain h_c. Figure 5.9 shows profiles of the error between the theoretical height h_t and the computed heights: $(h_t - h_{xy})/h_t$ in black, $(h_t - h_{yx})/h_t$ in blue, $(h_t - h_c)/h_t$ in red, for $x = 0$cm on the left panel and $y = 0$cm on the right panel, for the small tank configuration, with small-scale perturbations. We can see that the three results are comparable, though we still improve the results by considering h_c rather than only h_{xy} or h_{yx}. In both cases, the error is smaller than 10^{-4}.

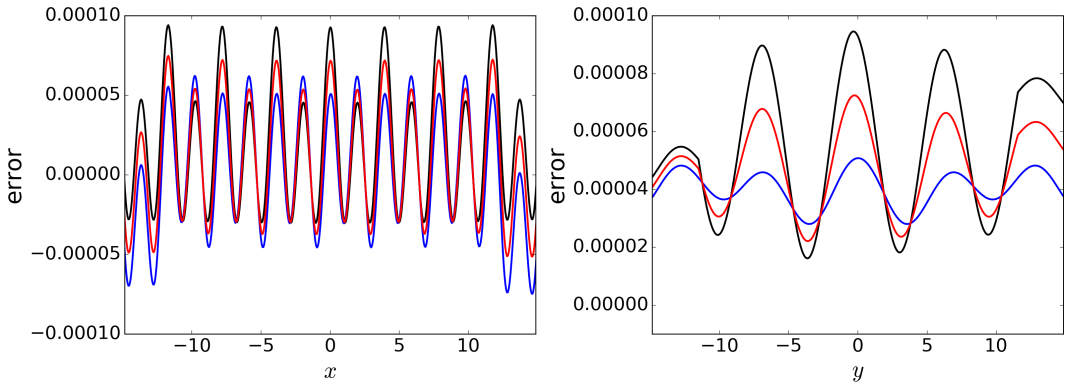

Figure 5.9: Error $(h_t - h)/h_t$ between the theoretical profile h_t and three computed profiles h, for $y = 0cm$ in the left panel and for $x = 0cm$ in the right panel. Black lines: $h = h_{xy}$, blue lines: $h = h_{yx}$, red line $h = h_t$.

5.6 Conclusion

Inspired by the optical AVI method used for a single layer (see Afanasyev et al. [2009]), we have developed a new optical method to measure accurately the height of an interface, using the comparison between an initial image with a colour profile and an image with perturbation of this profile. The two fluids need to have different optical indices and we have supposed that the interface is sharp, allowing the use of Snell-Descartes optical laws to obtain a first-order non-linear equation linking the height and the slope. The reference height is needed at one point to be able to compute it in the entire domain. With the height at this point, we can solve the first order non-linear equation. This reference height should be measured with a probe (acoustic, laser, ...) at a position that corresponds with a light ray, i.e. in the field of view.

The code has been tested using different virtual tank configurations, with different interface profiles. It is possible to capture very small waves as much as large-amplitude perturbations. However, the precision decreases when the second derivative of the height becomes too important. In the different cases here considered, from the extremely high amplitudes and steep perturbations in the large tank to the small amplitude oscillations in the small tank, the error between the theoretical height and the computed height is never higher than 10^{-3} the theoretical height. So, we have a very precise method to detect the height of the interface.

However, as we have to solve first order non-linear equations for each point, the code is not very fast and needs one to two hours to obtain the height for one image using

a single core computer. The code can be easily parallelised, since all time steps are absolutely independent from one another. Additionally, for each time step, h_{xy} and h_{yx} can be computed independently, thus cutting the time in half for each time step.

An experimental validation of this method remains to be performed. We need to determine this effect of local noise on the quality of the entire profile. This could be done in the first instance numerically. This would help understand the limits of resolution that can be captured by this method as well as the limits on interface slopes. Furthermore, it would be interesting to compare the precision of our method with the precision of the polarimetry method [Lovegrove et al., 1999]. In our method we use the angle of the interface whereas in Lovegrove et al. [1999] they use the height of the interface, which is measured from the optical rotation of the light.

This method is very promising, as we will obtain the entire profile of the interface with a very high spatial resolution. Additionally, as it will be used with immiscible fluids, experiments can be conducted during very long periods. This spatial and temporal improvement will offer a better understanding of the formation and evolution of vortices and show the impact of small waves on their dynamics. Then, this method could perhaps be extended to flows with a miscible and thick interface to linear stratification, supposing little mixing.

Chapter 6

Conclusion and perspectives

In this chapter, the overall results and their possible perspectives are discussed.

Jets and vortices are omnipresent in turbulent planetary atmospheres, both on telluric planets like the Earth, as well as on gas giants like Jupiter or Saturn. Jupiter exhibits a peculiar feature: namely, the permanent coexistence of jets and vortices. In this study, we have used a dual approach of both numerical simulations and laboratory experiments to study the formation and evolution of jets and vortices in turbulent planetary atmospheres. We have decided to adopt a shallow-layer approach, assuming that jets emerge through an upscale cascade of geostrophic turbulence. In this final chapter, we first review the key findings obtained from a numerical approach using a highly accurate numerical method. Then we review our experimental findings, including a novel approach to visualisation of the interface between two immiscible fluids. Finally, we present a few ideas for future research that have emerged from this thesis.

In chapters 2 and 3, we have investigated the emergence and evolution of jets using a two-layer β-plane quasi-geostrophic shallow-water channel model (based on Phillips's model, see Phillips [1951]). We model the stratification as an exponential decrease of the density profile. Following Panetta and Held [1988], a vertical shear is implemented to represent the latitudinal temperature gradient representing the thermal forcing variation between the equator and the poles. This vertical shear is maintained by thermal relaxation which tends to bring the interfaces of the two layers back to the state imposed by the vertical shear. To mimic convective motions, a spatially-random addition of hetons is implemented, as in Thomson and McIntyre [2016]. The hetons contribute to the destabil-

isation of the flow. In chapter 3, stochastic forcing is replaced by an initial lower layer Rossby wave perturbation, which allows for an initial destabilisation of the flow. The stochastic forcing has little impact on the flow, except for increasing background perturbations and thus making the flow more resistant to the vertical shear. More than one hundred simulations have been run using the Combined Lagrangian Advection method (Dritschel and Fontane [2010]), for at least 10^4 and up to 10^5 units of time. Simulations of this accuracy over such durations have never before been conducted in this context and they have led to new insights into jet formation and dynamics.

The initial state imposed by the vertical shear is baroclinically unstable. Hetons moreover contribute to the destabilisation of the flow. This leads to heterogeneous potential vorticity mixing, which creates regions where potential vorticity is relatively homogeneous, separated by regions of potential vorticity jumps called jets (see Dritschel and McIntyre [2008], Scott and Dritschel [2012]). Thermal relaxation tries to bring the interface back to the imposed vertical shear state, whereas baroclinic instability develops and reduces the vertical shear. This competition between thermal relaxation and baroclinic instability leads to the continuous evolution of jets. For a specific regime in vertical shear and thermal relaxation, turbulent phases appear from time to time. During these phases, the flow loses its zonal organisation and forms large eddies and generally more turbulence. The turbulent phases last for a thermal relaxation period before recovering to a quiescent phase, when the flow is organised in nearly zonal bands.

We have also investigated the energetics during the turbulent phases. At the beginning of turbulent phases, all the zonal energy components drop, which corresponds to the loss of zonality. At the same time, the eddy energy components increase due to the formation of eddies pinching off the meandering jets. Next, eddies transfer their energy back to jets through heterogeneous potential vorticity mixing. Zonal available potential energy takes longer to recover, as it is directly linked to the thermal relaxation period.

The dependence of the flow evolution on vertical shear, thermal relaxation, topography, stratification, heton intensity and enstrophy input rate has been studied. The flow strongly depends on thermal relaxation. Without thermal relaxation, baroclinic instability breaks down the initial state imposed by the vertical shear, but no recovery or baroclinic instability are then possible. If the thermal relaxation is too strong, it inhibits the formation of turbulent phases. Oscillations between quiescent phases and turbulent phases, then, are only possible for a specific regime in vertical shear and thermal relaxation. Notably, jets are globally more intense and jet spacing is larger for weaker thermal relaxation.

The stronger the vertical shear, the more unstable is the flow. For a small vertical shear, the flow is very stable and no turbulent phases appear. Jet spacing and jet intensity increase with vertical shear.

Different stratifications have been examined, mainly an atmospheric case, but also an oceanic case. For the oceanic case, jets are more meandering, and, globally the flow is less homogeneous, but rather composed of a multitude of vortices.

The impact of topography was investigated in chapter 3. For a given vertical shear, topography can either bring the flow to the margin of stability or bring a stable flow to instability (as seen in Chen and Kamenkovich [2013]), and to simulations where oscillations between quiescent phases and turbulent phases are present. Topography that deepens northward makes turbulent phases more intense, with a higher and steeper drop of zonal available potential energy. Additionally, we obtained jets slowly drifting north or south. This has already been observed in Boland et al. [2012], in the context of meridional and zonal topographies, or in Nature, as in Thompson and Wallace [2000], Barnes and Polvani [2013].

In chapter 4, we have studied the formation of fronts and vortices in a rotating cylindrical tank filled with two salt-stratified miscible fluids. In order to create an interface allowing baroclinic instability, we used a rigid lid spinning faster than the rotating platform. We analysed two experiments conducted by JH Thysen. By the addition of rhodamine 6G in one layer, light intensity, showing the interface between the two layers, was recorded. Additionally, particle images were recorded, which allowed us to use particle images velocimetry. The flow was analysed using different methods. From the particle images, we used the software UVmat to obtain the vorticity of the flow. Using the light intensity images, different methods have been developed. First, we looked at the light intensity variation around a chosen circle. This method allowed us to capture waves and large-scale perturbations. But in the presence of large-amplitude, small wavenumber perturbations, large wavenumber perturbations were difficult to observe. A second method based on the computation of the light intensity contours was therefore developed. This method is very accurate and provides a precise power spectrum of the contour. However, due to the variation in contour sizes, it is difficult to obtain the time evolution of the power spectrum using this approach. A third method computed the temporal and azimuthal spectrum from the radially-averaged light intensity. Finally, by subtracting two consecutive images, we obtained the density derivative. This approach offered a clear view of the temporal evolution of waves on the interface. In addition, a radial mean was

calculated to obtain the time evolution of the azimuthal spectrum.

Following the work of Scolan et al. [2014] on amplitude vacillations, two experiments have been analysed, both having the same flow parameters, except for the Rossby number. Amplitude vacillations were present in both cases. We found vortices emerging from the front, centring, merging into the mean flow and stabilising it, until a new vortex emerged and the process started again. However, amplitude vacillations were strongly different in these two experiments. For the small Rossby number ($Ro = 0.405$), the formation of a vortex was highly correlated to small wave activity. The vortices that formed were baroclinic dipoles and their radius was comparable to the baroclinic Rossby deformation radius. In the experiment with a larger Rossby number ($Ro = 0.572$), we had barotropic vortices emerging from large-scale disturbances. Their radius was comparable to the barotropic Rossby deformation radius. This result matches the observations of baroclinic and barotropic vortices recorded in Carton [2010]. The Rossby number also impacted the recovery period of amplitude vacillations. The experiment with a larger Rossby number presented a longer recovery period, linked with the fact that more mixing occurred and that the interface had been flattened.

In chapter 5, we have presented a new optical method that has been developed for a rotating tank filled with two immiscible fluids, with a rigid lid on top. A camera is placed on top of the tank. The rotation is not mandatory for our method, but the two fluids need to have different optical indices. A colour pattern is placed at the bottom of the tank and illuminated from underneath. Using refractive optical laws, we can compute the height of the interface between the two layers. The algorithm to compute the interface is based on a first-order non-linear equation linking the height and the slope of the interface. The height at one point in the domain, then, is necessary to be able to compute the entire height profile. This could be obtained from a probe, a laser, or using an acoustic method.

The code was tested using two virtual tanks for various interface profiles. The precision of the height decreases with its second derivative, though it is precise enough to capture the kind of flow we were interested in. From steep high-amplitude perturbations to small-amplitude perturbations, the error between the theoretical height and the obtained height was never higher than 10^{-3} the theoretical height. To obtain the height from a 512×512 grid, we needed between one to two hours using a single core computer. However, the code can be parallelised easily, both in time and in space. Each time step can be computed independently from the other and we can further halve the computation in space. In the future, we will conduct an experimental verification. Then this method

could be extended to study other stratifications, such as linear stratification or thick interfaces.

To summarise, with a dual approach we have investigated the formation of jets and vortices in turbulent planetary atmospheres. Similarities can be found between the two studies. In both cases, the time evolution of the flow exhibits oscillations. Oscillations between quiescent and turbulent phases were found in the numerical study. During the turbulent phases, the flow loses its zonality, forms eddies, and becomes generally more turbulent. In the experimental study, amplitude vacillations were visible, with large-scale vortices forming, followed by quiescent phases when the flow recovers.

New experiments could be conducted for Rossby numbers between $Ro = 0.405$ and $Ro = 0.572$ to see if the transition from baroclinic dipoles to barotropic vortices is gradual or abrupt. A Hilbert transform could be applied to LIF measurements to evaluate whether triadic interactions are present. With the new optical method developed and presented in chapter 5, we obtain the experiments full height profile. By using immiscible fluids, no mixing occurs, so experiments could last for a long time. Typically, we can model around nine years in a single day. Knowing the entire profile of the interface for such long periods will both improve our understanding of the formation and evolution of vortices and allow us to better assess the impact of small waves on their dynamics. We further plan to add a spinning bottom to the experimental set-up for an experimental equivalent to the Phillips's model. Additionally, vortices will be created on the edge of the tank to observe the interactions between fronts and vortices.

In the numerical study, we investigated the formation of jets and vortices using a two-layer quasi-geostrophic β-channel model. It would be interesting to see if we can obtain similar oscillations between quiescent and turbulent phases using another model, namely, the shallow-water approximation or the primitive approximation. We could further vary the number of layers and the geometry, for instance, changing it to spherical geometry. Also, no long-lived vortex is present in our simulations – varying the approximation might enable us to obtain a persistent co-existence of jets and vortices.

Moreover, the appearance of turbulent phases in the flow is a fascinating phenomenon. Can such a phenomenon be found in Nature during climate variations? In a first approach, it would be interesting to acquire an estimate of the period between two turbulent phases and its dependence on the different parameters.

Additionally, the study of drifting jets should be expanded. Possible points of atten-

tion could include the impact of topography and of the potential vorticity gradient in each layer on the direction of propagation and on the drift velocity. Would the distribution of the drifting direction be random? Further, would the drifting jets be more stable (containing fewer turbulent phases) than non-drifting jets? Answers to these question will widen our knowledge on the dynamics and formation of these jets.

Appendix A

Layer model decomposition and related analyses

A.1 Vertical modes

The inversion of (2.8) for the layer streamfunctions ψ_1 and ψ_2 is accomplished through a projection onto vertical modes, i.e.

$$\begin{aligned} \hat{\psi}_1 &= c_{11}\psi_1 + c_{12}\psi_2 \\ \hat{\psi}_2 &= c_{21}\psi_1 + c_{22}\psi_2 \end{aligned} \tag{A.1}$$

where a hat indicates a vertical mode, and the c_{ij} are the projection coefficients, determined as follows. Using the same projection for the PV anomaly $q_i' - \beta y$ in (2.8), we obtain

$$\hat{q}_j' = \nabla^2\hat{\psi}_j + c_{j1}h_2\bar{k}_d^2(\alpha\psi_2 - \psi_1) + c_{j2}h_1\bar{k}_d^2(\psi_1 - \psi_2) \tag{A.2}$$

for each vertical mode ($j = 1$ or 2). The objective is to make the terms involving c_{j1} and c_{j2} equal to $-\gamma_j\bar{k}_d^2\hat{\psi}_j$ for each j, since then we have simple Helmholtz-type equations to invert for $\hat{\psi}_j$, namely

$$\hat{q}_j' = \nabla^2\hat{\psi}_j - k_{dj}^2\hat{\psi}_j \tag{A.3}$$

where $k_{dj}^2 \equiv \gamma_j \bar{k}_d^2$ is the squared deformation wavenumber for mode j. Equating then the terms above with $-\gamma_j \bar{k}_d^2 \hat{\psi}_j$ and re-arranging, we obtain

$$[(\gamma_j - h_2)c_{j1} + h_1 c_{j2}]\,\psi_1 + [(\gamma_j - h_1)c_{j2} + \alpha h_2 c_{j1}]\,\psi_2 = 0. \tag{A.4}$$

As this must be true for all $\psi_1(x, y, t)$ and $\psi_2(x, y, t)$, the constant coefficients must vanish:

$$(\gamma_j - h_2)c_{j1} + h_1 c_{j2} = 0 \tag{A.5}$$

$$(\gamma_j - h_1)c_{j2} + \alpha h_2 c_{j1} = 0. \tag{A.6}$$

$$\tag{A.7}$$

The only nontrivial solution results by taking the determinant of this linear system to be zero, leading to

$$\gamma_j^2 - \gamma_j + (1 - \alpha)h_1 h_2 = 0 \tag{A.8}$$

which gives the prefactor γ_j in $k_{dj}^2 \equiv \gamma_j \bar{k}_d^2$:

$$\gamma_{1,2} = \frac{1}{2} \mp \sqrt{\frac{1}{4} - (1 - \alpha)h_1 h_2}. \tag{A.9}$$

We have taken the minus sign in front of the square root for the lower mode, since it is purely 'barotropic' with $\gamma_1 = 0$ in the Boussinesq limit $\alpha \to 1$. The other mode is called 'baroclinic' and always has the higher deformation wavenumber. Note: $\gamma_1 + \gamma_2 = 1$.

Regarding the projection coefficients c_{j1} and c_{j2}, by convention we take $c_{11} + c_{12} = 1$ for the 'barotropic' mode $j = 1$. This, along with (A.5) gives

$$c_{11} = \frac{h_1}{1 - \gamma_1} = \frac{h_1}{\gamma_2} \quad ; \quad c_{12} = 1 - \frac{h_1}{\gamma_2}. \tag{A.10}$$

For the 'baroclinic' mode $j = 2$, we take $c_{22} = 1$. Again using (A.5), we find

$$c_{21} = \frac{h_1}{h_2 - \gamma_2} \quad ; \quad c_{22} = 1. \tag{A.11}$$

The inverse of these coefficients are needed to express modes in terms of layers, i.e. as

$$\begin{aligned}\psi_1 &= \tilde{c}_{11}\hat{\psi}_1 + \tilde{c}_{12}\hat{\psi}_2\\ \psi_2 &= \tilde{c}_{21}\hat{\psi}_1 + \tilde{c}_{22}\hat{\psi}_2.\end{aligned} \tag{A.12}$$

Simple algebra leads to

$$\tilde{c}_{11} = \frac{c_{22}}{\Delta} \quad ; \quad \tilde{c}_{12} = -\frac{c_{12}}{\Delta} \quad ; \quad \tilde{c}_{21} = -\frac{c_{21}}{\Delta} \quad ; \quad \tilde{c}_{22} = \frac{c_{22}}{\Delta} \tag{A.13}$$

where $\Delta = c_{11}c_{22} - c_{12}c_{21}$.

A.2 Vertical shear

A vertical shear (a uniform flow $\bar{u}_i$ in each layer i) is imposed by taking the lower layer mean PV to be $\bar{q}_1 = -\epsilon_1\beta y$, specifying ϵ_1, and requiring the mass-integrated momentum to be zero, or $h_1\bar{u}_1 + \alpha h_2\bar{u}_2 = 0$. The latter requirement determines the constant ϵ_2 in the associated upper layer PV $\bar{q}_1 = \epsilon_2\beta y$, as well as the mean flows $\bar{u}_1$ and $\bar{u}_2$, as explained next.

We start with (2.8) for the mean flow, for which $\bar{\psi}_i = -\bar{u}_i(y - y_c)$, where y_c is the centreline of the channel. For this flow, the relative vorticity $\nabla^2\bar{\psi}_i$ is zero. After cancelling the common y factor and some re-arrangement, (2.8) implies

$$\begin{aligned}(1-\epsilon_1)\beta &= h_2\bar{k}_d^2(\alpha\bar{u}_2 - \bar{u}_1)\\ (1-\epsilon_2)\beta &= h_1\bar{k}_d^2(\bar{u}_1 - \bar{u}_2).\end{aligned} \tag{A.14}$$

We can solve these for the mean flows $\bar{u}_1$ and $\bar{u}_2$ in terms of ϵ_1 and ϵ_2, but we also want to obtain ϵ_2 from the condition of zero momentum, $h_1\bar{u}_1 + \alpha h_2\bar{u}_2 = 0$. Omitting the details, this gives $\epsilon_2 = 1 + (1-\epsilon_1)G_1/G_2$ where $G_j = c_{1j}\gamma_2 + \mu c_{2j}\gamma_1$ with

$$\mu = \frac{h_1\tilde{c}_{12} + \alpha h_2\tilde{c}_{22}}{h_1\tilde{c}_{11} + \alpha h_2\tilde{c}_{21}}. \tag{A.15}$$

The mean velocities $\hat{\bar{u}}_j$ associated with each mode j are

$$\hat{\bar{u}}_1 = \frac{(1-\epsilon_1)\beta\Delta}{\bar{k}_d^2 G_2} \quad ; \quad \hat{\bar{u}}_2 = -\mu\hat{\bar{u}}_1, \tag{A.16}$$

from which we obtain the mean layer velocities by projection:

$$\bar{u}_i = \tilde{c}_{i1}\hat{\bar{u}}_1 + \tilde{c}_{i2}\hat{\bar{u}}_2 \quad i = 1,\, 2. \tag{A.17}$$

A.3 Thermal equilibrium Interface slopes

Initially, the flow is in thermal equilibrium, with uniform velocity $\bar{u}_i$ in each layer i. Associated with this flow, by thermal wind balance, the layer interfaces adopt a linear profile $\delta_{\mathsf{eq},i} \propto y - y_c$. In terms of the scaled displacements $\tilde{\delta}_{\mathsf{eq},i} = f_0\delta_{\mathsf{eq},i}/H$, upon using their definitions in terms of streamfunctions (2.12), we find

$$\tilde{\delta}_{\mathsf{eq},1} = -h_1h_2\bar{k}_d^2(\bar{u}_1 - \alpha\bar{u}_2)(y - y_c) \quad ; \quad \tilde{\delta}_{\mathsf{eq},1} = -h_1h_2\bar{k}_d^2(1-\alpha)\bar{u}_2(y - y_c). \tag{A.18}$$

These are the profiles to which the interfaces are relaxed to subsequently, at a specified rate r.

A.4 Linear stability

We next provide brief details of the linear stability analysis used in the main body of the paper to calculate the maximum growth rate. We start with the instantaneous zonally-averaged PV $\bar{q}_i$ and zonal velocity $\bar{u}_i$ in each layer $i = 1,\, 2$. In this subsection, these profiles are general functions of y for each sampled time t. In the numerical code, they are provided at each y grid point (typically 129 or 257 grid points, including the edges). The PV gradient $d\bar{q}_i/dy$, needed in the analysis below, is computed using centred differences in y. Notably, only the interior grid point values are needed, since the perturbation satisfies homogeneous boundary conditions (required to ensure zero meridional velocity at each boundary).

In the linear stability analysis, the base flow is considered to be both x and t-independent. Hence, we can consider infinitesimal perturbations of the form

$$\begin{aligned} q_i'(x,y,t) &= \Re\{Q_i(y)e^{\mathrm{i}(k_x x - \sigma t)}\} \\ \psi_i'(x,y,t) &= \Re\{\Psi_i(y)e^{\mathrm{i}(k_x x - \sigma t)}\} \end{aligned} \tag{A.19}$$

where k_x is a prescribed zonal wavenumber (necessarily integer for a domain of length $L_x = 2\pi$), σ is the frequency (the imaginary part of which, if non-zero, is the growth rate), while $Q(y)$ and $\Psi(y)$ are the perturbation amplitudes (eigenfunctions) to be determined along with σ (the eigenvalue).

Plugging the above forms into the conservative form of the governing equations (2.1) — with $F_i = 0$ — and in the PV inversion relations (2.8), then linearising, and finally cancelling the common $e^{\mathrm{i}(k_x x - \sigma t)}\}$ factor, we obtain the following eigen-system for the perturbation amplitudes $Q(y)$ and $\Psi(y)$ together with the phase speed $c = \sigma/k_x$:

$$(\bar{u}_i - c)Q_i + \frac{d\bar{q}_i}{dy}\Psi_i = 0, \quad i = 1,\, 2 \tag{A.20}$$

$$\frac{d^2\hat{\Psi}_j}{dy^2} - K_j^2\hat{\Psi}_j = \hat{Q}_j, \quad j = 1,\, 2 \tag{A.21}$$

$$\tag{A.22}$$

where i refers to layers, j and the hats refer to vertical modes, and $K_j^2 \equiv k_x^2 + \bar{k}_{dj}^2$. To combine these, we eliminate Q_i in the first set of equations using $\hat{Q}_j$ in the second set projected onto layers:

$$\begin{aligned} Q_i &= \tilde{c}_{i1}\hat{Q}_1 + \tilde{c}_{i2}\hat{Q}_2 \\ &= \frac{d^2\Psi_i}{dy^2} - \tilde{c}_{i1}K_1^2\hat{\Psi}_1 - \tilde{c}_{i2}K_2^2\hat{\Psi}_2. \end{aligned} \tag{A.23}$$

Next, we eliminate $\hat{\Psi}_1$ and $\hat{\Psi}_2$ by projecting them onto modes:

$$\hat{\Psi}_j = c_{j1}\Psi_1 + c_{j2}\Psi_2. \tag{A.24}$$

Using this in the expression for Q_i above, we obtain

$$Q_i = \frac{d^2\Psi_i}{dy^2} - B_{i1}\Psi_1 - B_{i2}\Psi_2 \tag{A.25}$$

where $B_{ij} \equiv \tilde{c}_{i1}K_1^2 c_{1j} + \tilde{c}_{i2}K_2^2 c_{2j}$. Finally, inserting this into (A.20) to eliminate Q_i

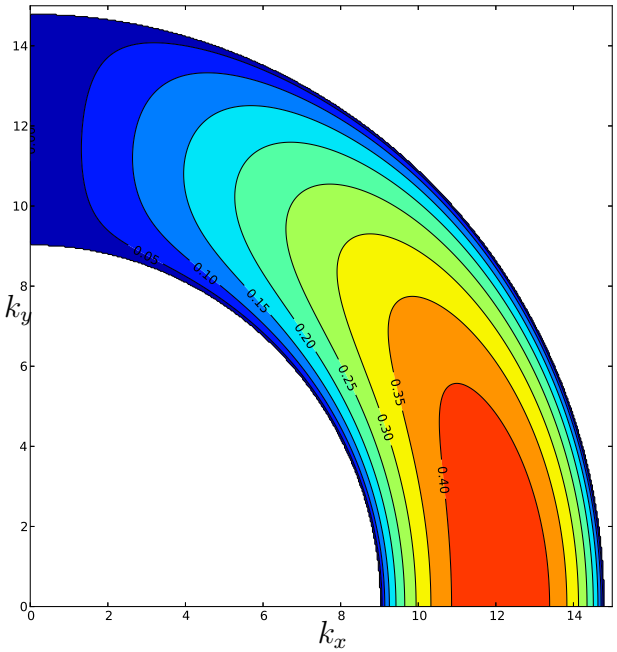

Figure A.1: Growth rate as a function of x and y wavenumbers, respectively k_x and k_y, for the initial flow state used for the characteristic simulation.

results in two coupled, second-order equations for the layer streamfunction amplitudes:

$$\begin{aligned}
\bar{u}_1 \frac{d^2\Psi_1}{dy^2} + \left(\frac{d\bar{q}_1}{dy} - \bar{u}_1 B_{11} \right) \Psi_1 - \bar{u}_1 B_{12} \Psi_2 &= c \left(\frac{d^2\Psi_1}{dy^2} - B_{11}\Psi_1 - B_{12}\Psi_2 \right) \\
\bar{u}_2 \frac{d^2\Psi_2}{dy^2} + \left(\frac{d\bar{q}_2}{dy} - \bar{u}_2 B_{21} \right) \Psi_1 - \bar{u}_2 B_{22} \Psi_2 &= c \left(\frac{d^2\Psi_2}{dy^2} - B_{21}\Psi_1 - B_{22}\Psi_2 \right) .
\end{aligned} \tag{A.26}$$

This is an eigenvalue problem for the phase speed c. It is solved numerically by discretising the second derivative terms by centred finite differences, and using the boundary conditions $\Psi_i = 0$ on both channel walls. This results in a block-tridiagonal generalised eigenvalue problem, which we have solved using the LAPACK routine **DGGEV**,

The results of the analysis above have been verified by matching them with the exact results obtained for the initially uniform PV gradients $d\bar{q}_i/dy = \epsilon_i \beta$ and uniform layer velocities $\bar{u}_i$, $i = 1, 2$. In this special case, we can seek solutions for $\Psi_i \propto \sin(k_y(y - y_{\mathsf{min}}))$ where k_y is the meridional wavenumber (an integer for $L_y = \pi$). This reduces (A.26) to a simple algebraic system, from which c is determined from a quadratic equation. It is straightforward to show that (baroclinic) instability always occurs when the PV gradients have opposite signs in the two layers, $\epsilon_1 \epsilon_2 < 0$ (details omitted).

Figure A.1 shows the growth rates as a function of k_x and k_y, obtained using the parameters of the characteristic simulation. The most unstable disturbances have small meridional wavenumbers k_y, and zonal wavenumbers k_x between 11 and 13. For a given k_x, the *maximum* growth rate is positive until $k_x > 13$. Hence, there are always disturbances with low k_x which are unstable (note: $k_x = 0$ is excluded). These disturbances simply have higher meridional wavenumbers k_y. Baroclinic instability occurs in a band of total wavenumbers $\sqrt{k_x^2 + k_y^2}$ between approximately 11 and 13 here.

Appendix B

Evolution variations

To illustrate the variability occurring between different simulations of the same flow, two other nearly identical simulations have been conducted. All parameters were kept the same as in the characteristic simulation previously illustrated, only the inversion grid resolution was halved to 256×129. Additionally, a different random number seed was used in each simulation.

The two simulations exhibit striking differences. In the first case, see figure B.1, we see oscillations between turbulent and quiescent phases, sometimes with a shift of the jets and homogeneous regions, while retaining the jet spacing. The flow alternates between the two different quiescent phases encountered in the characteristic simulation. The 'centred' state exhibits jets slowly coming together toward the center of the domain. By contrast, the 'shifted' state does not exhibit any evident jet drift and moreover appears to be much shorter lived. Arguably, the jet configuration of this state is less robust than that in the centred state, though both the stability analysis of the zonal flow and the APE spectrum show no major differences between the states.

In the second simulation, see figure B.2, the shifted quiescent state develops after the initial baroclinic instability and dominates the first third of the simulation. Turbulent events throughout this period collapse back to this state except for the last one. This prominent turbulent event instead collapses to a new configuration resembling the centred state seen over much of the characteristic simulation. This state then dominates the remainder of the evolution.

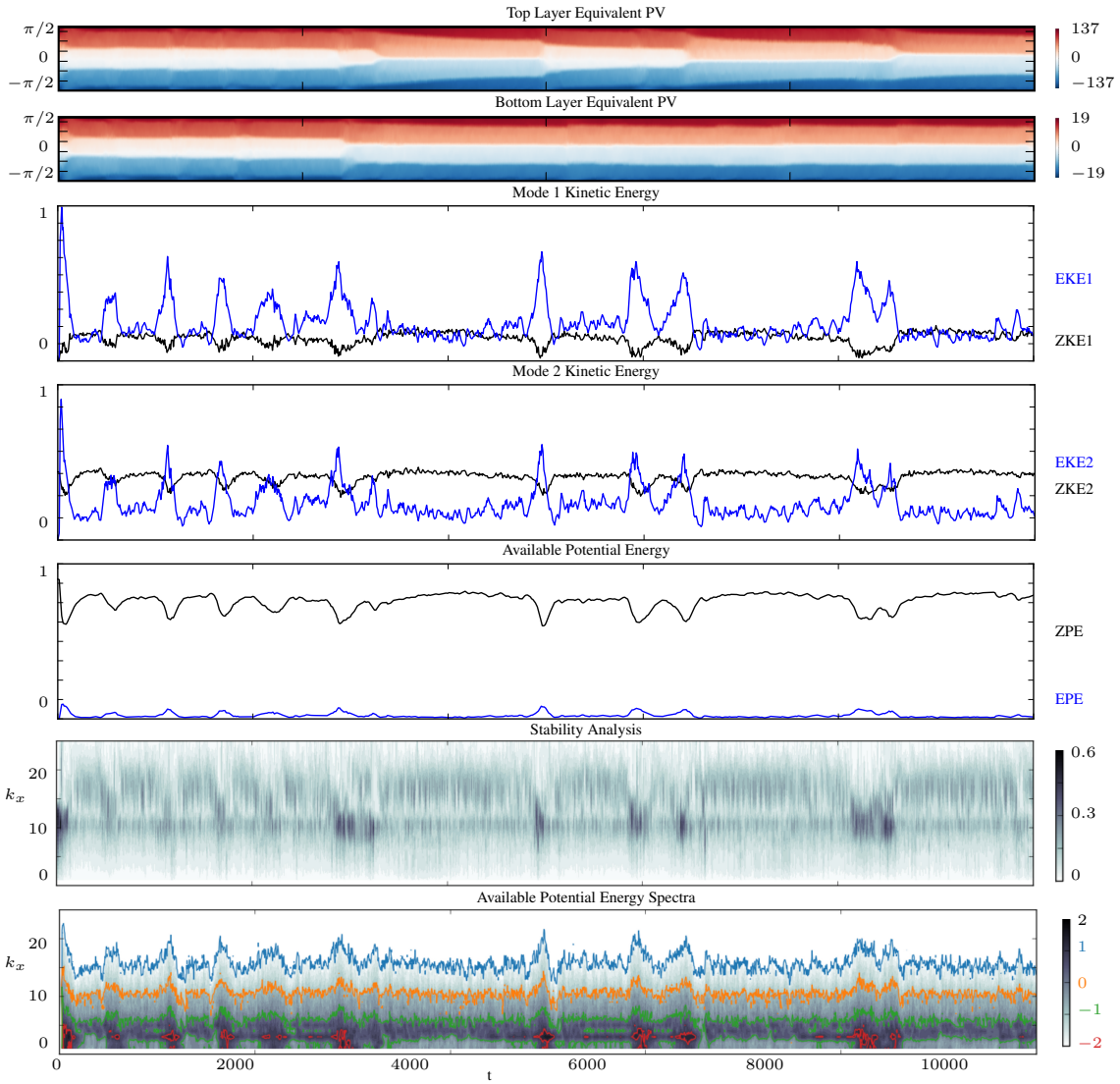

Figure B.1: (a,b) Hövmoller diagrams of the equivalent PV, with latitude in the ordinate. (c,d,e) Energy components (with the eddy part in blue and the zonal part in black) versus time. (f) log_{10} of the maximum growth rate of the zonally-averaged flow versus zonal wavenumbers. (g) log_{10} of the y-integrated spectrum of the available potential energy versus zonal wavenumbers. For all these plots time is in the abscissa. The same parameters are used as in the characteristic simulation but on a 256×128 basic inversion grid.

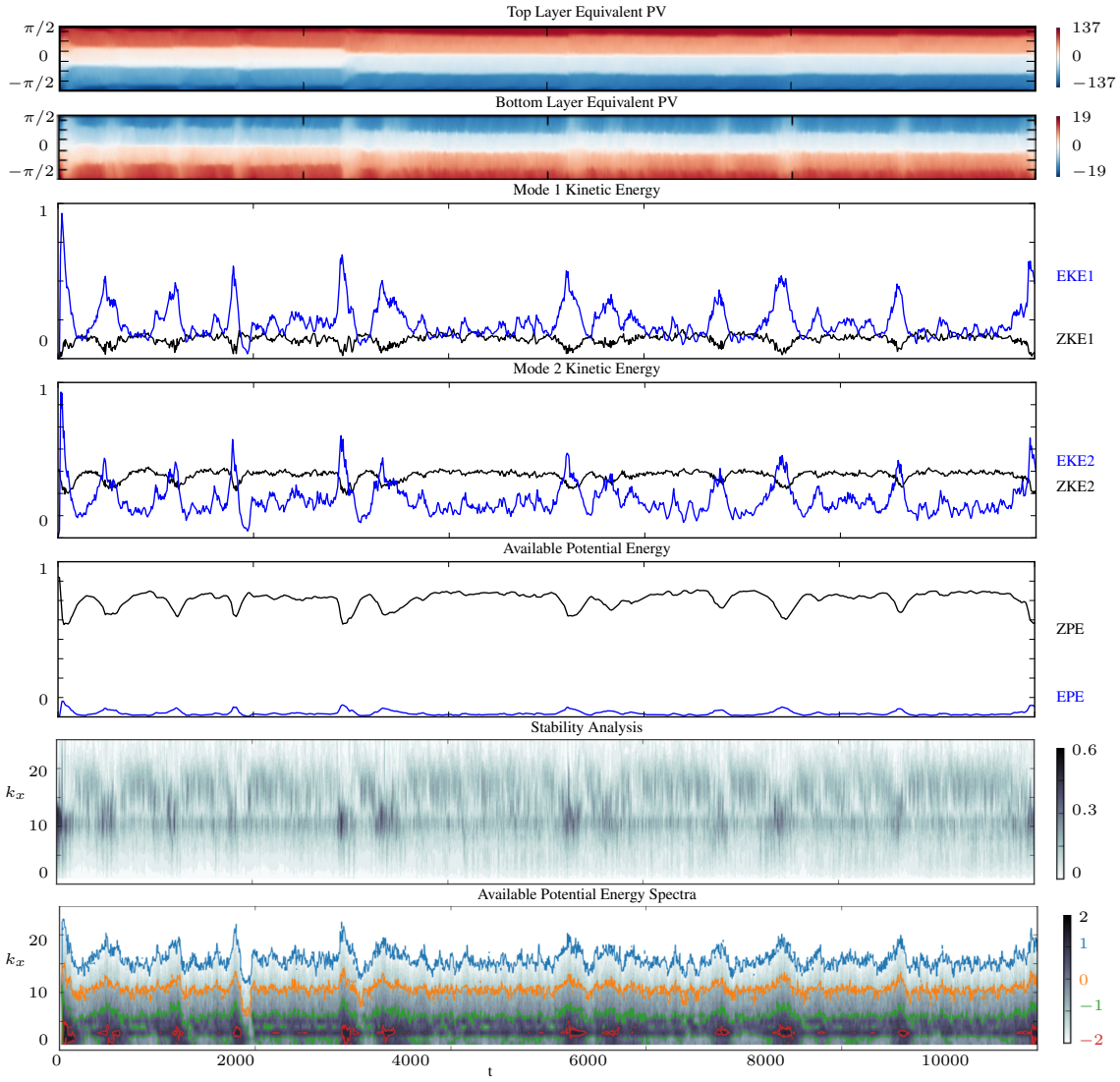

Figure B.2: As in figure B.1 but for a different initial random seed .

Bibliography

A. Adriani, A. Mura, G. Orton, C. Hansen, F. Altieri, M. Moriconi, J. Rogers, G. Eichstädt, T. Momary, A. Ingersoll, et al. Clusters of cyclones encircling Jupiter's poles. Nature, 555(7695):216, 2018.

Y. Afanasyev, P. Rhines, and E. Lindahl. Velocity and potential vorticity fields measured by altimetric imaging velocimetry in the rotating fluid. Experiments in fluids, 47(6): 913, 2009.

B. K. Arbic and G. R. Flierl. Baroclinically unstable geostrophic turbulence in the limits of strong and weak bottom Ekman friction: Application to midocean eddies. Journal of Physical Oceanography, 34(10):2257–2273, 2004.

D. H. Atkinson, J. B. Pollack, and A. Seiff. The Galileo probe Doppler wind experiment: Measurement of the deep zonal winds on Jupiter. Journal of Geophysical Research, 103(E10):22911–22928, 1998.

J. M. Aurnou and M. H. Heimpel. Zonal jets in rotating convection with mixed mechanical boundary conditions. Icarus, 169(2):492–498, 2004.

J. M. Aurnou and P. L. Olson. Strong zonal winds from thermal convection in a rotating spherical shell. Geophysical research letters, 28(13):2557–2559, 2001.

M. P. Baldwin, P. B. Rhines, H.-P. Huang, and M. E. McIntyre. The Jet-Stream Conundrum. Science, 315:467–468, 2007.

D. Banfield, P. Gierasch, M. Bell, E. Ustinov, A. Ingersoll, A. Vasavada, R. A. West, and M. Belton. Jupiter's cloud structure from Galileo imaging data. Icarus, 135(1): 230–250, 1998.

E. A. Barnes and L. Polvani. Response of the midlatitude jets, and of their variability, to increased greenhouse gases in the CMIP5 models. Journal of Climate, 26(18):7117–7135, 2013.

M. E. Bastin and P. L. Read. A laboratory study of baroclinic waves and turbulence in an internally heated rotating fluid annulus with sloping endwalls. Journal of Fluid Mechanics, 339:173–198, 1997.

P. Berloff, S. Karabasov, J. T. Farrar, and I. Kamenkovich. On latency of multiple zonal jets in the oceans. Journal of Fluid Mechanics, 686:534–567, 2011.

A. Berman, J. Bradford, and T. Lundgren. Two-fluid spin-up in a centrifuge. Journal of Fluid Mechanics, 84(3):411–431, 1978.

E. J. Boland, A. F. Thompson, E. Shuckburgh, and P. H. Haynes. The formation of non-zonal jets over sloped topography. Journal of Physical Oceanography, 42(10):1635–1651, 2012.

A. P. Boss. Evolution of the solar nebula. IV. Giant gaseous protoplanet formation. The Astrophysical Journal, 503(2):923, 1998.

A. S. Bower. A simple kinematic mechanism for mixing fluid parcels across a meandering jet. Journal of Physical Oceanography, 21(1):173–180, 1991.

A. S. Bower, H. T. Rossby, and J. L. Lillibridge. The Gulf Streambarrier or blender? Journal of Physical Oceanography, 15(1):24–32, 1985.

J. Bradford, A. Berman, and T. Lundgren. Nongeostrophic baroclinic instability in a two-fluid layer rotating system. Journal of the Atmospheric Sciences, 38(7):1376–1389, 1981.

F. H. Busse. Thermal instabilities in rapidly rotating systems. Journal of Fluid Mechanics, 44(03):441–460, 1970.

F. H. Busse. A simple model of convection in the Jovian atmosphere. Icarus, 29:255–260, 1976.

G. Buzyna, R. L. Pfeffer, and R. Kung. Kinematic properties of wave amplitude vacillation in a thermally driven rotating fluid. Journal of the Atmospheric Sciences, 46(17): 2716–2730, 1989.

P. Cardin and P. Olson. Chaotic thermal convection in a rapidly rotating spherical shell: consequences for flow in the outer core. Physics of the earth and planetary interiors, 82(3-4):235–259, 1994.

X. Carton. Hydrodynamical modeling of oceanic vortices. Surveys in Geophysics, 22(3): 179–263, 2001.

X. Carton. Oceanic vortices. In Fronts, Waves and Vortices in Geophysical Flows, pages 61–108. Springer, 2010.

P. Cessi and F. Primeau. Dissipative selection of low-frequency modes in a reduced-gravity basin. Journal of Physical Oceanography, 31(1):127–137, 2001.

J. G. Charney. Geostrophic turbulence. Journal of the Atmospheric Sciences, 28(6): 1087–1095, 1971.

E. P. Chassignet and D. P. Marshall. Gulf Stream separation in numerical ocean models. Ocean Modeling in an Eddying Regime, pages 39–61, 2008.

C. Chen and I. Kamenkovich. Effects of topography on baroclinic instability. Journal of Physical Oceanography, 43(4):790–804, 2013.

J. Y.-K. Cho and L. M. Polvani. The emergence of jets and vortices in freely-evolving shallow-water turbulence on a sphere. Physics of Fluids, 8:1531–1552, 1996.

U. Christensen. Zonal flow driven by strongly supercritical convection in rotating spherical shells. Journal of Fluid Mechanics, 470:115–133, 2002.

G. G. Coriolis. Mémoire sur les équations du mouvement relatif des systèmes de corps. Bachelier, 1835.

C. S. Cox. Measurements of slopes of high-frequency wind waves. Journal of Marine Research, 16:199–225, 1958.

D. Dabiri and M. Gharib. Simultaneous free-surface deformation and near-surface velocity measurements. Experiments in Fluids, 30(4):381–390, 2001.

S. Dalziel, G. O. Hughes, and B. R. Sutherland. Whole-field density measurements by synthetic schlieren. Experiments in Fluids, 28(4):322–335, 2000.

J. Darbyshire. The effect of bottom topography on the Agulhas Current. Pure and Applied Geophysics, 101(1):208–220, 1972.

G. Daviero, P. Roberts, and K. Maile. Refractive index matching in large-scale stratified experiments. Experiments in Fluids, 31(2):119–126, 2001.

A. B. de Saint-Venant. Mémoire sur la prise en considération de la force centrifuge dans le calcul du mouvement des eaux courantes et sur la distinction des torrents et des rivières. Mémoires de l'Académie des sciences de l'Institut de France, 44:245–273, 1888.

T. E. Dowling. Dynamics of Jovian atmospheres. Annual Review of Fluid Mechanics, 27 (1):293–334, 1995.

T. E. Dowling and A. P. Ingersoll. Potential vorticity and layer thickness variations in the flow around Jupiter's Great Red Spot and White Oval BC. Journal of the Atmospheric Sciences, 45(8):1380–1396, 1988.

T. E. Dowling and A. P. Ingersoll. Jupiter's great red spot as a shallow water system. Journal of the Atmospheric Sciences, 46:3256–3278, 1989.

D. G. Dritschel. The stability of elliptical vortices in an external straining flow. Journal of Fluid Mechanics, 210:223–261, 1990.

D. G. Dritschel and M. H. P. Ambaum. A contour-advective semi-Lagrangian numerical algorithm for simulating fine-scale conservative dynamical fields. Quarterly Journal of the Royal Meteorological Society, 123:1097–1130, 1997.

D. G. Dritschel and J. Fontane. The combined Lagrangian advection method. Journal of Computational Physics, 229:5408–5417, 2010.

D. G. Dritschel and M. E. McIntyre. Multiple jets as PV staircases: the Phillips effect and the resilience of eddy-transport barriers. Journal of the Atmospheric Sciences, 65: 855–874, 2008.

D. G. Dritschel and S. M. Tobias. Two-dimensional magnetohydrodynamic turbulence in the small magnetic Prandtl number limit. Journal of Fluid Mechanics, 703:85–98, 2012.

D. G. Dritschel, M. de la Torre Juárez, and M. H. Ambaum. The three-dimensional vortical nature of atmospheric and oceanic turbulent flows. Physics of Fluids, 11(6): 1512–1520, 1999.

C. Egbers, W. Beyer, A. Bonhage, R. Hollerbach, and P. Beltrame. The geoflow-experiment on ISS (part I): Experimental preparation and design of laboratory testing hardware. Advances in Space Research, 32(2):171–180, 2003.

J. G. Esler. The turbulent equilibration of an unstable baroclinic jet. Journal of Fluid Mechanics, 599:241–268, 2008.

S. B. Feldstein and I. M. Held. Barotropic decay of baroclinic waves in a two-layer beta-plane model. Journal of Atmospheric Sciences, 46(22):3416–3430, 1989.

J.-B. Flór, H. Scolan, and J. Gula. Frontal instabilities and waves in a differentially rotating fluid. Journal of Fluid Mechanics, 685:532–542, 2011.

J. Fontane and D. G. Dritschel. The HyperCASL algorithm: a new approach to the numerical simulation of geophysical flows. Journal of Computational Physics, 228 (17):6411–6425, 2009.

R. M. Friedman. Appropriating the weather: Vilhelm Bjerknes and the construction of a modern meteorology. Cornell University Press, 1993.

L. Fu and G. R. Flierl. Nonlinear energy and enstrophy transfers in a realistically stratified ocean. Dynamics of Atmospheres and Oceans, 4(4):219–246, 1980.

D. Fultz, R. R. Long, G. V. Owens, W. Bohan, R. Kaylor, and J. Weil. Studies of thermal convection in a rotating cylinder with some implications for large-scale atmospheric motions. In Studies of Thermal Convection in a Rotating Cylinder with Some Implications for Large-Scale Atmospheric Motions, pages 1–104. Springer, 1959.

B. Galperin, H. Nakano, H.-P. Huang, and S. Sukoriansky. The ubiquitous zonal jets in the atmospheres of giant planets and Earth's oceans. Geophysical Research Letters, 31:L13303, 2004.

G. A. Glatzmaier, M. Evonuk, and T. M. Rogers. Differential rotation in giant planets maintained by density-stratified turbulent convection. Geophysical and Astrophysical Fluid Dynamics, 103(1):31–51, 2009.

T. Guillot. A comparison of the interiors of Jupiter and Saturn. Planetary and Space Science, 47(10-11):1183–1200, 1999.

T. Guillot, Y. Miguel, B. Militzer, W. Hubbard, Y. Kaspi, E. Galanti, H. Cao, R. Helled, S. Wahl, L. Iess, et al. A suppression of differential rotation in Jupiters deep interior. Nature, 555(7695):227, 2018.

J. Gula, V. Zeitlin, and R. Plougonven. Instabilities of two-layer shallow-water flows with vertical shear in the rotating annulus. Journal of Fluid Mechanics, 638:27–47, 2009.

G. Hadley et al. VI. Concerning the cause of the general trade-winds. Philosophical Transactions, 39(437):58–62, 1735.

U. Harlander, T. von Larcher, Y. Wang, and C. Egbers. PIV-and LDV-measurements of baroclinic wave interactions in a thermally driven rotating annulus. Experiments in Fluids, 51(1):37–49, 2011.

J. Hart. A laboratory study of baroclinic instability. Geophysical & Astrophysical Fluid Dynamics, 3(1):181–209, 1972.

J. Hart. Baroclinic instability over a slope. Part I: Linear theory. Journal of Physical Oceanography, 5(4):625–633, 1975.

P. Haynes. Stratospheric dynamics. Annual Review of Fluid Mechanics, 37:263–293, 2005.

R. Hide. Some experiments on thermal convection in a rotating liquid. Quarterly Journal of the Royal Meteorological Society, 79(339):161–161, 1953.

R. Hide. An experimental study of thermal convection in a rotating liquid. Philosophical Transactions of the Royal Society A, 250(983):441–478, 1958.

R. Hide and W. Fowlis. Thermal convection in a rotating annulus of liquid: effect of viscosity on the transition between axisymmetric and non-axisymmetric flow regimes. Journal of the Atmospheric Sciences, 22(5):541–558, 1965.

R. Hide and P. Mason. Baroclinic waves in a rotating fluid subject to internal heating. Philosophical Transactions of the Royal Society A, 268(1186):201–232, 1970.

A. P. Ingersoll, R. F. Beebe, J. L. Mitchell, G. W. Garneau, G. M. Yagi, and J.-P. Müller. Interaction of eddies and mean zonal flow on Jupiter as inferred from Voyager 1 and 2 images. Journal of Geophysical Research: Space Physics, 86(A10):8733–8743, 1981.

A. P. Ingersoll, T. E. Dowling, P. J. Gierasch, G. S. Orton, P. L. Read, A. Sánchez-Lavega, A. P. Showman, A. A. Simon-Miller, and A. R. Vasavada. Dynamics of Jupiters atmosphere. Jupiter: The Planet, Satellites and Magnetosphere, 105, 2004.

P. Irwin. Giant planets of our solar system: atmospheres, composition, and structure. Springer Science & Business Media, 2009.

L. Jackson, C. W. Hughes, and R. G. Williams. Topographic control of basin and channel flows: The role of bottom pressure torques and friction. Journal of Physical Oceanography, 36(9):1786–1805, 2006.

B. Jähne, J. Klinke, and S. Waas. Imaging of short ocean wind waves: a critical theoretical review. JOSA A, 11(8):2197–2209, 1994.

I. N. James. Suppression of baroclinic instability in horizontally sheared flows. Journal of the Atmospheric Sciences, 44(24):3710–3720, 1987.

T. Jougla and D. G. Dritschel. On the energetics of a two-layer baroclinic flow. Journal of Fluid Mechanics, 816:586–618, 2017.

I. Kamenkovich, P. Berloff, and J. Pedlosky. Role of eddy forcing in the dynamics of multiple zonal jets in a model of the North Atlantic. Journal of Physical Oceanography, 39(6):1361–1379, 2009.

Y. Kaspi and G. R. Flierl. Formation of jets by baroclinic instability on gas planet atmospheres. Journal of the Atmospheric Sciences, 64(9):3177–3194, 2007.

Y. Kaspi, G. R. Flierl, and A. P. Showman. The deep wind structure of the giant planets: Results from an anelastic general circulation model. Icarus, 202(2):525–542, 2009.

Y. Kaspi, E. Galanti, W. Hubbard, D. Stevenson, S. Bolton, L. Iess, T. Guillot, J. Bloxham, J. Connerney, H. Cao, et al. Jupiters atmospheric jet streams extend thousands of kilometres deep. Nature, 555(7695):223, 2018.

J. Kurata, K. Grattan, H. Uchiyama, and T. Tanaka. Water surface measurement in a shallow channel using the transmitted image of a grating. Review of Scientific Instruments, 61(2):736–739, 1990.

J. LaCasce and K. Brink. Geostrophic turbulence over a slope. Journal of Physical Oceanography, 30(6):1305–1324, 2000.

T. Larcher, C. Egbers, et al. Experiments on transitions of baroclinic waves in a differentially heated rotating annulus. Nonlinear Processes in Geophysics, 12(6):1033–1041, 2005.

L. Li, A. P. Ingersoll, A. R. Vasavada, C. C. Porco, A. D. Del Genio, and S. P. Ewald. Life cycles of spots on Jupiter from Cassini images. Icarus, 172(1):9–23, 2004.

S. S. Limaye. Jupiter: New estimates of the mean zonal flow at the cloud level. Icarus, 65(2):335–352, 1986.

R. S. Lindzen, B. Farrell, and D. Jacqmin. Vacillations due to wave interference: Applications to the atmosphere and to annulus experiments. Journal of the Atmospheric Sciences, 39(1):14–23, 1982.

J. J. Lissauer. Planet formation. Annual Review of Astronomy and Astrophysics, 31(1): 129–172, 1993.

J. Liu and T. Schneider. Mechanisms of jet formation on the giant planets. Journal of the Atmospheric Sciences, 2009.

A. Lovegrove, P. Read, and C. Richards. Generation of inertia-gravity waves by a time-dependent baroclinic wave in the laboratory. Physics and Chemistry of the Earth, Part B: Hydrology, Oceans and Atmosphere, 24(5):455–460, 1999.

A. Lovegrove, P. Read, and C. Richards. Generation of inertia-gravity waves in a baroclinically unstable fluid. Quarterly Journal of the Royal Meteorological Society, 126 (570):3233–3254, 2000.

P. S. Marcus. Numerical simulation of jupiter's great red spot. Nature, 331(6158):693, 1988.

P. S. Marcus. Jupiter's great red spot and other vortices. Annual Review of Astronomy and Astrophysics, 31:523–573, 1993.

P. Mason. Baroclinic waves in a container with sloping end walls. Philosophical Transactions of the Royal Society A, 278(1284):397–445, 1975.

R. P. Matano. A numerical study of the Agulhas retroflection: The role of bottom topography. Journal of Physical Oceanography, 26(10):2267–2279, 1996.

A. Matulka and Y. Afanasyev. Zonal jets in equilibrating baroclinic instability on the polar beta-plane: Experiments with altimetry. Journal of Geophysical Research: Oceans, 120 (9):6130–6144, 2015.

N. A. Maximenko, B. Bang, and H. Sasaki. Observational evidence of alternating zonal jets in the world ocean. Geophysical Research Letters, 32(12), 2005.

A. R. Mohebalhojeh and D. G. Dritschel. Contour-advective semi-Lagrangian algorithms for many-layer primitive-equation models. Quarterly Journal of the Royal Meteorological Society, 130(596):347–364, 2004.

F. Moisy, M. Rabaud, and K. Salsac. A synthetic Schlieren method for the measurement of the topography of a liquid interface. Experiments in Fluids, 46(6):1021, 2009.

D. R. Ohlsen and J. E. Hart. The transition to baroclinic chaos on the β-plane. Journal of Fluid Mechanics, 203:23–50, 1989.

D. B. Olson. Rings in the ocean. Annual Review of Earth and Planetary Sciences, 19(1): 283–311, 1991.

I. Orlanski. The influence of bottom topography on the stability of jets in a baroclinic fluid. Journal of the Atmospheric Sciences, 26(6):1216–1232, 1969.

R. L. Panetta. Zonal jets in wide baroclinically unstable regions: Persistence and scale selection. Journal of the atmospheric sciences, 50(14):2073–2106, 1993.

R. L. Panetta and I. M. Held. Baroclinic eddy fluxes in a one-dimensional model of quasi-geostrophic turbulence. Journal of the Atmospheric Sciences, 45(22):3354–3365, 1988.

J. Pedlosky. Finite-amplitude baroclinic waves. Journal of the Atmospheric Sciences, 27 (1):15–30, 1970.

N. Phillips. A simple three-dimensional model for the study of large-scale extra-tropical flow patterns. Journal of Meteorology, 8:381–394, 1951.

C. C. Porco, R. A. West, A. McEwen, A. D. DG., A. P. Ingersoll, P. Thomas, S. Squyres, L. Dones, C. D. Murray, T. V. Johnson, et al. Cassini imaging of Jupiter's atmosphere, satellites, and rings. Science, 299(5612):1541–1547, 2003.

F. Poulin and G. Flierl. The influence of topography on the stability of jets. Journal of Physical Oceanography, 35(5):811–825, 2005.

F. Poulin, A. Stegner, M. Hernández-Arencibia, A. Marrero-Díaz, and P. Sangrà. Steep shelf stabilization of the coastal Bransfield Current: Linear stability analysis. Journal of Physical Oceanography, 44(2):714–732, 2014.

A. Randriamampianina, P. Maubert, W.-G. Fruh, and P. L. Read. DNS of structural vacillation in the transition to geostrophic turbulence, pages 432–434. Springer, 2007.

P. L. Read, P. J. Gierasch, B. J. Conrath, A. Simon-Miller, T. Fouchet, and Y. H. Yamazaki. Mapping potential-vorticity dynamics on Jupiter. I: Zonal-mean circulation from Cassini and Voyager 1 data. Quarterly Journal of the Royal Meteorological Society, 132(618):1577–1603, 2006.

P. L. Read, Y. H. Yamazaki, S. R. Lewis, P. D. Williams, R. Wordsworth, K. Miki-Yamazaki, J. Sommeria, and H. Didelle. Dynamics of convectively driven banded jets in the laboratory. Journal of the Atmospheric Sciences, 64:4031–4052, 2007.

J. N. Reinaud, D. G. Dritschel, and C. Koudella. The shape of vortices in quasi-geostrophic turbulence. Journal of Fluid Mechanics, 474:175–192, 2003.

P. Rhines, E. Lindahl, and A. Mendez. Optical altimetry: a new method for observing rotating fluids with applications to Rossby and inertial waves on a polar beta-plane. Journal of Fluid Mechanics, 572:389–412, 2007.

P. B. Rhines. Waves and turbulence on a beta-plane. Journal of Fluid Mechanics, 69: 417–443, 1975.

K. Richards, N. Maximenko, F. Bryan, and H. Sasaki. Zonal jets in the Pacific Ocean. Geophysical Research Letters, 33(3), 2006.

L. F. Richardson. Weather prediction by numerical process. Cambridge University Press, 2007.

C. Rodda, I. Borcia, P. Le Gal, M. Vincze, and U. Harlander. Baroclinic, Kelvin and inertia-gravity waves in the barostrat instability experiment. Geophysical & Astrophysical Fluid Dynamics, pages 1–32, 2018.

J. H. Rogers. The giant planet Jupiter. Number 6. Cambridge University Press, 1995.

A. Sachs. Babylonian observational astronomy. Philosophical Transactions of the Royal Society of London A: Mathematical, Physical and Engineering Sciences, 276(1257): 43–50, 1974.

R. Salmon. Geostrophic turbulence, 1982.

A. Sanchez-Lavega, G. Orton, R. Morales, J. Lecacheux, F. Colas, B. Fisher, P. Fukumura-Sawada, W. Golisch, D. Griep, C. Kaminski, et al. The merger of two giant anticyclones in the atmosphere of Jupiter. Icarus, 149(2):491–495, 2001.

M. J. Schmeits and H. A. Dijkstra. Bimodal behavior of the Kuroshio and the Gulf Stream. Journal of Physical Oceanography, 31(12):3435–3456, 2001.

H. Scolan and P. L. Read. A rotating annulus driven by localized convective forcing: a new atmosphere-like experiment. Experiments in Fluids, 58(6):75, 2017.

H. Scolan, R. Verzicco, and J.-B. Flór. Frontal Instabilities at Density–Shear Interfaces in Rotating Two-Layer Stratified Fluids. Modeling Atmospheric and Oceanic Flows: Insights from Laboratory Experiments and Numerical Simulations, 205, 2014.

R. K. Scott. Non-robustness of the two-dimensional turbulent inverse cascade. Physical Review E, 75:046301, 2007.

R. K. Scott and D. G. Dritschel. The structure of zonal jets in geostrophic turbulence. Journal of Fluid Mechanics, 711:576–598, 2012.

R. K. Scott and D. G. Dritschel. Zonal jet formation by potential vorticity mixing at large and small scales. B. Galperin and P.L. Read, Eds., Cambridge University Press, 2018.

R. K. Scott and L. M. Polvani. Forced-dissipative shallow water turbulence on the sphere and the atmospheric circulation of the gas planets. Journal of the Atmospheric Sciences, 64:3158–3176, 2007.

R. K. Scott and A.-S. Tissier. The generation of zonal jets by large-scale mixing. Physics of Fluids, 24:126601, 2012.

A. P. Showman. Numerical simulations of forced shallow-water turbulence: effects of moist convection on the large-scale circulation of Jupiter and Saturn. Journal of the Atmospheric Sciences, 2007. In press.

A. P. Showman, J. Y. Cho, and K. Menou. Atmospheric circulation of exoplanets. Exoplanets, 526:471–516, 2010.

A. A. Simon, M. H. Wong, and G. S. Orton. First Results from the Hubble OPAL Program: Jupiter in 2015. The Astrophysical Journal, 812(1):55, 2015.

A. A. Simon-Miller, P. J. Gierasch, R. F. Beebe, B. Conrath, F. M. Flasar, R. K. Achterberg, C. C. Team, et al. New observational results concerning Jupiter's great red spot. Icarus, 158(1):249–266, 2002.

C. A. Smith, K. G. Speer, and R. W. Griffiths. Multiple zonal jets in a differentially heated rotating annulus. Journal of Physical Oceanography, 44(9):2273–2291, 2014.

K. S. Smith and G. K. Vallis. The scales and equilibration of midocean eddies: Forced–dissipative flow. Journal of Physical Oceanography, 32(6):1699–1720, 2002.

J. Sommeria, S. D. Meyers, and H. L. Swinney. Laboratory simulation of Jupiter's great red spot. Nature, 331(6158):689, 1988.

A. Spiga, S. Guerlet, Y. Meurdesoif, M. Indurain, E. Millour, T. Dubos, M. Sylvestre, J. Leconte, and T. Fouchet. Waves and eddies simulated by high-resolution Global Climate Modeling of Saturn's troposphere and stratosphere. In EPSC 2015, volume 10, page 881, 2015.

D. Steinsaltz. Instability of baroclinic waves with bottom slope. Journal of Physical Oceanography, 17(12):2343–2350, 1987.

A. Stern, L.-P. Nadeau, and D. Holland. Instability and mixing of zonal jets along an idealized continental shelf break. Journal of Physical Oceanography, 45(9):2315–2338, 2015.

K. Sugiyama, M. Odaka, K. Kuramoto, and Y. Hayashi. Static stability of the Jovian atmospheres estimated from moist adiabatic profiles. Geophysical Research Letters, 33(3), 2006.

S. Sukoriansky, N. Dikovskaya, and B. Galperin. On the arrest of inverse energy cascade and the Rhines scale. Journal of the Atmospheric Sciences, 64:3312–3327, 2007.

B. R. Sutherland, S. B. Dalziel, G. O. Hughes, and P. Linden. Visualization and measurement of internal waves by synthetic schlieren. Part 1. Vertically oscillating cylinder. Journal of Fluid Mechanics, 390:93–126, 1999.

C. E. Tansley and D. P. Marshall. On the influence of bottom topography and the Deep Western Boundary Current on Gulf Stream separation. Journal of Marine Research, 58 (2):297–325, 2000.

A. F. Thompson. Jet formation and evolution in baroclinic turbulence with simple topography. Journal of Physical Oceanography, 40(2):257–278, 2010.

A. F. Thompson and J.-B. Sallée. Jets and topography: Jet transitions and the impact on transport in the Antarctic Circumpolar Current. Journal of Physical Oceanography, 42 (6):956–972, 2012.

A. F. Thompson and W. R. Young. Two-layer baroclinic eddy heat fluxes: zonal flows and energy balance. Journal of the Atmospheric Sciences, 64:3214–3231, 2007.

D. W. Thompson and J. M. Wallace. Annular modes in the extratropical circulation. Part I: Month-to-month variability. Journal of Climate, 13(5):1000–1016, 2000.

S. I. Thomson and M. E. McIntyre. Jupiters unearthly jets: a new turbulent model exhibiting statistical steadiness without large-scale dissipation. Journal of the Atmospheric Sciences, 73(3):1119–1141, 2016.

C. D. Thorncroft, B. J. Hoskins, and M. E. McIntyre. Two paradigms of baroclinic-wave life-cycle behaviour. Quarterly Journal of the Royal Meteorological Society, 119:17–55, 1993.

J.-H. Thysen. Frontal instabilities: generation of small-waves and vortex formation in the baroclinic unstable regime, 2014.

A. Treguier and B. Hua. Influence of bottom topography on stratified quasi-geostrophic turbulence in the ocean. Geophysical & Astrophysical Fluid Dynamics, 43(3-4):265–305, 1988.

A.-M. Tréguier and J. McWilliams. Topographic influences on wind-driven, stratified flow in a β-plane channel: An idealized model for the antarctic circumpolar current. Journal of physical oceanography, 20(3):321–343, 1990.

G. K. Vallis. Atmospheric and Oceanic Fluid Dynamics. Cambridge University Press, 2006.

A. R. Vasavada and A. P. Showman. Jovian atmospheric dynamics: An update after Galileo and Cassini. Reports on Progress in Physics, 68(8):1935, 2005.

A. R. Vasavada, A. P. Ingersoll, D. Banfield, M. Bell, P. J. Gierasch, M. J. Belton, G. S. Orton, K. P. Klaasen, E. DeJong, H. H. Breneman, et al. Galileo imaging of Jupiter's atmosphere: The Great Red Spot, equatorial region, and white ovals. Icarus, 135(1): 265–275, 1998.

A. Venaille. Bottom-trapped currents as statistical equilibrium states above topographic anomalies. Journal of Fluid Mechanics, 699:500–510, 2012.

A. Venaille, L. Nadeau, and G. K. Vallis. Ribbon turbulence. Physics of Fluids, 26(12): 126605, 2014.

M. Vincze, U. Harlander, T. von Larcher, and C. Egbers. An experimental study of regime transitions in a differentially heated baroclinic annulus with flat and sloping bottom topographies. arXiv preprint arXiv:1309.0321, 2013.

G. P. Williams. Planetary circulations: 1. Barotropic representation of Jovian and terrestrial turbulence. Journal of the Atmospheric Sciences, 35:1399–1424, 1978.

P. D. Williams, T. W. Haine, and P. L. Read. On the generation mechanisms of short-scale unbalanced modes in rotating two-layer flows with vertical shear. Journal of Fluid Mechanics, 528:1–22, 2005.

J.-O. Wolff, E. Maier-Reimer, and D. J. Olbers. Wind-driven flow over topography in a zonal β-plane channel: A quasi-geostrophic model of the Antarctic Circumpolar Current. Journal of Physical Oceanography, 21(2):236–264, 1991.

R. M. Young and P. L. Read. Forward and inverse kinetic energy cascades in Jupiters turbulent weather layer. Nature Physics, 13(11):1135, 2017.

X. Zhang, D. Dabiri, and M. Gharib. Optical mapping of fluid density interfaces: concepts and implementations. Review of Scientific Instruments, 67(5):1858–1868, 1996.